Universidad Carlos III de Madrid
www.uc3m.es

TESIS DOCTORAL

Application of unconventional methods to MIM Inconel 718 components

Autor:
OLIVIER DUGAUGUEZ

Director/es:
Pr. José Manuel Torralba Castello
Dr. Antonia Jimenez Morales
Pr. Thierry Barrière
Pr. Jean-Claude Gelin

Department of Materials Science and Engineering

Leganés, 1st of December 2017

Universidad Carlos III de Madrid
www.uc3m.es

(a entregar en la Oficina de Posgrado, una vez nombrado el Tribunal evaluador , para preparar el documento para la defensa de la tesis)

TESIS DOCTORAL

Application of unconventional methods to MIM Inconel 718 components

Autor: ***Olivier DUGAUGUEZ***

Firma del Tribunal Calificador:

Firma

Presidente: **Monica Campos Gomez**, assistant profesor
University Carlos III of Madrid

Vocal: **Didier Bouvard**, Professor
Polytechnic Institute of Grenoble

Secretario: **Lars Nyborg**, Professor
Chalmers University of Technology

Suplente: **Maria Teresa Freire Vieira**, Professor
University of Coïmbra

Calificación: Ciencia e Ingenieríad e Materiales e Ingeniería Química

Leganés, 1st of December 2017

TABLE OF CONTENTS

TABLE OF CONTENTS ..... **II**

LIST OF FIGURES ..... **V**

LIST OF TABLES ..... **X**

LIST OF ABREVIATION AND SYMPOLS ..... **XI**

ABSTRACT ..... **XII**

I INTRODUCTION **1**

I.1 CONTEXT OF THE PHD PROJECT 1
I.2 SPECIFICATIONS OF THE PROJECT 3
I.2.1 Choice of the material *3*
I.2.2 Investigation of new processing methods for MIM samples *4*
I.3 EXPERIMENTAL WORK DEVELOPED FOR THE PROJECT 5

REFERENCES **7**

II INTRODUCTION TO THE NICKEL-CHROME SUPERALLOYS, THE MIM PROCESS AND THE UNCONVENTIONAL SINTERING PROCESSES **9**

II.1 NICKEL BASED SUPERALLOYS AND INCONEL 718 9
II.1.1 Application of the Nickel based superalloys *9*
II.1.2 Composition of Inconel 718 ..... *10*
II.1.3 Structure of Inconel 718 ..... *11*
II.1.4 Thermal behaviour of Inconel 718 ..... *14*
II.1.5 Mechanical behaviour of Inconel 718 ..... *15*
II.2 INTRODUCTION TO POWDER METALLURGY 17
II.3 INTRODUCTION TO POWDER INJECTION MOULDING 19
II.3.1 Economic context and market application *20*
II.3.2 General introduction of the PIM process *22*
II.3.3 Advantages/disadvantages of the PIM process *25*
II.3.4 Materials used in feedstocks *26*
II.4 POWDER SINTERING, APPLICATION TO MIM SAMPLES 28
II.4.1 Mechanism of particle sintering *28*
II.4.2 Effect of the morphology of the powder *29*
II.4.3 Influence of the sintering on MIM samples *31*
II.4.4 Application to Inconel 718 ..... *31*
II.5 DEBINDING METHODS OF MIM FEEDSTOCKS 33
II.5.1 Solvent debinding *34*
II.5.2 Supercritical debinding *35*
II.5.3 Thermal debinding *36*
II.6 UNCONVENTIONAL SINTERING METHODS 38
II.6.1 Field Assisted Hot Pressing *38*
II.6.2 Microwave sintering *39*
II.7 PARTIAL REMARKS 42

REFERENCES **44**

III METHODS AND MATERIALS: RAW MATERIALS AND BULK MATERIAL CHARACTERIZATION METHODOLOGY **51**

III.1 RAW MATERIALS SELECTION 51
III.2 POWDERS CHARACTERIZATION 52
III.2.1 Morphology of the powders *52*
III.2.2 Laser Granulometry *54*

III.2.3 Specific surface analysis ... *56*
III.2.4 Powder rheology ... *57*
III.3 BINDERS CHARACTERIZATION ... 60
III.3.1 Thermal properties characterization ... *61*
III.3.2 Rheology of the binders ... *61*
III.4 MIM COMPONENT ELABORATION AND CONSOLIDATION ... 62
III.5 BULK MATERIAL CHARACTERIZATION ... 65
III.5.1 Microscopy ... *65*
III.5.2 Tensile strength tests ... *67*
III.5.3 Hardness characterization ... *68*
III.5.4 Nano-indentation test ... *69*
III.6 PARTIAL REMARKS ... 70

REFERENCES ... 71

IV CONVENTIONAL MIM PROCESS OF INCONEL 718 COMPONENTS ... 73

IV.1 FEEDSTOCK ELABORATION ... 74
IV.1.1 Mixing and Torque measurement ... *74*
IV.1.2 Thermal characterization ... *77*
IV.2 FEEDSTOCK INJECTION ... 79
IV.2.1 Feedstock rheology ... *79*
IV.2.2 Injection conditions ... *80*
IV.2.3 Thermal characterization ... *80*
IV.3 SOLVENT AND THERMAL DEBINDING ... 81
IV.3.1 Water solvent debinding ... *81*
IV.3.2 Thermal debinding ... *82*
IV.4 SINTERING OF THE MIM COMPONENTS ... 84
IV.4.1 Optimization of the sintering parameters ... *84*
IV.4.2 Application to all of the feedstocks ... *86*
IV.4.3 MIM component characterization ... *88*
IV.4.4 Thermal treatment of MIM sintered component ... *91*
IV.5 PARTIAL REMARKS ... 92

REFERENCES ... 94

V EXTRACTION OF PEG FROM INCONEL 718 MIM SAMPLE BY SUPERCRITICAL STATE CO_2 ... 96

V.1 SUPERCRITICAL FLUID DEBINDING PROCESS ... 97
V.1.1 Supercritical fluid debinding equipment ... *97*
V.1.2 Supercritical fluid debinding tests methodology ... *98*
V.1.3 Selectivity of the CO_2 in supercritical state ... *99*
V.2 OPTIMIZATION OF THE SUPERCRITICAL FLUID DEBINDING CYCLE ... 100
V.3 EFFECT ON THE SINTERING STEP AFTER A SUPERCRITICAL FLUID DEBINDING ... 103
V.3.1 Carbon and oxygen analysis ... *103*
V.3.2 Effect on the microstructure ... *103*
V.3.3 Roughness characterization ... *105*
V.4 PARTIAL REMARKS ... 106

REFERENCES ... 108

VI FIELD ASSISTED HOT PRESSING OF INCONEL 718 MIM COMPONENTS ... 109

VI.1 FAHP SINTERING PROCESS ... 110
VI.1.1 Description of the equipment ... *110*
VI.1 FAHP SINTERING OF INCONEL 718 POWDER ... 111
VI.1.1 Protective foil ... *111*
VI.1.2 Optimization of the pressure ... *113*
VI.1.3 Optimization of the temperature ... *114*
VI.1.4 Optimization of the heating rate ... *116*

VI.1.5 Optimization of the dwell time *118*
VI.1.6 Bulk material mechanical characterization *119*
VI.2 HEAT TREATMENT AFTER SINTERING. 121
VI.3 PARTIAL REMARKS 125

REFERENCES 126

VII MICROWAVE SINTERING AND HEAT TREATMENT 127

VII.1 MICROWAVE SINTERING 127
VII.1.1 Microwave equipment and methodology *127*
VII.1.2 Sintering of the MIM component *129*
VII.2 HEAT TREATMENT VIA PLASMA MICROWAVE 132
VII.2.1 Plasma microwave equipment and methodology *132*
VII.2.2 Plasma microwave sintering of MIM components *133*
VII.2.3 Plasma flame heat treatment *135*
VII.3 PARTIAL REMARKS 138

REFERENCES 139

VIII CONCLUDING REMARKS 140

LIST OF FIGURES

Figure I. 1 Example of components produced during the ProPIM project with the courtesy of Radial and ARaymond 3
Figure I. 2 Experimental work developed during this thesis 6
Figure II. 1 Thermal view of a turbofan CFM56 serie 3 9
Figure II. 2 Combustion chamber SuperDraco engine, 3D printed with Inconel by SpaceX [5] 10
Figure II. 3 OM of Microstructures of (a) as-cast, (b) wrought, and (c) wrought-grain-grown conditions [11] 11
Figure II. 4 SEM image of a γ' phase present inside a γ phase, obtained on a forged sample thermally treated at 760 °C for 50 hours and water quenched [13] 12
Figure II. 5 Dark field TEM image showing γ'' and γ' phases, obtained on a forged Inconel 718 sample, thermally treated at 700 °C for 524 hours [16] 12
Figure II. 6 OM of a δ phase developed in a forged Inconel 718 sample after thermal treatment at 870 °C during 50 hours. 13
Figure II. 7 SEM image of fusion zone micro constituents in Inconel 718, showing both the NbC and Laves phases [20] 13
Figure II. 8 TTT diagram of Inconel 718 [2] 15
Figure II. 9 DTA curves performed on an aged- wrought Inconel 718 at a heating rate of 5°C/min [6] 15
Figure II. 10 Effect of grain size and grain boundary microstructure on the creep crack growth rate at 650 °C [24] 16
Figure II. 11 Comparison between different materials of the yield stress in function of the temperature [25] 17
Figure II. 12 Powder metallurgy process route and European parts production by processing methods in 2016 (courtesy of EPMA) 18
Figure II. 13 Industrial sectors in Europe for MIM process and European MIM sales by material in 2016 (courtesy of EPMA) 20
Figure II. 14 Roadmap of economic batch size and shape complexity [38] 21
Figure II. 15 Raw material utilisation and energy requirements for different manufacturing techniques [38] 21
Figure II. 16 Description of the metal powder injection moulding 22
Figure II. 17 Effect of powder shape on the packing density [50] 23
Figure II. 18 Injection unit configuration [53] 24
Figure II. 19 Two-component tensile specimens of stainless steel/Stellite6 obtained by MIM [59] 26
Figure II. 20 Representation of defects produced during injection remaining during sintering [62] 26
Figure II. 21 Evolution of the specific surface and the densification rate in function of the temperature during solid phase sintering [74] 28
Figure II. 22 Molecular dynamic simulation of three tungsten particles during sintering [75] 29
Figure II. 23 Representation of porosity evolution during the sintering [74] 29
Figure II. 24 Effect of the particle size on the fractional density in function of the temperature [79] 30
Figure II. 25 Values of σ_{Lyp} plotted against the inverse square root of the grain diameter observed after aging treatment of mild steel (left) [81] and evolution of the grain size and of the density during sintering of a Fe-2Ni powder (right)[79] 30
Figure II. 26 Shrinkage evolution during sintering and volume modification before and after sintering [74] 31

Figure II. 27 Images of MIM samples after sintering showing deformations [82] and cracks [46] ..31
Figure II. 28 Description of the solvent debinding in the case of PEG elimination by water. A: component after moulding injection. B: Start of the progressive diffusion of water inside the binder C: Progressive elimination of the PEG and apparition of porosity inside the component. D: Final state after complete solvent debinding with primary binder back-bone around the particles and porosity channels created through the component [86] 34
Figure II. 29 Phase diagram of the carbon dioxide [93]and evolution of Carbon dioxide properties in function of the pressure [94] 36
Figure II. 30 Defects observed on MIM samples after wax debinding with supercritical CO_2 and heptane [95]..... 36
Figure II. 31 Decomposition curves of a wax-PP-PE based feedstock and of each of its elements [99] 37
Figure II. 32 Energy dissipation in the microscopic scale [111] 39
Figure II. 33 Conventional and MW induced heating patterns [115] 40
Figure II. 34 Evolution of the Skin depth in function of the temperature for different metals [117] 40
Figure II. 35 Dissipation of the energy brought by the microwaves by hotspots [120]..... 41
Figure II. 36 Optical micrographs of two sets of 'green' (un-sintered) and microwave sintered powdered–metal parts processed at 1,200 °C for 30 minutes[124] 41
Figure II. 37 Types of microwave heating (a) direct heating, (b) selective heating and (c) hybrid heating [125] 42

Figure III. 1 OM images and SEM image of the commercial powder (Inconel 718 S)..... 53
Figure III. 2 OM images (above) and SEM image (below) of the milled powder (Inconel 718 M) .53
Figure III. 3 Typical set up of a laser granulometer [11] 54
Figure III. 4 Differential distribution (a) and cumulative distribution (b) in function of the particle diameter of Inconel 718 S 55
Figure III. 5 FT4 powder rheometer (A) and the shape of the blade used during the tests (B) 57
Figure III. 6 Compressibility of the powders in function of the normal stress applied during the compressibility test 58
Figure III. 7 Pressure drop inside the powders in function of the normal stress applied during the permeability test 59
Figure III. 8 Energy needed for the rotation of the blades inside the powders in function of the air flow rate applied during the ventilation test..... 59
Figure III. 9 Shear viscosity in function of the shear viscosity obtained by rotating and capillary rheometers of the different elements composing the binder 62
Figure III. 10 Equipment used during conventional MIM process: a) Brabender Plastograph EC W50EHT, b) Arburg 220S, c) solvent debinding set-up, d) Setaram Setsys EVO 2400..... 63
Figure III. 11 SEM images of a sintered Inconel 718 MIM component taken before and after EP ..65
Figure III. 12 schematic diagram of a conventionally prepared FIB TEM specimen [27]..... 67
Figure III. 13 Drawings of the samples for the micro-tensile strength tests 67
Figure III. 14 Tensile strength test and micro-tensile strength test equipment..... 68
Figure III. 15 Example of Vickers footprint obtained on Inconel 718 samples..... 69
Figure III. 16 Schematic illustration of indentation load–displacement data showing important measured parameters[33] 69
Figure IV. 1 Mixing torque vs time during the elaboration of the feedstock composed of binder B with the spherical powder 75
Figure IV. 2 elaboration of the feedstock composed of binder A with the flake shape powder..... 76
Figure IV. 3 TGA results on the prepared feedstocks from 0 to 600 °C at 2 °C/min in argon atmosphere 77

Figure IV. 4 Shear viscosity vs Shear rate of the prepared feedstock at 180 °C with a shear die channel of 1 mm and 16 mm length 79
Figure IV. 5 TGA results for the injected components. Left side is the cylinder composed of Binder A + Inconel S 718 62 %, right side is the bar composed of Binder B + Inconel S 718 62 % 81
Figure IV. 6 Water debinding of the feedstocks at 30 °C in function of the time 82
Figure IV. 7 Water debinding of the feedstocks prepared during 72 hours in function of the temperature 82
Figure IV. 8 Shrinkage vs Time during a debinding cycle from 0 to 600°C at 1 °C /min of binder A +Inconel 718 S 62 % 83
Figure IV. 9 TGA results after performing a thermal debinding cycle on a component binder A +Inconel 718 S 62 % 83
Figure IV. 10 Maximum shrinkage vs temperature after sintering of binder A+ Inconel 718 S 71 % at different temperatures during 2 hours under argon atmosphere 85
Figure IV. 11 OM images of the sintered component binder A + Inconel 718 S 71 % at (a) 850 °C, (b) 1000 °C, (c) 1200 °C, (d) 1250 °C, (e) 1275 °C, (f) 1290 °C during 4 hours 85
Figure IV. 12 Dilatometry curves performed on Binder A+ Inconel 718 S 71 % at 1290 °C maintained at different times under argon atmosphere 86
Figure IV. 13 Dilatometry curves performed on the injected components at1290 °C for 2 hours and 5 °C/min under argon atmosphere 87
Figure IV. 14 OM image of sintered component of a) binder A + Inconel 718 S 62 %, b) binder A + Inconel 718 S 71 %, c) binder B + Inconel 718 S 62 %, d) binder A + Inconel 718 M 55 % 88
Figure IV. 15 SEM images of the furnace sintered at 1290 °C during 4 hours after electro-polishing of (a) binder A + Inconel 718 M 55 % and (b) binder A + Inconel 718 S 62 % 89
Figure IV. 16 Tensile strength test of the sintered component binder A + Inconel 718 S 71 % 90
Figure IV. 17 SEM images obtained during an in-situ tensile strength test at (a) 0 MPa, (b) 800 MPa (c) breaking point and (d) is the rupture profile of the broken sample 90
Figure IV. 18 SEM image of sintered component binder A + Inconel 718 S 62 % after thermal treatment at 720 and 620 °C during 8 hours each 91
Figure IV. 19 Time repartition of the conventional MIM process 93
Figure V. 1 Description of the equipment and CO_2 diagram phase 97
Figure V. 2 Example of the evolution of the pressure and the temperature vs time during the tests 98
Figure V. 3 IR spectrum of each elements of Binder A, after injection and CO_2 in supercritical state debinding 99
Figure V. 4 Quantity of PEG removed vs pressure at 50 °C and vs temperature at 50 MPa, both during 4 hrs after supercritical fluid debinding of binder A + Inconel 718 S 62 % 100
Figure V. 5 Quantity of PEG removed vs pressure at 50 °C and vs temperature at 50 MPa, both during 4 hrs after supercritical fluid debinding of binder A + Inconel 718 S 62 % 101
Figure V. 6 Quantity of PEG removed in function of the pressure at 150 °C after supercritical fluid debinding of binder A + Inconel 718 S 62 % (image a) before and c) after debinding) and binder A + Inconel 718 M 55 % (image b) before and d) after debinding) 102
Figure V. 7 TGA curves under argon atmosphere and 5 °C/min of the components after supercritical fluid at the optimized conditions 102
Figure V. 8 OM images of binder A + Inconel 718 S 71 %, sintered at 1290 °C during 4 hours, after supercritical fluid debinding at 150 °C, 40 MPa during 4 hours (a and b) and water debinding at 50 °C during 72 hours (c and d) 104
Figure V. 9 OM images of binder A + Inconel 718 M 55 %, sintered at 1290 °C during 4 hours, after supercritical fluid debinding at 150 °C, 50 MPa during 4 hours (above) and water debinding at 50 °C during 72 hours (below) 104
Figure V. 10 Roughness results after each treatments on the MIM samples 105

Figure V. 11 3D Roughness profile of sintered samples debinded by supercritical CO_2 and in water 105
Figure V. 12 Time repartition of the MIM process after using supercritical debinding 107
Figure VI. 1 Gleeble 3800 representative system 110
Figure VI. 2 Example of FAHP sintering cycle applied at each tests 111
Figure VI. 3 Shrinkage and rate of shrinkage vs temperature during SPS sintering of Inconel 718 powder at 50 °C/min maintained 5 minutes 112
Figure VI. 4 SEM images obtained after sintering at 1200 °C during 5 min at 50 °C/min 113
Figure VI. 5 Images of the sample a) debinded at 600 °C during 2 hours b) sintered by FAHP at 50 MPa and c) 10 MPa, both at 1250 °C during 10 min 114
Figure VI. 6 Rate of shrinkage vs sintering time during FAHP sintering of Inconel 718 S powder maintained 10 minutes and under 50 MPa 114
Figure VI. 7 OM images of the samples sintered by FAHP at a)1100°C, b) 1200°C and c) 1250°C at 50 °C/min 115
Figure VI. 8 SEM images of MIM component sintered at 1250 °C under 10 MPa at 50 °C/min during 10 minutes 115
Figure VI. 9 Shrinkage vs time during FAHP sintering at 1250 °C of Inconel 718 S powder at different heating rate 116
Figure VI. 10 SEM image after electro-polishing of MIM component sintered at 1250 °C, 300 °C/min under 10 MPa during 10 minutes 117
Figure VI. 11 Rate of shrinkage vs time during FAHP sintering at 1250 °C, 300 °C/min under 10 MPa at different dwell times 118
Figure VI. 12 SEM images of MIM component sintered at 1250 °C under 10 MPa at 50 °C/min during 10 minutes 118
Figure VI. 13 Tensile strength test of the FAHP sintered component Binder B + Inconel 718 S 62 % at 1250 °C maintained during 10 and 15 min 119
Figure VI. 14 SEM images obtained at different tensile stress of the FAHP sintered components at 1250 °C, 300 °C/min under 10 MPa and during a) 10 min and b) 15 min 121
Figure VI. 15 Thermal treatment applied with FAHP equipment to a MIM component 121
Figure VI. 16 SEM images of MIM component sintered at 1250 °C under 10 MPa at 50 °C/min during 10 minutes a) before and b) after electro-polishing 122
Figure VI. 17 (a) SAD pattern identified as the zone [111]γ axis for the matrix and (b) to (f) TEM images of Inconel 718 62% + binder B sintered by FAHP at 1250 °C at 100 °C/min, during 15 min and a second FAHP cycle applied at 750 °C, 100 °C/min during 15 min 123
Figure VI. 18 EDX analysis performed with TEM on a grain of Inconel 718 62% + binder B sintered by FAHP at 1250 °C at 100 °C/min, during 15 min and a second FAHP cycle applied at 750 °C, 100 °C/min during 150 mins 124
Figure VII. 1 Microwave single cavity mode equipment from Sairem 128
Figure VII. 2 Three set-up used during the microwave sintering tests: a) alumina support, b) surrounded by alumina powder and c) graphite die and tungsten foil surrounded by alumina powder 129
Figure VII. 3 Electric arcs created during tests around 700 °C at 0.80 kW during microwave irradiation with set-up a) and Paschen law curves of different pure gas 130
Figure VII. 4 Electric arcs created during microwave irradiation appearing at temperatures around 1000 °C and picture of the damaged component after the test 130
Figure VII. 5 Images of the evolution of the temperature during the microwave irradiation at 1.0, 2.0 and 3.0 kW with set-up c) 131
Figure VII. 6 Plasma microwave equipment from Sairem 132

Figure VII. 7 Evolution of the temperature and the microwave power in function of the time during plasma microwave sintering of Inconel 718 MIM component 134
Figure VII. 8 Optical Microscopy images of the samples sintered by microwave sintering during a) 30min and b) 60min 135
Figure VII. 9 Mapping of the measured Young modulus (above) and of the hardness (below) obtained after nano-indentation on plasma sintered Inconel 718 MIM component 135
Figure VII. 10 SEM image of Plasma microwave thermal treatment at 750 °C during 30 min of a sintered Inconel 718 MIM component and EDX mapping of the image 137

LIST OF TABLES

Table I. 1 Project specifications and properties at room temperature of the considered materials 4
Table II. 1. Chemical composition in mass percentage of the Inconel 625 & 718 powder 11
Table II. 2 Reactions temperatures obtained on a wrought Inconel 718 sample [20].....14
Table II. 3 Tensile properties of Inconel 718 forged discs at room temperature (RT) and at a high temperature [2].....16
Table II. 4 Grain size and hardness variation of Inconel 718 at different thermal treatments [6] 17
Table II. 5 Technologies involved in the MIM process 19
Table II. 6 List of binders in literature 27
Table II. 7 List of the results during sintering MIM Inconel 718 samples 32
Table III. 1 Data on the powders provided by the suppliers 52
Table III. 2 data on the polymers provided by the supplier 52
Table III. 3Diffraction equivalent diameters obtained by laser granulometry of Inconel 718 S 55
Table III. 4 Specific surface measured on Inconel 718 spherical and flake shape powders and calculated diameters 56
Table III. 5 Composition of the binders A and B.....60
Table III. 6 Temperatures of fusion and degradation of the polymers 61
Table III. 7 Technical specifications of the Arburg 220S.....64
Table IV. 1 Mixing torque obtained during the elaboration of the feedstock composed of binder B with the spherical powder 76
Table IV. 2 Mixing torque obtained during the elaboration of the feedstock composed of binder A with the spherical powder 77
Table IV. 3 Weight loss of the feedstocks after TGA from 0 to 600 °C under argon atmosphere....78
Table IV. 4 Density and hardness obtained at different sintering temperature for binder A + Inconel 718 S 71 %.....86
Table IV. 5 Density and hardness obtained for the different feedstock sintered at1290 °C for 2 hours and 5 °C/min under argon atmosphere.....88
Table IV. 6 EDX analysis of the zones marked on Figure IV. 15 89
Table IV. 7 Mechanical properties obtained from the tensile strength test of the sintered component binder A + Inconel 718 S 71 %.....90
Table IV. 8 EDX analysis of the zones marked on Figure IV. 18 92
Table V. 1Carbon and Oxygen rates inside the powder after solvent or supercritical fluid and thermal debinding.....103
Table VI. 1 EDX analysis of the zones marked on Figure VI. 4 113
Table VI. 2 EDX analysis of the zones marked on Figure VI. 8 116
Table VI. 3 EDX analysis of the zones marked on Figure VI. 10 117
Table VI. 4 Density and hardness obtained after different FAHP sintering cycles under a pressure of 10 MPa 119
Table VI. 5 Mechanical properties obtained from the tensile strength test of the sintered component by FAHP and compared to the conventional MIM components 120
Table VI. 6 Hardness measurements after plasma microwave thermal treatment at 750 °C.....136

LIST OF ABREVIATION AND SYMPOLS

PIM	Powder injection moulding
MIM	Metal Injection moulding
MW	Microwaves
MWHH	Microwaves hybrid heating
FAHP	Field Assisted Hot pressing
HIP	Hot isostatic pressing
FIB	Focus ion beam
EP	Electro-polishing
CAB	Cellulose acetate butyrate
PP	Polypropylene
PEG	Polyethylene glycol
SA	Stearic acid
PTZ	Phenothiazine
BET	Brunauer, Emmett & Teller
DSC	Differential scanning calorimetry
TGA	Thermogravimetric analysis
LOM	Light optical microscopy
SEM	Scanning electron microscopy
TEM	Transmission electron microscopy
EDX	Energy dispersive X-ray spectrometry
HV	Vickers hardness
UTS	Ultimate tensile strength
YS	Yield stress
E	Young modulus

ABSTRACT

Powder injection moulding is a mature manufacturing process used for mass producing small size and complex geometry components. It is a competitive and effective alternative to the forging and casting methods as it produces near net shape components with a low raw material consumption. Thus it is even more effective with expensive materials. The expansion of the PIM requires extensive research in new materials but also of the manufacturing process itself.

The PIM process employs debinding and sintering methods with high time and energy consumption. The environmental awareness of both industrials and customers is pushing for a reduction of these conditions. Within the PIM process, there are two possibilities to find alternatives. One of those would consist to find alternatives to the equipment and methods employed at the moment.

This PhD thesis studied the replacement of the debinding and sintering methods by unconventional one with better kinetics. The supercritical fluid debinding, the FAHP sintering and the microwave sintering are three methods developed for faster performances and were applied to PIM components in order to reach at least the same results as the conventional methods.

This project was developed in collaboration with industrials interested on the elaboration of Inconel 718 parts. The scope of this work is the study and the comprehension of the behaviour of these components while they are treated with these three unconventional methods. With regard to this matter, the formulation and the elaboration of the components is first introduced. Different feedstocks with different powder morphology, a spherical and an irregular flake shape were used. A PP based binder and a CAB based binder were also used. Hence, the homogeneity, the optimum powder volume loading, the thermal and rheological behaviour of both the raw materials and mixtures were all determined in order to perform the tests with the best starting conditions.

The first chapter of this thesis introduces the superalloys and more precisely the nickel-chrome superalloys. The composition, the microstructure and the thermal behaviour of the Inconel 718 was thoroughly investigated. It is followed by an introduction to the powder metallurgy, the MIM process and the research performed on Inconel 718 MIM components. The final part of this chapter presents the three new unconventional methods.

The second chapter presents the raw materials used during this work and their characteristics. The methods employed to obtain the different mechanical, thermal and chemical properties are also

introduced. The following chapter presents the results of the application of the conventional MIM process on the MIM components. The first step is the progressive extraction of the polymers composing the binders with first a water debinding step of the PEG followed by a thermal degradation of the remaining organic compounds. The brown part is then sintered via a furnace and a thermal treatment of the metallic compound is concluding the process. All of the steps are optimized in order to reach the best performances of the material.

The next chapter introduces the supercritical fluid debinding method in order to replace the water extraction. The equipment and the methods are presented with the objectives to extract all of the PEG introduced during the elaboration of the feedstock. The quality of the final component is characterized by its surface roughness.

The FAHP sintering and the thermal treatment were performed on fully debinded Inconel 718 MIM components. The methods needed an adaptation to the MIM component and the material in order to avoid geometry deformation and microstructure pollution. The effects on the final components, its mechanical performances and its microstructures, were investigated in order to understand the effects of the method on the MIM components.

The last chapter presents the results observed during the microwave irradiation of the Inconel 718 components. A second method, using a plasma microwave flame, was used to perform thermal treatments on the components. The results on the microstructure and the mechanical performances were investigated via nano-identation tests.

I INTRODUCTION

I.1 Context of the PhD project

Powder Injection Moulding (PIM) is a process that have undergone for the last twenty years, along with a huge development in the industrial sector. It has generated many research project and scientific communications. Most of them brought technologic development for industrial applications for small complex components elaboration. In the case of Metal Injection Moulding (MIM), the most developed material is the stainless steels such as grades 316L [1] or 17-4PH [2] in numerous fields like watchmaking, military, aeronautics or automotive industry [3].

The MIM process needs knowledge in multiple fields as it combines the advantages from both thermoplastic moulding injection and powder metallurgy. Thus, the development of a component implies a reflexion at every step of the process and on materials. It goes from the selection of the polymers for their rheological and thermal behaviour, to the morphology of the powder and its behaviour during injection and sintering.

On top of the process, the industrial context is also changing, as the environmental and economic politics are more demanding. The economic context is tougher with a fierce competition between the different markets and are pushing manufacturers to reduce the cost of production. On top of this race to cheap production costs, environmental laws are stricter and industries need to be adapted to new standards. A lot of research programs are now engaged in order to bring solutions to both problems at the same time.

In France, a FUI (Fonds unique interministériel) is a program directed by the Ministry of Economy, Industry and Employment. It was made to help to develop collaborative research projects and development between industries and research centres, in order to bring innovative products and services on the market at short or medium term.

The project FUI ProPIM was brought by Eurotungstene and the objective were to develop MIM with French actors MIM technology for high performance products with high accuracy tolerance. The project brings together 9 actors that are from a powder manufacturer (Eurotungstene), a plastic manufacturer and a plastic industry development research centres (VP Plast and IPC), a mould manufacturer (SA. Vuillermoz Philippe), an injection system manufacturer (Runipsys), two industrial

parts manufacturers (Radiall and ARAymond) and two research centres (CEA LITEN and FEMTO-ST institute).

This project, started in 2013, aims to develop solutions to technologic issues linked to components and micro-components manufacturing with high precision dimensions, high production rate, and good specific properties. Three working areas were developed: Material, Tools and Process.

Two PhD research projects were financed by ProPIM inside the FEMTO-ST institute. One of them was for the Material part [4] and the second for the Process Part, which oriented the works presented in this manuscript.

The research was developed with the collaboration between two university research groups. The first one is the French group 2PC (Polymer and high loaded polymers), which is part of the Applied Mechanics Department of the FEMTO-ST institute. The second one is the Spanish group GTP (Group of Powder Technology) which belongs to the Department of Materials Science and Engineering of the University Carlos III of Madrid.

The 2PC group is directed by two permanent professors and the principal research activity is the development of components and micro-components with functional properties, obtained by injection moulding or hot embossing. These polymers can be loaded with micro or nano particles with metallic or ceramic particles. The research developed by the group are mainly concentrated on the MIM process from the feedstock elaboration [4], Injection analysis [5], debinding and sintering in both experimental and numerical work [6], [7].

The GTP group is composed by six permanent professors and most of the research activities of the group have in common the use of powder technology for materials development, from the synthesis of nanoparticles to the application of smart coatings for several industrial sectors. They are also working in the processing of materials by powder metallurgy techniques, the design of new alloys and the study of interactions between phases and coatings. They also developed projects around the global optimization of the MIM process [8], [9].

In this manuscript the presented topic is first devoted to the influence of the debinding method of the MIM samples and the impact of the process used on the quality of the obtained components. Secondly, two different ways of sintering were investigated. They are qualified as “unconventional” as they are using different thermal phenomenon in order to obtain the sintering temperatures. One of them is the Field Assisted Hot Pressing (FAHP) sintering, which uses an alternative electric current,

and the other is the microwave (MW) assisted sintering, using microwave wavelengths to excite the particles.

I.2 Specifications of the project

I.2.1 Choice of the material

One of the goals of the project is to produce components for aeronautic applications (Figure I. 1). During the elaboration of the project, the first specifications of the material were related to the mechanical properties, as it will be used under huge solicitations during its life time. The second requirement was a good corrosion resistance, and more specifically at high temperatures. In terms of the alloy composition, the first materials that were investigated were stainless steels such as 17-4PH [10] and A286 [11]. That kind of material displays interesting mechanical characteristics compared to requirements. However, the application of the component imposed a last condition, which is a non-magnetic character. Both Ferritic materials as the 17-4PH became impossible to be used and Nickel alloys was one of the materials that could fulfil all the required conditions [12].

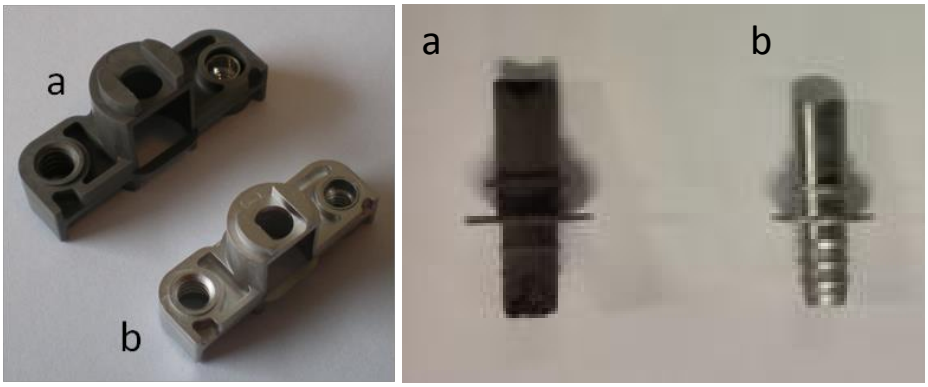

Figure I. 1 Example of components produced during the ProPIM project with the courtesy of Radial and ARaymond

Specifications are also coming from the complex shape of the components. The presence of a thread and thin walls brought the necessity to have a precision of at least 100 µm. That kind of finishing specification can only be obtained with fine powder granulometry and the proper morphology [13], which are difficult to find on the market. The A286 is a stainless steel grade with 25.5 (wt.) % of nickel and 13.5 (wt.) % of chrome, and thanks to the huge rate of nickel, is an austenitic material, then non-magnetic. This material can reach good mechanical properties after undergoing a thermal treatment. A previous study from the partners of the project demonstrates some

troubles to obtain the good mechanical properties by applying thermal treatments. The Inconel 625 and 718 are both Nickel-Chrome superalloys developed for the aeronautic industry. Then, they were developed for their high mechanical and corrosion behaviour at ambient and high temperatures. Because of the different hardening mechanisms, the Inconel 718 exhibits the best mechanical performances between the two considered alloys. By combining all these factors (Table I. 1), Inconel 718 is the material that will be investigated.

Table I. 1 Project specifications and properties at room temperature of the considered materials

	Project specifications	17-4PH	A286	In625	In718
UTS (MPa)	> 700	1350	1045	900	1200
0,2 PS (MPa)	> 500	1300	640	450	1000
Elongation (%)	> 12	5-12	21.7	50	12
Magnetism	no	Yes	no	no	no

I.2.2 Investigation of new processing methods for MIM samples

As previously introduced, the industrial needs for more economic and ecologic process are a huge concern. In the case of the MIM process, a low material loss during the production and a high rate of production is allowed to reduce the production costs. It is even more important in our case, with the use of expensive materials such as Inconel 718. This kind of material is tough to machine and to damage faster the tools [14]. Moreover, there is also an unavoidable risk of damaging the components while the forging process.

However, the MIM process has also weaknesses. The first problem is to be able to master every steps of the process in order to avoid defects [15]. Another one is the wastes coming from the use of organic solvents in order to get rid of the polymers. A part of the project that was inside the material axis was the development of binders composed by bio-sourced polymers. The second part was to find an alternative process to solvent debinding.

The supercritical fluids are at the moment used for component extraction perfume industry or cleaning mechanical parts. It is only recently that it was investigated for polymer extraction inside MIM samples [16]. The advantages of using them is to avoid solvent wastes, which needs to be recycled and treated. A new equipment was acquired by the research group 2PC for this project via the equipex platform MIFHysTO. The effects of using these methods need to be investigated, as it can impact the structure of the particles of the MIM samples or leave a significant carbon residue.

The last steps of the MIM process are the sintering and the thermal treatment of the metallic powders. They are performed inside furnaces and consumes a lot of time and energy in order to obtain a complete densification of the parts [17]. New sintering methods were developed in order to reduce the impact of this conventional way. Even so, they still need to be adapted to the requirements of the MIM samples, and more precisely, the complex geometry. Thus, two sintering methods were considered and briefly described in the following paragraphs.

The assisted microwave (MW) sintering is a method used for ceramics [18]. Metals are considered insensitive to micro-wavelengths, but studies showed that if the material is in a powder state, they were able to penetrate and heat the material [19]. Thanks to this, it was possible to obtain high heating rate and shortened sintering time.

The Field Assisted Hot Pressing (FAHP) sintering is a method using strong alternative currents in order to rise the temperature of conductive materials [20]. At the time the use of superalloys with this method was not investigated, but it presents the same kind of advantages as the microwave sintering. Moreover, as it is performed under pressure, it is also have an impact on the properties of the materials processed [21]. In order to find an alternative to the furnace sintering, these two methods were chosen in order to study the compatibility with a Inconel 718 MIM sample.

I.3 Experimental work developed for the project

Figure I. 2 introduces the experimental procedures followed during the thesis work. The raw materials used to elaborate the component and the selection criteria according to their intrinsic properties are also introduced. The successive steps of the MIM process are all linked with the different parameters that needs to be determined and with the different equipment and characterization method used to identify them. The first step is to determine the characteristics of the raw materials in order to prepare the first step of the MIM process. Each stage of this process is dependant of the previous one and have to be developed consecutively. Therefore, defects derived from a previous stage is impacting the subsequent stage, forcing to start over the previous optimization process. The introduction of the supercritical fluid debinding, the microwave sintering and the FAHP sintering is implying a different effect on the raw materials. Hence, the different characterization methods need to be performed in the same conditions in order to be able to compare the properties of the different components.

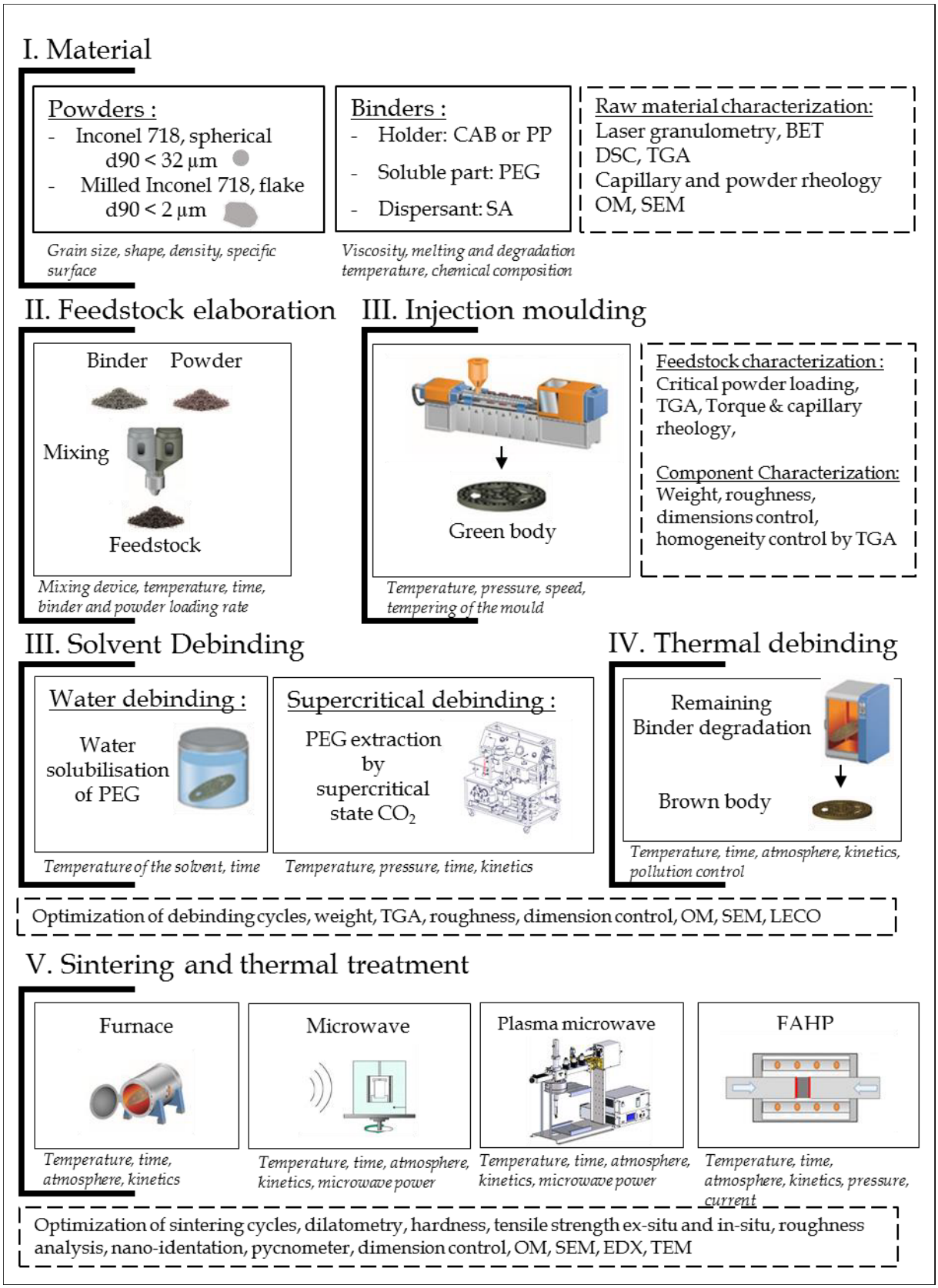

Figure I. 2 Experimental work developed during this thesis

REFERENCES

[1] M.-S. Huang Et H.-C. Hsu, « Effect Of Backbone Polymer On Properties Of 316l Stainless Steel Mim Compact », J. Mater. Process. Technol., Vol. 209, Nº 15–16, P. 5527‑5535, Août 2009.

[2] B. N. Mukund, B. Hausnerova, Et T. S. Shivashankar, « Development Of 17-4ph Stainless Steel Bimodal Powder Injection Molding Feedstock With The Help Of Interparticle Spacing/Lubricating Liquid Concept », Powder Technol., Vol. 283, P. 24‑31, Oct. 2015.

[3] Inovar Communications Ltd, « Pim International », Vol. Vol-10, Nº No-4, Déc-2016.

[4] A. Royer, « Etude, Caractérisations Et Développement De Mélanges De Polymères Biosourcés Chargés De Poudre D'inconel 718 Pour L'élaboration De Composants Et Micro-Composants Via Moulage Par Injection De Poudres Métalliques », Université De Franche-Comté, 2016.

[5] D. Claudel, « Modélisation Et Identification De Lois Rhéologiques De Polymères Chargés. Application Au Procédé De Moulage Par Injection De Poudres De Superalliages. », Université De Franche-Comté, 2016.

[6] M. Belgacem, « Experimental Investigation And Numerical Simulation Of Thermal Debinding And Sintering Processes In Powder Injection Moulding. », Université De Franche-Comté, 2013.

[7] P. Tourneroche, « Développement De Mélanges Chargés En Poudres D'aluminure De Titane Pour Moulage Par Injection Et Applications Aéronautiques », Université De Franche-Comté, 2016.

[8] A. Páez Pavón, « Desarrollo De Nuevos Sistemas Ligantes De Eliminación De Catalítica Para Moldeo Por Inyección De Polvos », Universidad Carlos Iii De Madrid, 2016.

[9] C. Abajo Clemente, « Development And Optimization Of An Eco-Friendly Binder System For Ceramic Injection Moulding Of Zirconium Silicate », Universidad Carlos Iii De Madrid, 2016.

[10] H. Ye, X. Y. Liu, Et H. Hong, « Sintering Of 17-4ph Stainless Steel Feedstock For Metal Injection Molding », Mater. Lett., Vol. 62, Nº 19, P. 3334‑3336, Juillet 2008.

[11] H. De Cicco, M. I. Luppo, L. M. Gribaudo, Et J. Ovejero-García, « Microstructural Development And Creep Behavior In A286 Superalloy », Mater. Charact., Vol. 52, Nº 2, P. 85‑92, Mai 2004.

[12] E. W. Collings, F. J. Jelinek, J. C. Ho, Et M. P. Mathur, « Magnetic And Thermal Properties Of Stainless Steel And Inconel At Cryogenic Temperatures », In Advances In Cryogenic Engineering, Springer, 1977, P. 159–173.

[13] K. Okubo, S. Tanaka, Et H. Ito, « The Effects Of Metal Particle Size And Distributions On Dimensional Accuracy For Micro Parts In Micro Metal Injection Molding », Microsyst. Technol., Vol. 16, Nº 12, P. 2037‑2041, Déc. 2010.

[14] A. Thakur Et S. Gangopadhyay, « State-Of-The-Art In Surface Integrity In Machining Of Nickel-Based Super Alloys », Int. J. Mach. Tools Manuf., Vol. 100, P. 25‑54, Janv. 2016.

[15] K. S. Hwang, « 10 - Common Defects In Metal Injection Molding (Mim) A2 - Heaney, Donald F. », In Handbook Of Metal Injection Molding, Woodhead Publishing, 2012, P. 235‑253.

[16] T. Chartier, M. Ferrato, Et J.-F. Baumard, « Influence Of The Debinding Method On The Mechanical Properties Of Plastic Formed Ceramics », J. Eur. Ceram. Soc., Vol. 15, Nº 9, P. 899‑903, 1995.

[17] J. J. Valencia, « Sintering Effect On The Microstructure And Mechanical Properties Of Alloy 718 Processed By Powder Injection Molding », Miner. Met. Mater. Soc., Vol. Superalloys 718,625,706 And Various Derivatives, 1997.

[18] D. K. Agrawal, « Microwave Processing Of Ceramics », Curr. Opin. Solid State Mater. Sci., Vol. 3, Nº 5, P. 480‑485, Oct. 1998.

[19] R. Roy, D. Agrawal, J. Cheng, Et S. Gedevanishvili, « Full Sintering Of Powdered-Metal Bodies In A Microwave Field », Nature, Vol. 399, Nº 6737, P. 668‑ 670, Juin 1999.
[20] J. Langer, M. J. Hoffmann, Et O. Guillon, « Direct Comparison Between Hot Pressing And Electric Field-Assisted Sintering Of Submicron Alumina », Acta Mater., Vol. 57, Nº 18, P. 5454‑ 5465, Oct. 2009.
[21] L. Minier, S. Le Gallet, Y. Grin, Et F. Bernard, « A Comparative Study Of Nickel And Alumina Sintering Using Spark Plasma Sintering (Sps) », Mater. Chem. Phys., Vol. 134, Nº 1, P. 243‑ 253, Mai 2012.

II INTRODUCTION TO THE NICKEL-CHROME SUPERALLOYS, THE MIM PROCESS AND THE UNCONVENTIONAL SINTERING PROCESSES

The use of Inconel 718 for industrial applications was introduced in the late 60's. It was then used as a component for feedstocks in the late 90's [1]. In order to introduce the works developed in this manuscript, a description of the material is presented. It will be followed by an introduction to the MIM process, with the different steps needed to produce metal parts and the specifications of the process. Then the different methods that will have an impact on the particles and their sintering process will be studied. Thus, the theory and the experimental work behind the powder metallurgy applied to the MIM samples will help analysing that impact on our material. The last two parts are devoted to introduce a state of the art of the research that was performed with the investigated methods in this manuscript.

II.1 Nickel based superalloys and Inconel 718

II.1.1 Application of the Nickel based superalloys

Superalloys started because of the needs in aeronautic engines. They are complex machines, where mechanical and thermal solicitations are colluding at high level for long time periods (Figure II. 1).

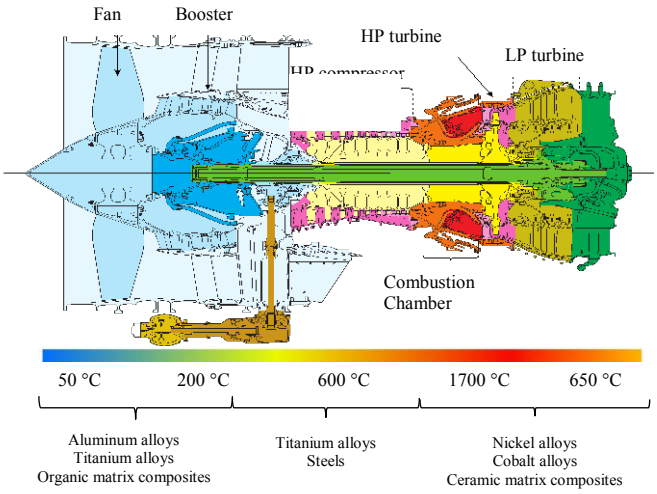

Figure II. 1 Thermal view of a turbofan CFM56 serie 3

In order to answer to these needs, high performance materials were designed in order to survive these harsh environments. From the 70's and the 80's, three main families of metallic alloys for critical conditions such as steels, titanium alloys and nickel alloys were developed. Intensive research activity on these materials allows materials with good characteristics and high reliability [2]. Thanks to the mechanical behaviour of these materials, combined with air cooling systems and thermal barrier, it allowed the development of engines with high performances. Since its creation, the use of these materials was completely diversified and used in aerospace (Figure II. 2), automotive, petrol and nuclear industry [3], [4].

Figure II. 2 Combustion chamber SuperDraco engine, 3D printed with Inconel by SpaceX [5]

II.1.2 Composition of Inconel 718

The composition of the two types of Inconel introduced in the specification of the project is presented in Table II. 1. The main difference between the two of them is the nickel content. It is less important inside the 718 nuance and is compensated with more iron. It will drastically increase the Young modulus and the yield stress [6]. But the limitation of the nickel content reduces the corrosion resistance capability. The chrome present inside the composition is strengthening the oxidation resistance. The molybdenum helps to increase the hardening of the γ austenitic matrix at 20 °C but also at high temperatures. Niobium is responsible for the formation of the hardening phase γ''[7], which is developed in part II.1.3. That phase increases the hardness and the yield strength of Inconel. The more niobium is present in the composition, the more it is increased, until a limit around 5% in mass. Thus, Inconel 718 is including the maximum allowed for this kind of alloy. Titanium and aluminium are elements responsible for the formation of a γ' phase [8], also developed in the next

part. This phase is also responsible for the hardness of the structure, but at a lesser degree than the γ''. Depending on the thermal treatment, the γ'' phase can be four times more important than the γ'.

Table II. 1. Chemical composition in mass percentage of the Inconel 625 & 718 powder

Alloy	Ni	Fe	Cr	Mo	Al	Ti	Nb	C
In 625	61.00	2.50	21.50	9.00	0.20	0.20	3.60	0.05
In 718	52.5	19.00	19.00	3.00	0.50	0.90	5.30	0.05

II.1.3 Structure of Inconel 718

With the importance that took Inconel 718 in the aircraft industry, a lot of investigations of its structure were performed on casted and forged samples [2], [6], [9], [10].The optical microstructures of as-cast, wrought and wrought-grain-grown samples are illustrated in Figure II. 3.

In the as-cast case, the structure presents two types of distinct constituents, which are Laves phases and carbides. The formation of these two phases and their thermal behaviour will be described in the next parts. In the wrought sample, thanks to a homogenization coming from mechanical and thermal treatments, these two constituents are reduced or eliminated. The structure does not have twinned grains. In order to bring out the best mechanical performances a thermal treatment was applied to the material. A larger but similar structure is obtained, despite the grains containing small and uniform dendrites.

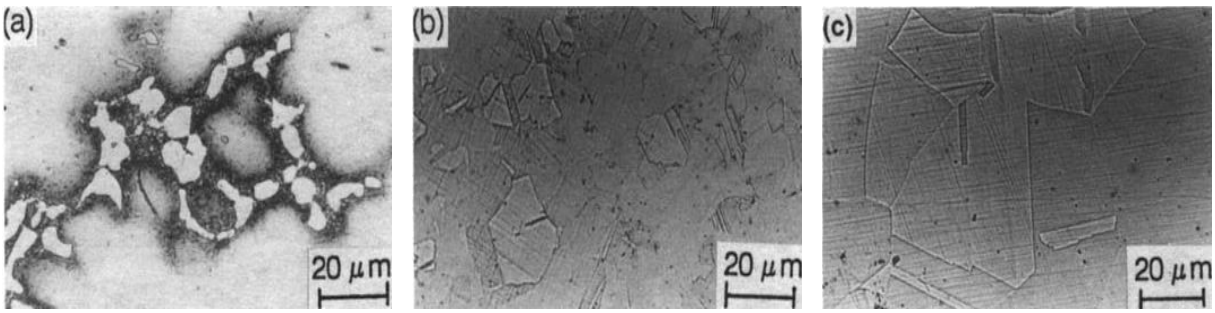

Figure II. 3 OM of Microstructures of (a) as-cast, (b) wrought, and (c) wrought-grain-grown Inconel 718 [11]

Nickel based superalloys have a γ austenitic matrix hardened with different phases developed inside it. The different phases present inside the In718 alloy was investigated and determined by Sundararaman et al. [12].

There are four main phases:

- γ matrix present in Face Cubic Centered (FCC), solid solution
- γ' phase present in Simple Cubic (SC), Ni_3 (Al,Ti), present on Figure II. 4 as spherical-like shapes.

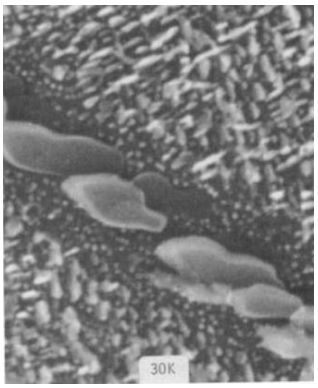

Figure II. 4 SEM image of a γ' phase present inside a γ phase, obtained on a forged sample thermally treated at 760 °C for 50 hours and water quenched [13]

- γ'' phase present in Tetragonal Body Centered (TBC), Ni_3Nb. The method to observe both phases was introduced by Paulonis et al. [9]. By observing the zone matrix on the axis [001], the orientation shows lattice diffraction patterns, which can be then identified (Figure II. 5). The γ' and the γ'' phases are dispatched homogeneously inside the grains and assure the hardening of the alloy [14]. They are also allowing a control of the grain size expansion by slowing the displacement of the grain joints [15].

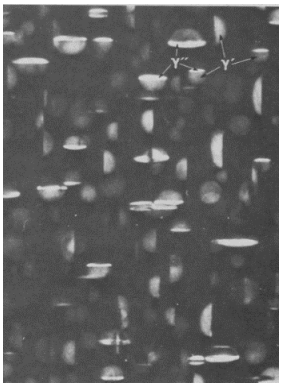

Figure II. 5 Dark field TEM image showing γ'' and γ' phases, obtained on a forged Inconel 718 sample, thermally treated at 700 °C for 524 hours [16]

- δ phase, Simple Orthorhombic structure, Ni_3Nb.The δ precipitates have a plate morphology (Figure II. 6). They appear at the grain boundaries at low temperatures and in an intragranular manner

at high temperatures. Even if they have an effect on the stress rupture ductility, they are formed from the degradation of the γ'' phase. Thus it is necessary to limit that phase in order to avoid a degradation of the hardness of the material.

Figure II. 6 OM of a δ phase developed in a forged Inconel 718 sample after thermal treatment at 870 °C during 50 hours.

The last two elements that can be observed in an Inconel 718 sample are the presence of carbides and Laves (Figure II. 7). The titanium and aluminum elements are extremely sensitive to carbon and is forming carbides with a MC,M_6C, $M_{23}C_6$ phase, all of them having a Cubic structure. The presence of carbides has a detrimental effect on the mechanical properties, both at room and high temperatures. Carbides will consume elements needed in the hardening effect and so will decrease their volume. At high temperatures, during long time periods, carbides undergo transformations, bringing brittle phases. This will perturb the stability of the structure and will have an effect on the creep resistance of the material [17]–[19].

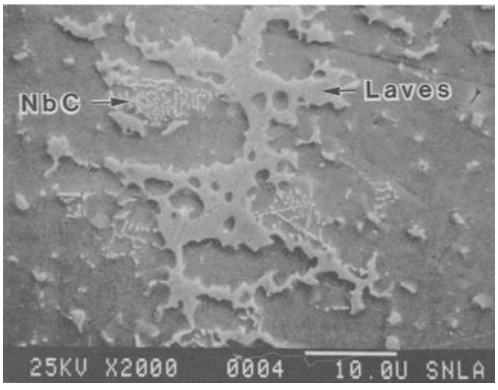

Figure II. 7 SEM image of fusion zone micro constituents in Inconel 718, showing both the NbC and the Laves phases [20]

Laves have an hexagonal structure and often appears during casting, in the presence of a liquid state [21]. They are generally paired with the γ matrix. The effects on the fracture resistance are less

important than with carbides, however they are niobium-rich constituted and facilitate the formation of carbides.

II.1.4 Thermal behaviour of Inconel 718

Knovorosky et al. [20] presented the main reactions related with structural changes due to the temperature on a wrought Inconel 718 sample (Table II. 2). They performed LECO analysis after different thermal treatments on the key components obtained in order to analyse their compositions. They also used a Gleeble simulation equipment in order to obtain the onset of the general grain boundary liquation, hence the lowest melting point of the material constituent.

Laves are formed at a temperature around 1198°C and the temperature when Carbides are obtained is 1252 °C. The solidus temperature is determined to be 1320 °C, but the melting temperature of the material is starting at a much lower temperature, which is 1267 °C. This information is important for the sintering of Inconel 718 and is developed in the next chapters.

Table II. 2 Reactions temperatures obtained on a wrought Inconel 718 sample [20]

	Liquidus	***Solidus***	***γ / Laves***	***γ / NbC***	***Gleeble NST***
Temperature (°C)	1362	1320	1198	1252	1267

In order to optimize the concentration of phases inside Inconel 718, thermal studies were developed since the elaboration of the material. The TTT diagram that was proposed by Brooks et al. [2] presents the temperatures of precipitation of the previously presented phases (Figure II. 8). The solidus temperature of the δ phase is around 1020 °C and can still appear at the grain boundaries until around 800 °C for long thermal cycles. The most important phase, which is the γ'', starts to precipitate around 900 °C until 650 °C. The γ' phase is precipitated between 850 °C and 650 °c, but for cycles longer than 10 hours.

From these information, in order to reduce the quantity of δ phase and to maximize the γ'' phase, the thermal treatment for Inconel 718 commonly applied is a thermal treatment at 980 °C during one hour, in order to concentrate the phases at the grain boundaries, and two steps of 8 hours each at 720 °C and 620 °C [2]. The DTA curves informs us on the transformation phases during a thermal treatment or during cooling. Slama et al presented one obtained after using an Inconel 718 sample which underwent the introduced thermal treatment [6].

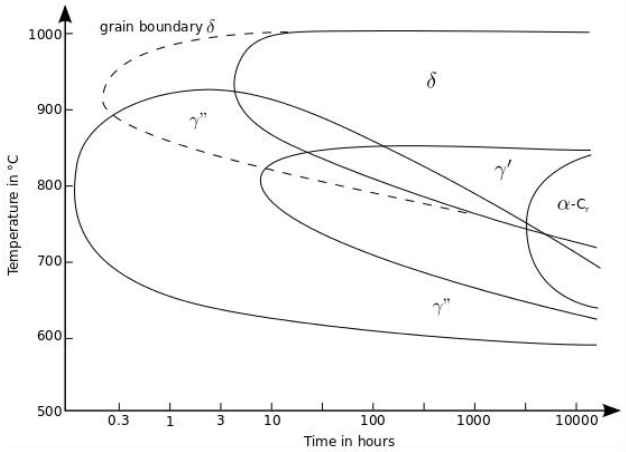

Figure II. 8 TTT diagram of Inconel 718 [2]

A first exothermic peak appears between 400 and 650 °C. After thermal treatment, there is a possibility to continue with the precipitation of the γ' phase, which needs a long time to happen, as seen above. Then, an endothermic peak is observed between 650 °C and 830 °C. This one is attributed to the γ' phase dissolution. It is followed by the same kind of peak between 830°C and 880°C, corresponding to the γ'' phase dissolution. It is finished with a last endothermic peak above 920°C, obtained with the dissolution of the δ phase. While cooling, only one peak is observed, where the precipitation of all three phases happen.

Figure II. 9 DTA curves performed on an aged- wrought Inconel 718 at a heating rate of 5°C/min [6]

II.1.5 Mechanical behaviour of Inconel 718

The tensile properties of Inconel (Table II. 3) are mainly produced by the γ'' hardening phase present in the austenitic matrix. It was evaluated to be in mass fraction at around 9.6 (wt.) % of the material. The size, the homogeneity and the number of γ'' precipitates are the characteristics

responsible for the behaviour of the shearing and the dislocations happening under mechanical stress. It is also important to note that a thermal treatment at 650 °C has low influence on the tensile properties of the material.

Table II. 3 Tensile properties of Inconel 718 forged discs at room temperature (RT) and at a high temperature [2]

	Temperature of the test (°C)	0.2% PS (MPa)	UTS (MPa)	El. (%)
untreated	RT	1170 ± 20	1412 ± 14	19.0 ± 2
	650	965 ± 13	1156 ± 9	25.3 ± 3
1000 hours 650°C	RT	1182 ± 18	1450 ± 15	19.0 ± 1
	650	987 ± 12	1188 ± 10	27.1 ± 2

It was reported that the grain size of Inconel 718 has an important effect on the mechanical properties of the material (Figure II. 10). Thus, it is important to keep the austenitic matrix as fine as possible. It was proven by the maps from Ashby [22] that the creeping speed of Inconel 718 is inversely proportional to the mean grain size of the γ phase [23], [24].

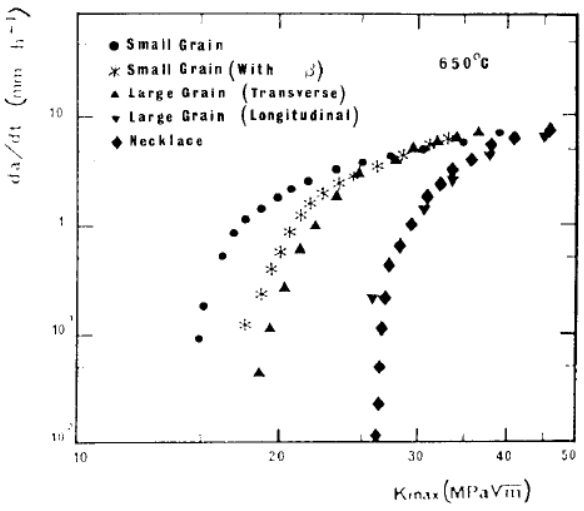

Figure II. 10 Effect of grain size and grain boundary microstructure on the creep crack growth rate at 650 °C [24]

The effects of the thermal treatment increasing the presence of the δ precipitates have also an effect on the hardening properties. As these precipitates are concentrated on the grain boundaries, and are lowering the other two phases, it strongly decreases the properties of the alloy. As seen in Table II. 4, the hardness of the superalloy 718 is also in relationship by the grain growth.

Table II. 4 Grain size and hardness variation of Inconel 718 at different thermal treatments [6]

Thermal treatment during 1 hour (°C)	930	960	990	1020	1050	1080
grain size (µm)	20	21.5	30	40	80	146
HV (200N)	229 ± 4	219 ± 2	200 ± 4	180 ± 3	170 ± 2	161 ± 4

Inconel 718 is mostly used for the good mechanical properties of the material under high temperature conditions. It comes from the good coherence between the γ/γ'' and γ/ γ' phases. Inconel 718 can keep a good mechanical resistance until around 700°C (Figure II. 11). After this, its resistance greatly drops, making it highly interesting for hot forging.

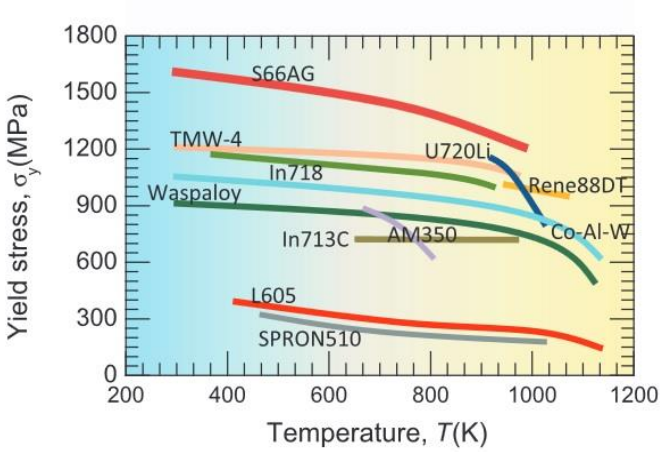

Figure II. 11 Comparison between different materials of the yield stress in function of the temperature [25]

II.2 Introduction to powder metallurgy

Powder Metallurgy (PM) comprises a family of production technologies (Figure II. 12), which process a material in powder form in order to obtain a dense component. The biggest advantage of the powder metallurgy route is the cost effectiveness thanks to a lower energy and material consumption. Instead of applying machining operations that would be applied in conventional manufacture to the material, the powder metallurgy allows complex geometric shapes with close dimensional tolerances. The cost effectiveness is getting more important with the production quantities because of the cost of the equipment and tools. The second advantage of the powder metallurgy is the processing of materials difficult to manufacture such as the hard metals and the carbides [26], [27] or materials with high melting points such as tungsten, molybdenum and tantalum.

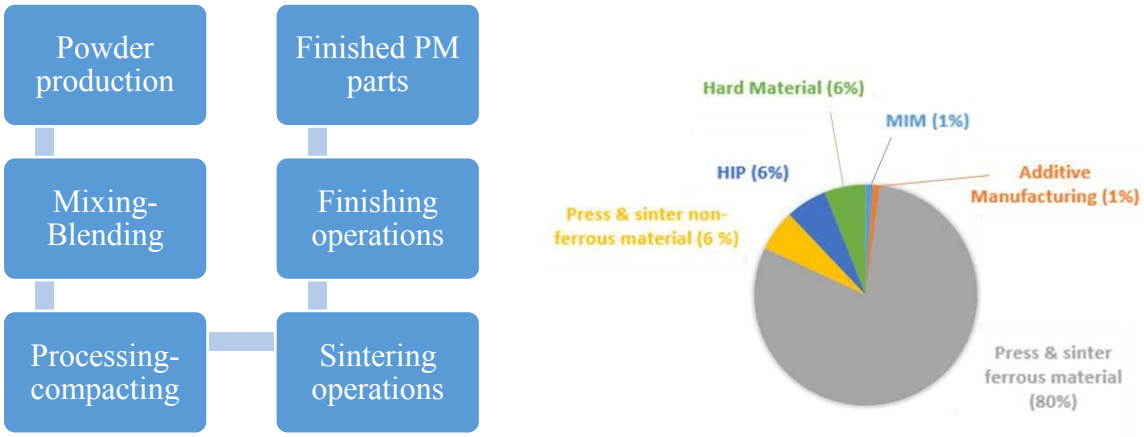

Figure II. 12 Powder metallurgy process route and European parts production by processing methods in 2016 (courtesy of EPMA)

All of the different processes begin with the powder production. The mixing of the powder brings the possibility to introduce alloying elements in a homogeneous form in order to elaborate materials with specific properties such as magnetic materials [28] or superalloys [29]. Before the processing or the compacting of the material, they are blended with a lubricant or a binder, allowing a better flow and a better compressibility of the powder. The shape of the PM part is obtained during an operation of compaction by die pressing or by injection inside a mould giving a green component. They will follow a thermal treatment process. A first one will get rid of the lubricants or the binders and a second one to obtain the densification of the powder via different sintering processes. The sintered PM parts can be heat treated during secondary operations such as the application of a surface treatment.

The powder production provides powder via several different methods such as atomization by using gas water or plasma [30], mechanical milling [31] and chemical conversion process [32]. Each process has distinct advantages and disadvantages in terms of powder morphology, chemical composition, production quantity and production cost.

Depending of the complexity of the geometry, the production quantity and of the material, different processing and sintering operations have been developed. The dominant technology for the forming of products from powder materials, in terms of both parts quantities and numbers of parts produced is the die pressing method. A shoe is filling a die cavity and the powder is compacted by punches from both ends. This method was then developed for more specific conditions such as isostatic pressing, the MIM, or the hot isostatic pressing (HIP). The HIP is a process to densify powders or cast and sintered parts in a furnace at high pressure (100-200 MPa). The gas pressure is used to apply

pressure uniformly in all directions to provide isotropic properties and 100% densification [33]. It provides many benefits and has become a viable and high performance alternative to conventional processes such as forging, casting and machining in many applications. Its positioning is also very complementary to other powder metallurgy (PM) processes such as Metal Injection Moulding (MIM), pressing and sintering.

The additive manufacturing is the new process to obtain components from a powder. At the difference of the other methods using die cavity moulds, the melted powder is directly sprayed on a support, and the component is elaborated layer by layer. It is allowing the development of new shapes and geometries which would be impossible to obtain by machining or moulding such as the hollow structures [34].

II.3 Introduction to powder injection moulding

Powder Injection moulding is a shaping process, which is making possible mass production, by combining thermoplastic polymers injection with powder metallurgy. It is particularly adapted for high production rate of complex shaped products and with costly materials. It also allows low loss of material coming from the process as feedstock can be recycled [35]. Thanks to these advantages, industrials developed the process in order to mass produce their components. The economic and market position of the process in the powder metallurgy will be introduced in the first part of the paragraph.

Table II. 5 Technologies involved in the MIM process

Thermoplastic Injection	Binder rheology and thermal properties
	Powder/binder mixing and extrusion
Transition step	Binder removing by solvents
	Binder removing by thermal treatment
Powder metallurgy	Densification by solid state diffusion or semi-liquid
	Thermal treatments

The MIM process is a mix of the thermoplastic injection and powder metallurgy in order to realize 3D complex shaped mechanical parts with controlled physical properties [36]. They have precise role

in the process. The thermoplastic injection is used to give the component a homothetic shape by replication via the print of a die cavity mould. The powder metallurgy gives mechanical properties to the components. The MIM process combines four successive steps: Feedstock elaboration, injection, debinding and thermal treatment (Table II. 5). They will be presented in the second paragraph, followed by the advantages and the restrictions of the process. The last paragraph presents the materials generally used for feedstock elaboration and their using conditions.

II.3.1 Economic context and market application

Since the first MIM products commercialized in the 80's in the USA, the production has followed a constant increase. The MIM market is essentially dedicated to metallic materials (Figure II. 13). In 2016, 80% of the parts were composed of metal. The materials proposed are composed of different steels, austenitic stainless steel, tungsten alloys, iron nickel alloys, superalloys, titanium or copper. The other 20% of the MIM production is principally the production of carbides, in general for tools elaboration. The Asian market (49%) is the most important, followed by the North American (27%) and the European one (21%) [37]. The main application for the MIM component is following the needs in production quantities such as for firearms and automotive industries.

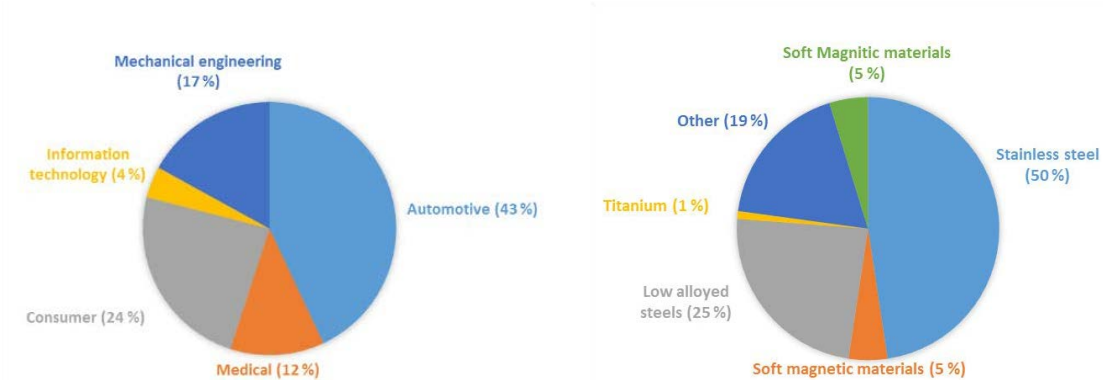

Figure II. 13 Industrial sectors in Europe for MIM process and European MIM sales by material in 2016 (courtesy of EPMA 2017)

The choice of PIM for components production of mechanical components is due to three principal reasons (Figure II. 14). The first one being the precision of the desired geometry, thanks to the thermoplastic injection technology which provides high precision and surface state giving a net-shape component, limiting the machining of the components at the end of the process. The second advantage of PIM is the production rate of the components, reducing the investment cost per part. It is thanks to thermoplastic injection technologies, allowing mass production with a limited number of defects.

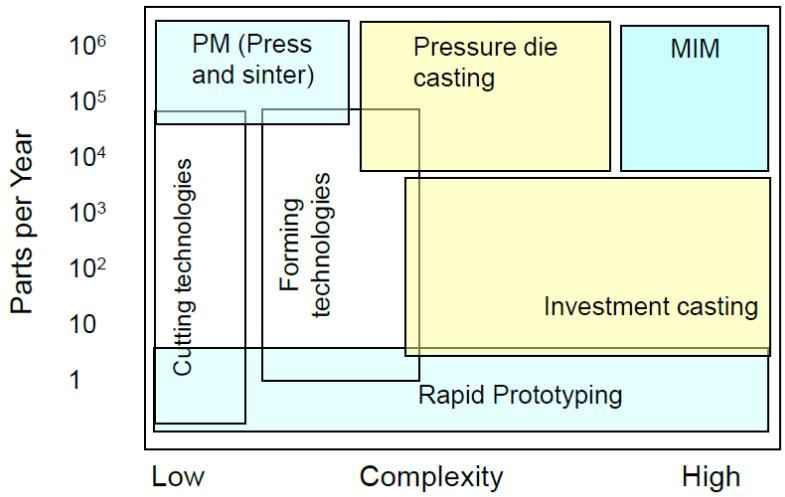

Figure II. 14 Roadmap of economic batch size and shape complexity [38]

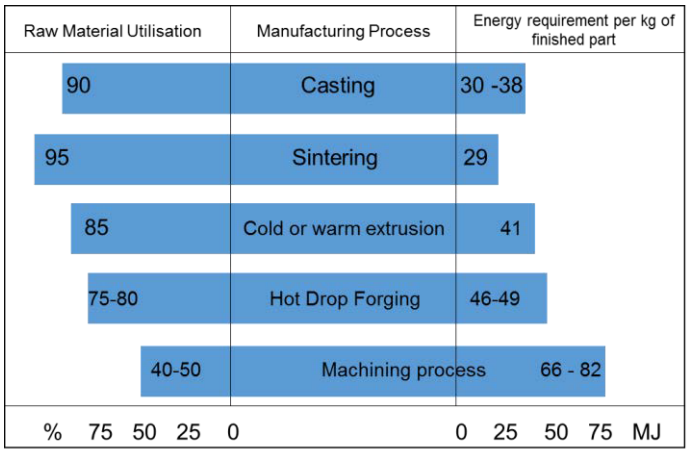

Figure II. 15 Raw material utilisation and energy requirements for different manufacturing techniques [38]

As seen on Figure II. 15, the different manufacturing techniques are compared by the raw material and the energy needed to produce 1 kg of finished parts. The powder sintering is the process with the highest raw material utilisation and the lowest energy requirement at the same time. Some materials, such as carbides and superalloys are difficult to machine [39] and damage the cutting tools faster. Thus, obtaining a component with low raw material consumption is reducing the production costs, and even more for expensive raw materials. The MIM process needs a huge production line in order to cover the costs of all the steps and manipulations needed. It will be more efficient to use this process for mass-producing with a few machining, such as in watch industry [40].

II.3.2 General introduction of the PIM process

This part will introduce the different steps of the MIM process (Figure II. 16). Each step is depending on several factors such as the powder morphology, the choice of a binder or the methods and equipment used for processing an injected component.

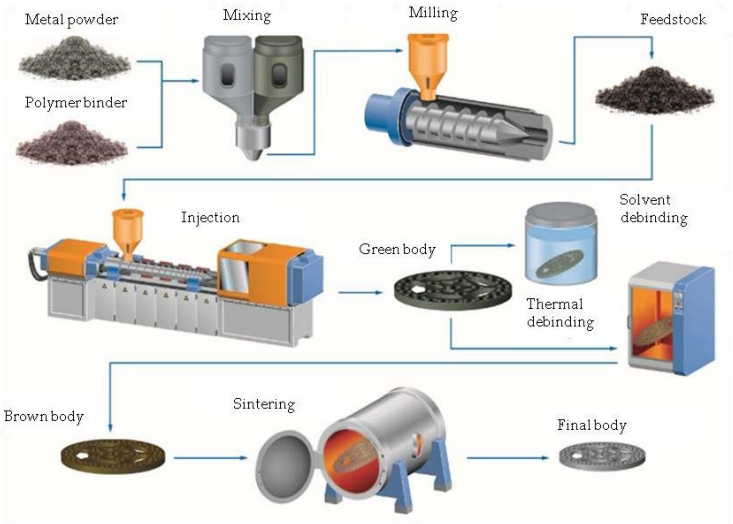

Figure II. 16 Description of the metal powder injection moulding

The first step of the MIM process is the feedstock elaboration. This initial step is the elaboration of a biphasic mix between the metallic powder and the thermoplastic binders. It is obtained by extrusion or, as in our case, by using twin screw mixer. The powder is mixed with thermoplastic binder at a temperature between the highest fusion temperature and the lowest degradation temperature of the binder, and milled after cooling in order to obtain granules usable for injection. The key point of the feedstock elaboration is to obtain a homogeneous mix between the powder and the binder. If not, the final parts may contain cracks or get damaged during the next steps. The proportions of the composed material vary in function of the chosen powder and its morphology. The powder and the binder volume have to be a compromise between a sufficient volume of the binder in order to assure the viscosity of the feedstock and a sufficient powder volume to allow the densification step without defects. In most feedstocks, the best compromise is to use a volume loading rate of 60% of the powder and 40% of the binder [37], [38].

The binder composition has to be adapted to the chosen powder. It has to be fluid enough during the mixing allowing a homogeneous mix with the powder. It also assures the cohesion of the component during the manipulation of the component after injection and resists to the mechanical and chemical solicitation brought along the process without damages [41], [42]. Binders can be

composed of three elements. A first one, named the primary binder, is used for bringing resistance to the injected component. It will create a skeleton structure around the powder and will be removed last in order to keep the shape of the component stable as long as possible. The second, named the secondary binder, has a role of shear thinning. It is used to reduce the viscosity of the feedstock, bringing a good flow during the injection. It will fill the space between the primary binders attached to the powder. The last element that can be introduced in the binder is a dispersive agent, which will assure the segregation of the powder and the cohesion between the primary binder and the powder.

The chosen powder has to verify some morphologic conditions. The first one is the shape of the particles. A spherical shape is the easiest one, for both injection and densification [43]–[45] as shown on Figure II. 17. The size of the particle is also limited. Most the feedstocks are composed of a maximum particle size under 50 µm. Using a bigger size would make the injection harder and the surface state might also be impacted [46]. If the feedstock is used for micro-components or complex shapes, the size of the particle has to be reduced. It can also have an impact on mechanical properties, as it reduces the grain size after densification[47]. One of the recent development in the feedstock elaboration is the use of a bimodal powder composed of a large and one really fine granulometric distribution [48], [49]. This will bring the same geometric advantages as the fine powder at a lower cost.

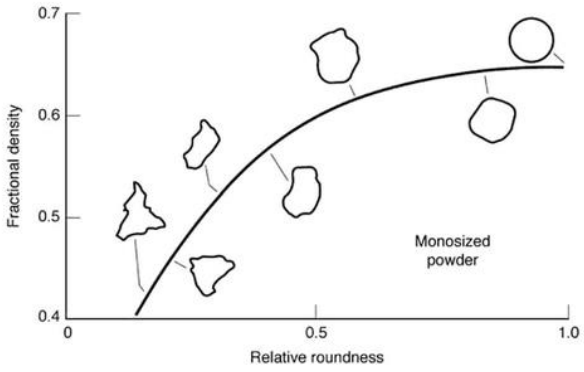

Figure II. 17 Effect of powder shape on the packing density [50]

The component geometry is obtained as it is during the thermoplastic injection. The feedstock is shaped by replication on the print of the cavity of a mould. The feedstock granules are introduced in the feeding hopper of the press, then pass through a temperature regulated sheath. The injection temperature is decided via the rheological analysis of the feedstock, being between the highest fusion temperature and the lowest degradation temperature of the binder. The injection unit is described in Figure II. 18.

It starts by the selection of the volume of injected material. In order to fill the mould cavity properly, the total volume needs to include the cavity of the mould plus the feeding, the sprue, the runners and the channels. The chosen volume is obtained thanks to an endless screw, bringing the feedstock during its rotation. Once the feedstock volume introduction is over, the mould is closed and filled at a determined pressure and speed. It is kept under pressure during the cooling down of the component in order to reach a solid state. It is finally ejected from the mould. The time of the injection process is dependent upon the cooling of the component and the thickness of the geometry [51], [52]. Thus, the temperature of the mould needs to be controlled in order to optimise these parameters.

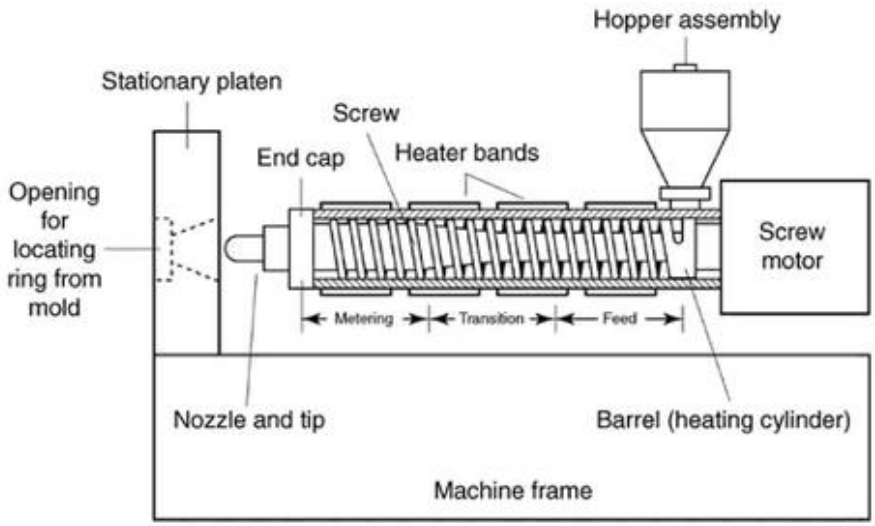

Figure II. 18 Injection unit configuration [53]

Due to thermo-physic of a powder loaded polymer, the specifications of feedstock injection is bringing differences with thermoplastic injection. First, the tools need to be surface treated in order to resist to the abrasion from the powder, in order to improve the lifetime of the equipment. The endless screw geometry has also to be adapted to the feedstock in order to keep its homogeneity. Segregation, jetting or demixing of the feedstock may happen inside the barrel, which can bring defects to the final part with an anisotropy of the densification[54], [55]. Feeding and injection speed need to be slow enough in order to avoid these defects. The filling of the die cavity can also bring defects to the component, such as an incomplete filling of the cavity.

The debinding step consists in the progressive removal of the organic compounds present inside of green components. There are two ways to get rid of them, the first one being the use of a solvent which will dissolve and extract the polymer out of the sample, and the second is the thermal degradation of the polymer.

Solvent debinding is commonly used in order to remove the secondary binder. Thus, the used solvent has to be compatible only with this one. There are two ways for solvent debinding. The first one, developed by BASF, is a catalytic debinding applied to their binder Catamold© [56]. Green parts are introduced inside a chamber with a controlled atmosphere with azote at a temperature between 110 and 140 °C. Acid nitric is injected inside the chamber and the acid atmosphere will dissolve the polymer. The second one is to immerge component into a solvent and thanks to a long diffusion time inside the polymers, dissolve and extract the binder. Thermal debinding eliminates all the residual binder after solvent debinding. It is realized inside an oven with controlled atmosphere if needed. The debinding theory and the different methodology are both more detailed in part II.5, along the description of supercritical debinding. Defects can be created during debinding steps. Most of them come from a problem of evacuation of the residues and gas created during the process. If the gas has no way out of the component, swellings or blisters can appear at the surface. It can also be trapped inside the sample, creating a local pressure point inside the material, leading to a huge decrease of the resistance of the material to creeping. Carbon residues are also found inside of the components, and it is a common problem for the MIM process [57].

The final operation on the component is the complete densification of the powder. The mechanism will be explained in the next part. It is obtained by heating the component at a high enough temperature and maintained for some time. After cooling components possess an annealed microstructure, and without undergoing post thermal treatment, lack the strength of forged components. The quality of sintering depends on the atmosphere, the sintering temperature and the dwell time, the heating rate and finally the cooling rate. These parameters will impact the final density and the microstructure of the component. The time and the complexity of the densification is also dependent on the material. It will be more detailed in part II.4.

II.3.3 Advantages/disadvantages of the PIM process

During the design period of a component, in order to choose if MIM is suitable, there are several conditions to respect in order to maximize the advantages of the process. The first condition being the production quantity and the number of specifications of the component. It is only viable if there are restrictions on the dimensions, locations of complex geometry, surface finish and such. The second condition is if the material is easily sintered. If the sintering temperature is low (under 1000°C), the die casting method may be more effective [58]. Therefore, the MIM process is interesting for materials resisting machining (machining, cutting and grinding), designs with difficult

access for the tools and considerable mass removed (even more when the material is expensive) and smooth surfaces. The development of bi-injection of two different materials or two components [59], [60] now increases the complexity of the components available and reduces the number of operations.

Figure II. 19 Two-component tensile specimens of stainless steel/Stellite6 obtained by MIM [59]

The process issues mostly come from the volume of the components. It becomes delicate for large dimension components, as the injection becomes less homogeneous. The debinding will be much longer, as the core will be more difficult to attain. There are also limitations coming from the shrinkage of the component between the green parts to the dense ones. As said above, the feedstock is composed of only 60% of powder, thus during consolidation, the shrinkage has to be predicted in order to obtain the wanted dimensions.

The last issue is that the MIM process is multi-steps, each with influent parameters. Once the component is damaged, it will not be possible to erase it with the next step (Figure II. 20), and even be amplified [61]. Therefore, it is an obligation to fully understand and optimize each of the parameters steps in order to avoid problems.

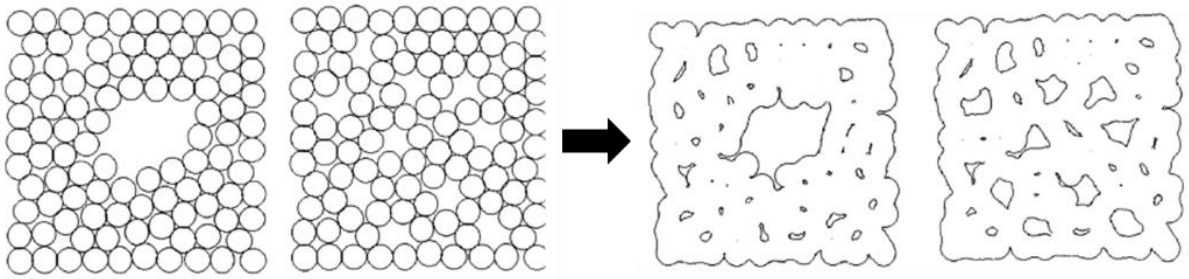

Figure II. 20 Representation of defects produced during injection remaining during sintering [62]

II.3.4 Materials used in feedstocks

The binder system is a transitory element of the feedstock in the melted state and brings rigidity in the solidified state. It does not remain in the final part and has to be removed easily and fast. Since

the beginning of the MIM process, a large variety of binders were developed, yet no miracle binders answering to every conditions of the process was found. Hence, it is a difficult task to select a binder and its components.

Binder systems are formulated as a mixture of organic or inorganic substances with several functions within the system itself. They can be composed of any types of polymers, waxes, oils or other substances like lubricant and dispersant agents. They all have one thing in common, which is the creation of a backbone that gathers particles and retains the shape of the component along all the steps of the process until complete elimination. In order to avoid trapped volatiles inside the component, different compounds with progressive degradation temperatures are selected [63].

Table II. 6 List of binders in literature

Primary binder	Secondary binder	Surfactant	Solvent debinding	Powder	authors
PE	PW	SA	Cyclohexane	316L	Huang at al. [64]
PP	PW	SA	Cyclohexane	Inconel 718	Özgün et al. [65]
EVA	PW	SA	Cyclohexane	Inconel 718	Fareh et al. [66]
PP	PEG	SA	water	Al_2O_3	Moinard et al. [67]
PMMA	PEG	SA	water	Ti-6Al-4V	Chen et al. [68]
CAB	PEG	SA	water	Zr_2O_3, Invar	Hidalgo et al. [69]

Thermoplastic polymers are preferred in PIM as they softened and re-solidified multiple times, allowing recycling of the waste material produced during injection. The most commonly used are polyolefins like polyethylene [43], and different variants of polypropylene [70], polyacetal [71], polymethyl methacrylate [68], ethylene vinyl acetate [72] and polyvinyl butyral [73]. They are blended with waxes or other low molecular weight polymers like polyethylene glycol that act as plasticizers [73]. Some examples of binder compositions are presented in Table II. 6.

II.4 Powder sintering, application to MIM samples

II.4.1 Mechanism of particle sintering

Sintering is a mechanism of bonding particles together. Thanks to the possibility to work in a protective atmosphere, it is possible to work on an extensive number of materials that are sensitive to oxidation such as titanium or aluminium. The mechanism of sintering was studied at the same time of the development of atomic models. When heat is applied to a powder, atoms starts to move randomly, amplified when the temperature is closer to the melting temperature. The atomic motion induces a decrease of the surface energy of the particles. It was put in evidence by measurement of a reduction of the surface area (Figure II. 21).

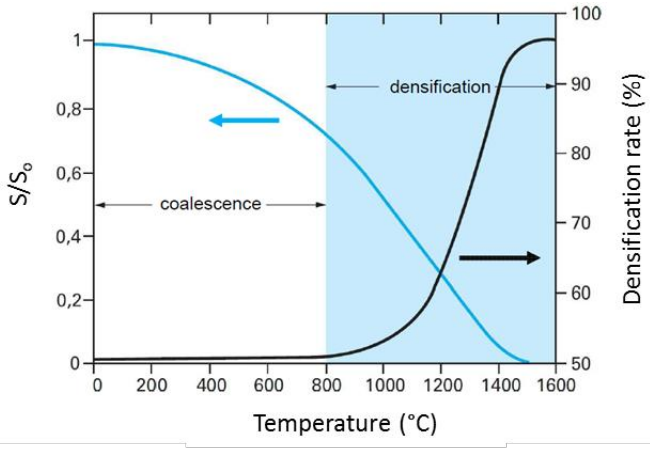

Figure II. 21 Evolution of the specific surface and the densification rate in function of the temperature during solid phase sintering [74]

The consequence is the growing of necks between particles (Figure II. 22). Once a contact has been formed, the atomic motion continues to enlarge the contact surface and subsequently densifies the powder. The speed of that mechanism depends principally on the composition of the powder and its morphology. At the end of the mechanism, the centre of the two particles move together to form a bigger particle. In the case of a powder compact the consequence is that the average grain size enlarges while the number of grains decreases. The grain growth takes place at the grain boundaries, hence the bigger particle presenting bigger boundaries will progressively consume the smaller next to it. If the powder granulometry is not homogeneous, the microstructure may be impacted by a heterogeneous repartition of the grain size.

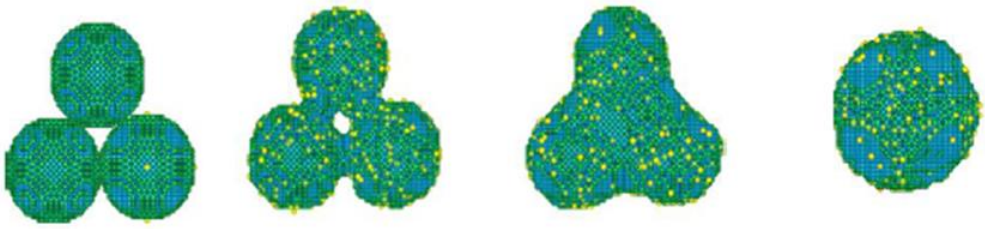

Figure II. 22 Molecular dynamic simulation of three tungsten particles during sintering [75]

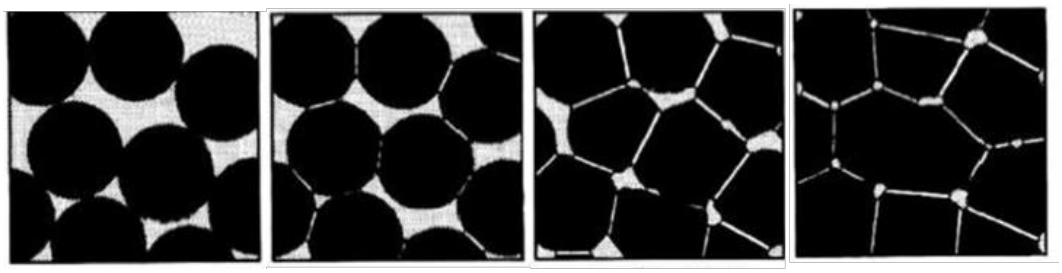

Figure II. 23 Representation of porosity evolution during the sintering [74]

Thus, the sintering stages are followed by a succession of pore and grain morphology changes. It is focused on the growth of the inter-particular bonds until densification of the material. Inside a powder compact, it will be accompanied by the pore network modification (Figure II. 23). The more surface contact the particle will create, the more porosity will equivalently decrease. The pore diameter will shrink and will adapt to the spherical shape of the particles. During sintering, if the atmosphere is performed under high level of vacuum, porosity will be empty and can be completely eliminated. In the case of a controlled atmosphere with gas such as argon or nitrogen, or in the case of MIM with impurity products such as carbon dioxide, gas filled pores may be created. The consequence will be the same as creating a pressure point inside the material and will severely decrease the mechanical performances when solicited. A powder compact can only be accepted as dense only if the pore elimination is complete.

II.4.2 Effect of the morphology of the powder

The changes of microstructures during sintering are influenced by lots of factors which are determined by the chemical and physical properties of the raw powders. If there is a slight difference in volume between the two particles, the smaller particle will start to shrink, and will eventually disappear and a single coarsened spherical particle will remain in the final equilibrium state. As a consequence it was suggested that mono-sized fine powders are preferable in producing dense,

uniform, fine-grained microstructures [76]. The case of bimodal grain size distribution was designed for materials difficult to sinter such as cemented carbides [77].

The granulometry is also having an effect on the sintering conditions. As shown by Figure II. 24, the smaller the particle size, the faster the maximal density can be obtained. It can be explained by a lower energy requirement to obtain the particle movement during sintering when the particles are smaller [78].

Figure II. 24 Effect of the particle size on the fractional density in function of the temperature [79]

Figure II. 25 Values of σ_{Lyp} plotted against the inverse square root of the grain diameter observed after aging treatment of mild steel (left) [81] and evolution of the grain size and of the density during sintering of a Fe-2Ni powder (right)[79]

The grain size of the final microstructure is also influenced by the initial particle size. The Hall Petch relation or grain boundary strengthening is a method to optimize the average crystalline grain size in order to obtain the best mechanical performances. The grain boundaries have an impact on the dislocation movement and how easily they can travel from grain to grain. So by reducing the grain size, the yield strength of the material will be influenced [80]. The choice of an ideal sintering consideration must include the variation of the grain size as the temperature can increase brutally the grain size while the temperature is close to the melting temperature of the material.

II.4.3 Influence of the sintering on MIM samples

As introduced in part II.4.1, sintering implies a reduction of the porosity of the powder compact. A MIM sample, after thermal debinding, is left with the powder particles only, so the porosity level of the component is proportional to the voids left by the polymer. The sintering of MIM sample induces a shrinkage that needs to be followed Figure II. 26. By following the evolution of the shrinkage, it is possible to optimize the thermal treatment conditions such as the heating rate, the dwell time, the maximum temperature and the cooling rate.

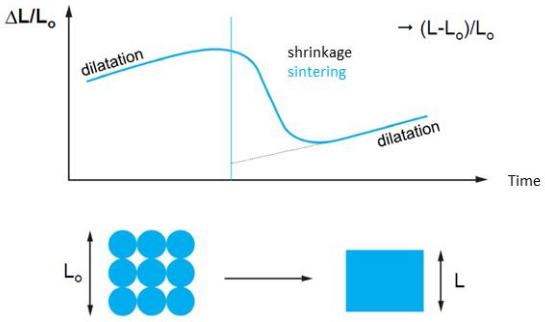

Figure II. 26 Shrinkage evolution during sintering and volume modification before and after sintering [74]

The shrinkage can be a source of defects during sintering if the geometry of the component is not adapted to the process [38]. Hence, the component geometry is limited by three parameters: the maximum cross-sectional area, the maximum length and the maximum thickness.

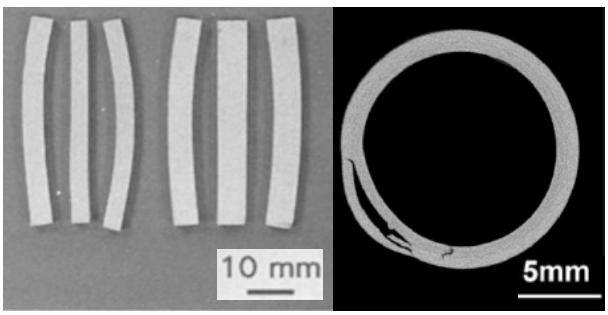

Figure II. 27 Images of MIM samples after sintering showing deformations [82] and cracks [46]

II.4.4 Application to Inconel 718

Since the development of the Inconel 718 superalloy, a few feedstocks have been developed for metal injection (Table II. 7). The first one was developed in 1994 and 1997 by Valencia et al. [1], [83]. After this, a few papers were proposed for sintering Inconel 718 MIM samples. They are

especially focused on the optimal sintering conditions and all of them perform thermal treatment after the initial sintering.

Table II. 7 List of the results during sintering MIM Inconel 718 samples

Powder loading (%)	Powder mean particle size (μm)	Sintering treatment	Furnace atmo-sphere	Maximum shrinkage (%)	Dens-ity (g/cm^3)	Hardn ess	YS 0.2% (MPa)	UTS (MPa)	Elong. (%)	Refer--ences
66	8.5	1275°C 8 hours 1 °C/min	Vacuum	24	8.18	-	972	1194	17.4	Valencia [83]
60	11.9	1290 °C 3 hours 10 °C/min	Vacuum	22	7.99	348	506	667	5.8	Özgun [65]
62	13.1	1275°C 2 hours	Vacuum	x	96.7	370	876	1054	25.4	Youhua [84]
62	2	1150°C 6 hours	Vacuum	x	98	280	x	800	7	
65	10	1220°C 6 hours	Vacuum	x	98.5	280	x	800	15	Miura [85]
65	22	1250°C 6 hours	Vacuum	x	99	330	x	1000	7	

Valencia et al. performed sintering in different atmospheres and heating rates. In a hydrogen atmosphere, they observed the formation of peripheral ring of dense material surrounding a porous material in the middle. It could be explained by hydrogen trapped inside the sample or the formation of water by a reaction between the gas and the oxides present in the sample. Hydrogen is not adapted for sintering Inconel 718. The heating ramp also plays an important role. They found that when the heating ramp is around 10 °C/min, the intermetallic Laves phases are more easily created, resulting in the creation of more porosity during cooling. On one hand, at 1°C/min, there is enough time for the Laves to be dissolved into the matrix, on the other hand, at 15°C/min, they don't have the time to nucleate. The optimal sintering temperature and holding time are trickier to conclude. As Valencia obtained results almost as good as wrought material, they didn't try sintering at higher temperatures.

Özgun et al. [65] performed sintering until 1300°C. At that temperature, as it is closer to the melting temperature of the superalloy (1320°C), they observed deformations of the MIM shape. The main difference that can be observed between 1275 °C and 1290°C is the mechanical properties. The hardness may be similar, the tensile solicitation response is completely different. The sintering selected by Özgun et al. gives a UTS and a YS twice lower than the others.

Youhua et al. [84] explained that the difference may come from melting temperatures of the different components of the superalloy. At 1260°C, the components with the lowest melting points such as the nickel carbides, iron and chromium, compose the liquid phase, resulting in a solid phase mechanism. At 1275°C, the content of the liquid phase is increased, giving a liquid/solid sintering mechanism, which will help reduce porosity. At 1290 °C, the liquid phase content is increased with niobium elements, which is followed by the Ni_3Nb phase precipitation. This liquid phase will reduce the flow of the liquid phase, hence reducing the porosity elimination. To conclude, these three papers performed sintering on MIM Inconel 718 samples followed by HIP treatments or thermal treatments, as explained in part II.1.4., in order to obtain a better density and mechanical performances closer to wrought Inconel 718.

Miura et al. [85] searched for the influence of the starting powder on the sintering conditions. They used three different granulometries with a D_{90} going from 2 µm to 22µm. They found that the lower the powder granulometry was, the lower the sintering temperature was needed in order to obtain full density. The downside of using such fine powder is the need to use water atomization instead of gas atomization. The hardening elements such as titanium and aluminium were much lower with water atomization method. Moreover, the carbon content, 0.05 (wt.) %, on each powder was the same, but the oxygen content was higher with water atomized powders (0.60 (wt.) % instead of 0.046 (wt.) %). That difference in chemical compositions explains the lower mechanical performances of the material after sintering. Completing the sintering conditions, the use of a fine gas atomized powder should be preferably used.

II.5 Debinding methods of MIM feedstocks

One of the most critical steps in PIM process is debinding, which consumes a major part of the processing time. Failure of the powder compact often results if the process is too fast. In order to avoid this, debinding is in general performed in multiple steps in order to remove progressively one at a time the polymers composing the binder. The two methods used are the solvent or catalytic debinding, which will eliminate the polymers acting as plasticizer and the thermal debinding, which will degrade the backbone polymer, right before sintering. The supercritical fluid extraction is a recent method that was researched in order to replace the solvent debinding.

II.5.1 Solvent debinding

Solvent debinding is performed by immerging the MIM components into a fluid at low temperature, which will react with the binder. The liquid will diffuse inside the binder and start a dissolution reaction. It may be accelerated by rising the solvent temperature. Some technics are to be developed in order to improve debinding rates, such as ultrasound waves, but accelerating the debinding has a double-edge effect, as it can also increase the chance of damaging the component.

The evolution of debinding is described in Figure II. 28. The progressive dissolution of the polymer creates percolation ways between the particles, which will be important for the thermal debinding. At the end of the solvent debinding, the component is supported only by the primary binder and becomes more fragile to manipulation.

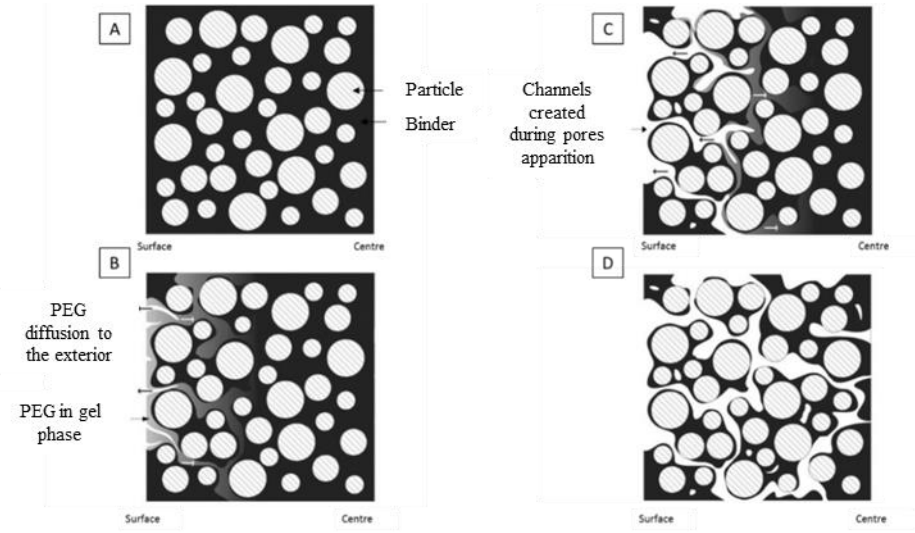

Figure II. 28 Description of the solvent debinding in the case of PEG elimination by water. A: component after moulding injection. B: Start of the progressive diffusion of water inside the binder C: Progressive elimination of the PEG and apparition of porosity inside the component. D: Final state after complete solvent debinding with primary binder back-bone around the particles and porosity channels created through the component [86]

The solvent used depends on the characteristics of the binder, but one of the most efficient is the cyclohexane [87]. As it is a product dangerous for the environment, ethanol and water are getting used more often [68], [88].

In the case of our project, which the main concern is the reduction of the environment impact of the MIM process, the use of water as a solvent was selected avoiding using organic solvent. The compensation is a much longer time of debinding. Depending of the thickness of the component and of the composition of the feedstock, water debinding time generally is at least taking one day. Even

with that amount time, it is also frequent that debinding is incomplete [89], which could bring complications during thermal debinding.

II.5.2 Supercritical debinding

The supercritical state of a fluid can be reached at a certain temperature and pressure cold triple point (Figure II. 29). Above the critical point, there is no physical distinction between the liquid and gaseous states, possessing both advantages of the two states. It possesses the density of a liquid and the viscosity of a gas at the same time. This particular state leads to a high diffusivity, making it more efficient than a liquid. To sum up, the supercritical fluid will penetrate the porous body like a gas and dissolve the binder like a liquid. Moreover, they show high compatibility with non-polar organic materials and low molecular weight materials. This selective behaviour plays in favour of the step-by-step MIM binder debinding.

Research was concentrated on carbon dioxide (CO_2). The conditions for obtaining the supercritical state of the CO2 are rather easy to reach, which are at 304.1 °K and 73.8 bars. It is also easy to change the temperature and pressure conditions to optimize the diffusion (Figure II. 29). Because the solvation capability in a solvent is closely related to the density of the solvent, a supercritical fluid that has a similar density level to liquid represents a high solubility similar to a liquid solvent. Thanks to this, it is also much easier to penetrate inside smaller porosities and faster to reach the centre of the binder matrix.

The debinding rate will be dependent on the temperature and pressure conditions during the experiments. Chartier et al. [90] have shown that the closer to the melting temperature of the polymers, the easier is the extraction of the polymers as they are closer to a liquid state. There is also a high probability that the melting temperature of the polymers will be modified by the supercritical fluid [91].

Most of the work was conducted on wax based feedstocks and ceramic materials. They obtained quite good results with each time a complete removal of the wax in a fast time [92], [93]. They also observed that, even if the temperature was quite high for the debinding of wax, there were no deformations occurring during the supercritical fluid debinding process with few dimensional variations.

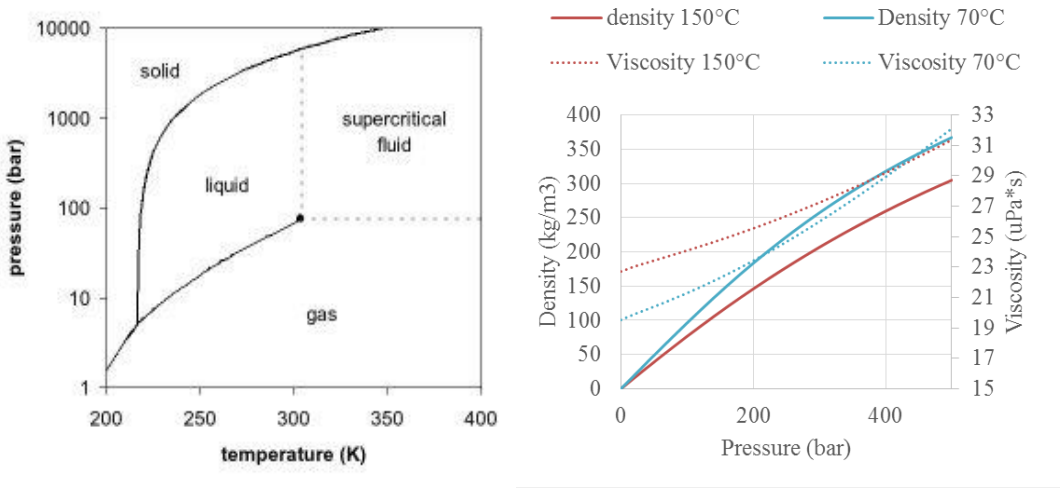

Figure II. 29 Phase diagram of the carbon dioxide [93]and evolution of Carbon dioxide properties in function of the pressure [94]

Yannig et al. [95] even show that solvent debinding was more damaging for the processing of titanium dental implants (Figure II. 30). They also performed carbon and oxygen analysis on pre-sintered samples. The supercritical debinding method did not affect the residual content of these two common contaminants in the MIM process.

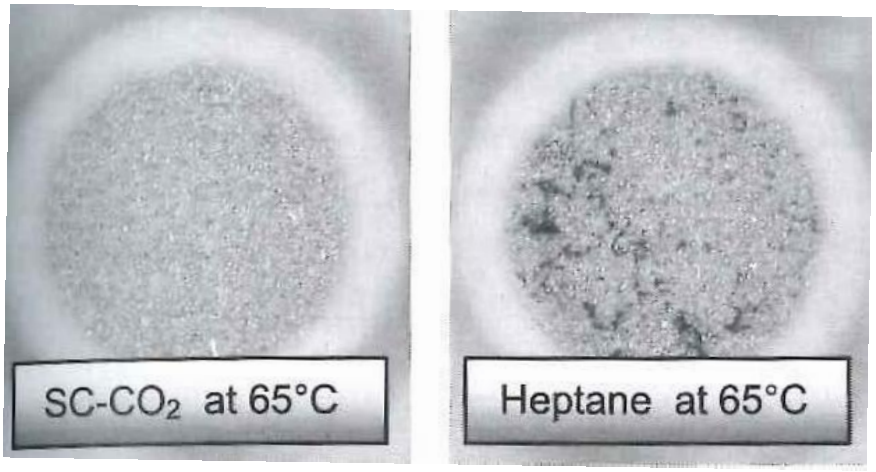

Figure II. 30 Defects observed on MIM samples after wax debinding with supercritical CO_2 and heptane [95]

II.5.3 Thermal debinding

Thermal debinding is a common methodology for the final removal of residual polymer from a PIM compact prior to sintering. During debinding, the polymer is heated thermally, melted into liquid, and decomposed into steam. The overall removal of residual polymer is an intricate combination of evaporation, liquid and gas migration, pyrolysis of polymer, and heat transfer in porous media [96].

It can be used in the same oven as the one for densification in order to optimize temperature cycles and avoid oxidation during the transfer of components.

The thermal treatment consists in realising different dwelling at the degradation temperatures of each binders present inside the sample. At these temperatures, polymers are degraded and vaporised. Hence, the heating rate needs to be slow, as the component's mechanical resistance will only depend on the powder structure. If debinding is too fast, it may disturb its stability. If it is too fast, it can also create overpressure inside the sample [97].

For multi-component binders obtaining optimal thermal cycles is a difficult task (Figure II. 31). It is necessary to perform an investigation of the binder decomposition kinetics in order to identify points of rapid weight loss. They can be obtained by performing thermogravimetric analysis (TGA) on the different polymers composing the binder and on the binder mixed, in case there are chemical interactions during mixing, which could affect the final thermal properties [98]. From these data, it is also now possible to determine master debinding curves and simulate the thermal debinding in order to obtain the best condition for debinding [99].

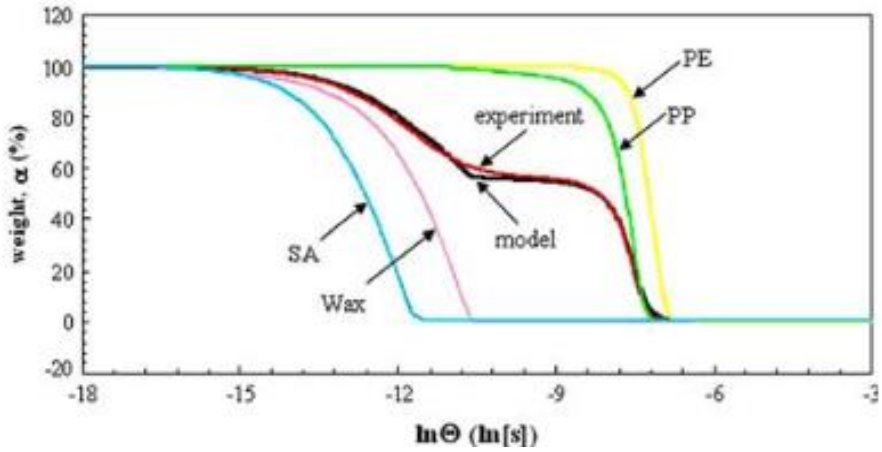

Figure II. 31 Decomposition curves of a wax-PP-PE based feedstock and of each of its elements [99]

The environment of the debinding is also important. Debinding in a wicking environment was developed [100]. The sample is debinded on a porous material, which will absorb by capillary effect the residual polymer extracted during the process. The wicking agent can be a porous plate or a powder disposed around the sample. The result is a homogenization of the polymer extraction and a cleaner surface, and can also prevent cracks or deformation [101].

II.6 Unconventional sintering methods

The introduction of the sintering process and the mechanisms and results of the process were performed with a method that can be named “conventional”, by heating the sample by effect of thermal conduction between the sintering atmosphere and the component, with low heating rate and without physical interactions on the samples. This paragraph will introduce different ways to bring the energy needed to obtain a fully dense material. The Field Assisted Hot Pressing (FAHP) is close to the HIP method, the difference being the way to rise the temperature of the sample. When the heat is brought conventionally in the case of the HIP method, the FAHP method is heating the sample by electrical conductivity. The other method, the microwave sintering, was first developed on ceramics, as the fully dense metals were reflecting them. However it was recently proved that if it was in a powder compact state, metallic materials were able to absorb them until reaching the sintering temperature.

II.6.1 Field Assisted Hot Pressing

FAHP is a method similar to the HIP sintering, the difference being the sintering mechanism. It was developed thanks to the idea of using the plasma on electric discharge for sintering ceramics and metals, leading to the development of a machine and a pattern of Inoue et al. [102], [103]. This allowed the development of different ways of sintering using electric current such as Spark Plasma Sintering (SPS) [104], [105], Flash sintering [106], [107], or Plasma sintering [108].

There are five expected merits of this method: generation of spark plasma, the effect of the electric field and of the electric current in the conductor, the impact of the spark plasma and the rapid heating and cooling. The mean mechanism is the generation of heat via Joule effect, produced by the electric current going through the particle of the powder (

Figure II. 32). This is the case if the powder is conductive, if not, the heat is generated by the heating of the graphite die and will be less effective.

From this and the development of the technology, it is possible to obtain new materials, especially with hard sintering materials such as carbides, borides or nitrides. That technique gives interesting results for tungsten based alloys. It is shown that the application of the electric current, with a 50 MPa of pressure on a milled activated powder, lowers the sintering temperature of almost 1000°C [109]. It is also used for the development of multi-layered components, thanks to the fast sintering, which

will help to limit the diffusion of the materials at the interfacial zones [110]. At the moment, there are no research published on the sintering of Inconel 718 via FAHP sintering.

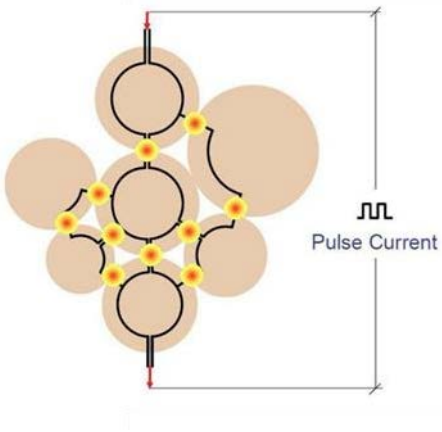

Figure II. 32 Energy dissipation in the microscopic scale [111]

II.6.2 Microwave sintering

Microwaves (MW) were first developed for communication, then the process of heating materials was established in the 1950's. Due to a high compatibility with dielectric materials, water being the perfect example, the advantages of MW heating were implemented in food industries or cleaning thermal treatment for nuclear or petrol industries. The MW heating gained a lot of popularity for processing ceramics powders. Intensive research works have been developed in MW processing of ceramics as they inculcate improved properties [112]–[114].

MW are electromagnetic waves which consist of two fields, an electric one and a magnetic one, and they are orthogonal to each other with wave-lengths ranging from 1 to 1000 mm. MW are wave energy that are converted into heat energy depending upon the type of interaction with the target materials. The processing of a material using MW depends on its dielectric and magnetic properties as the electric field and magnetic field components interact with the material during irradiation.

MW heating occurs internally and unlike conventional heating, the heating rates are not limited by heat transfer from external heat sources (Figure II. 33). Another important feature of the MW heating is the heating direction compared to the conventional heating. Conventional heating occurs via heat flow from external heat sources and heating front propagates from the surface to core via conduction or convection, meaning that the surface of the sample remains at a higher temperature than the core

during conventional heating. In contrast, the MW heating occurs from the core as the MW penetrates and generates heat inside the sample.

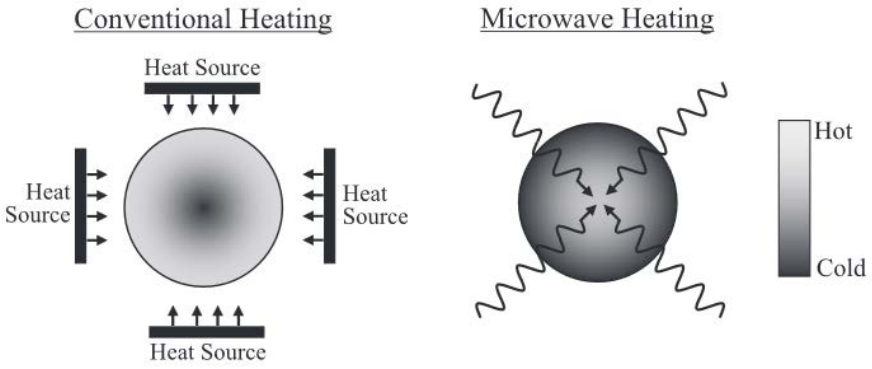

Figure II. 33 Conventional and MW induced heating patterns [115]

The MW coupling with a material inside an applicator is governed by Maxwell's equations [116]. These equations ensure variation of the electric and the magnetic field with time by updating material properties which are responsible for energy absorption. In the case of metal materials, the compatibility with the MW is calculated with a parameter called "Skin Depth" Ds, defined as:

$$D_S = \frac{1}{\sqrt{(\pi f \mu \sigma)}} = 0.029(\rho \lambda_0)^{0.5}$$

In which σ is the electrical conductivity (S m^{-1}), ρ is electrical resistivity (Ωm), λ_0 is the MW wavelength in air (m), f is the MW frequency and μ is the incident wavelength (m). It informs us that the power absorbed during MW irradiation depends on the electromagnetic characteristics, but also on the volume and more precisely the thickness of the target material. Moreover, when the temperature of the material increases, all the material properties get updated influencing the power absorbed (Figure II. 34).

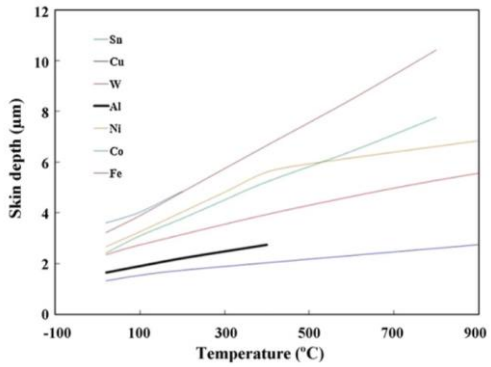

Figure II. 34 Evolution of the Skin depth in function of the temperature for different metals [117]

The heating mechanisms are typically active while MW processing magnetic materials such as iron, nickel, and cobalt. These materials are affected by an electric field and a magnetic field at the same time. The electric field imparts motion to free electrons, whereas the magnetic field affects the electron spin, the domains wall and the orientation of domains [118].

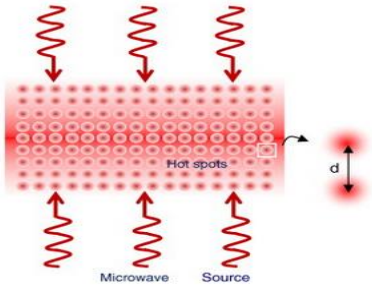

Figure II. 35 Dissipation of the energy brought by the microwaves by hotspots [120]

The movement of the particles will create an energy, transformed into heating in a homogeneous repartition of "hot spots" (Figure II. 35). The principal problem of MW sintering is directly linked to the formation of these "hot spots". It is really easy to obtain an inhomogeneous dissipation of energy through the material, generating temperature gradients; which will be enhanced with time [114], [119]. The result is a heterogeneous microstructure with some parts incompletely sintered and some parts getting too much sintered.

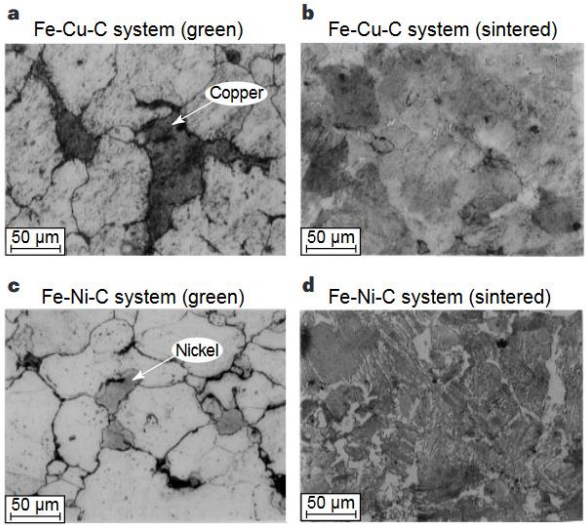

Figure II. 36 Optical micrographs of two sets of 'green' (un-sintered) and microwave sintered powdered–metal parts processed at 1,200 °C for 30 minutes[124]

It was at first considered that metal based materials cannot be processed with MW energy. The reason was that metallic materials reflect MW and electron clouds, leading to plasma arcs, formed at

the sharp edges because of the limited penetration of the MW. It was only reported of the possibility of MW irradiating ceramic bodies doped with a small percentage of metal powder inside, helping to enhance the heating rate [121]. MW sintering was then developed for hybrid heating with matrix metal powders and carbides [122], [123]. It was only recently, in 1999, that Roy et al. [124], obtained fully densified pure metal bodies composed of Fe-Cu-C and of Fe-Ni-C via MW sintering (Figure II. 36). In a short time (30 min) they obtained dense materials that shown higher density, hardness and resistance to rupture.

Finally, MW sintering can be done with different kinds of set-up. The three main ways are presented in Figure II. 37. The direct heating technique is used to heat materials which can be directly exposed to MW. In direct heating, MW easily couple with materials with heat generation inside the processed material. The selective heating technique is a special type of direct heating with certain constraints. A special tooling is used for partial exposure of material to MW. The material to be processed is covered with a masking material where exposure of material to MW is not required. The advantage of this technique is that the desired part of the material can be heated without disturbing the properties of the rest of the volume. In order to overcome the problems associated with direct MW heating, hybrid heating technique was developed. Later, this technique, also called MW hybrid heating, was successfully used for processing of materials which cannot be directly exposed to MW. A special arrangement, consisting in a susceptor (MW absorber) and masking materials, is required in this technique. Heating is completed with the temperature transmission between the susceptor and the non-microwave absorbing material.

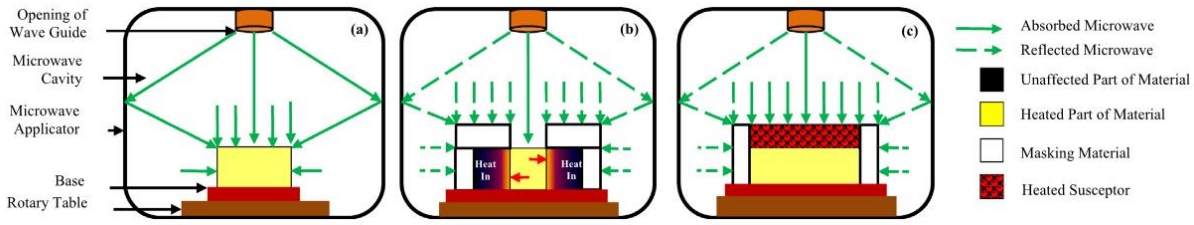

Figure II. 37 Types of microwave heating (a) direct heating, (b) selective heating and (c) hybrid heating [125]

II.7 Partial remarks

This part first introduces the Inconel 718 as a material intensively used for components needed in extreme conditions, both in corrosive and hot atmosphere. In order to resist at these conditions, the thermal treatment of the material plays an important role. It is really sensitive to the temperatures and

the heating rates, as it needs specific sintering conditions in order to maximize the γ'' phase content while avoiding the Laves and δ phases, detrimental to the mechanical performances of the final part. On top of sintering, it is also important to apply a long thermal treatment in order to homogenize the material. In order to have a good idea of the performances of the material, it will be important to perform and optimize the sintering conditions and the thermal treatment.

Secondly, the feedstock also influences the sintering wellbeing. If the mixing of the feedstock and its injection are not done correctly, the green part will not fulfil the conditions for a correct debinding and sintering, impacting the final part and its mechanical performances. So the feedstock parameters, such as the binder chosen and the powder loading rate have to be controlled. Debinding also directly impacts the sintering, as it will rise the carbon content of the component if not done properly, and can also disorganize the powder organization if it is too brutal. It is in general made step by step, by using solvent extraction followed by a thermal degradation of the polymers.

A third part introduced the mechanism of sintering, which will be influenced by the powder morphology, the atmosphere and the way of heating the material. Inconel 718, in the MIM process, was sintered and researched, giving us a range of parameters for the experiments to come, but as the final temperature and dwell time is not clearly set between the results published, it needs to be more investigated.

The last two parts introduced innovative methods for the debinding and the sintering of powder compacts. The supercritical debinding displays great possibilities, as it is possible to obtain a good debinding of a selective choice of polymers, in a short time. Moreover, it is a way that could be considered less impacting on the environment, as it doesn't leave any solvent waste.

The two selected process of the project, the MW and FAHP sintering show improvement of the material properties in a short time by introducing new microstructures. They both have to be done in special conditions, such as the application of pressure or the use of a susceptor, thus implying an adaptation to the MIM process.

REFERENCES

[1] J. J. Valencia, « Sintering effect on the microstructure and mechanical properties of alloy 718 processed by powder injection molding », Miner. Met. Mater. Soc., vol. superalloys 718,625,706 and various derivatives, 1997.

[2] J. W. Brooks et P. J. Bridges, « Metallurgical Stability of Inconel Alloy 718 in S. Reichman et al. (Eds.), Superalloys 1988, TMS, Warrendale, PA », p. 33‑42, 1988.

[3] J. Kolts, « Alloy 718 for the oil and gas industry », Superalloy 718–Metallurgy Appl., p. 739, 1989.

[4] h. R. Copson et w. E. Berry, « qualification of inconel for nuclear power plant applications », corrosion, vol. 16, nº 2, p. 79t‑85t, février 1960.

[5] H. Post, « SpaceX Launches 3D-Printed Part to Space, Creates Printed Engine Chamber », SpaceX,http://www.spacex.com/news/2014/07/31/spacex-launches-3d-printed-part-space-creates-printed-engine-chamber-crewed.

[6] C. Slama et G. Cizeron, « Étude du comportement structural de l'alliage NC 19 Fe Nb (Inconel 718) », J. Phys. III, vol. 7, nº 3, p. 24, 1997.

[7] H. Jianhong, « Y'' Precipitate in Inconel 718 », J.Mater.sci.Technol., vol. 10, p. 293‑303, 1994.

[8] S. Chen, M. Zhao, et L. Rong, « Role of γ′ characteristic on the hydrogen embrittlement susceptibility of Fe–Ni–Cr alloys », Corros. Sci., vol. 101, p. 75‑83, décembre 2015.

[9] D. F. Paulonis, J. M. OBLAK, et D. S. Duvall, « PRECIPITATION IN NICKEL-BASE ALLOY 718 », Trans ASM, vol. 62, p. 611, 1969.

[10] M. J. Cieslak, G. A. Knorovsky, T. J. Headley, et A. D. Romig Jr, « The solidification metallurgy of alloy 718 and other Nb-containing superalloys », Superalloy, vol. 718, p. 59–68, 1989.

[11] N. B. Dahotre, M. H. McCay, T. D. McCay, C. R. Hubbard, W. D. Porter, et O. B. Cavin, « Effect of grain structure on phase transformation events in the inconel 718 », Scr. Metall. Mater., vol. 28, nº 11, p. 1359‑1364, juin 1993.

[12] M. Sundararaman, P. Mukhopadhyay, et S. Banerjee, « Precipitation of the δ-Ni3Nb phase in two nickel base superalloys », Metall. Trans. A, vol. 19, nº 3, p. 453–465, 1988.

[13] A. Oradei-Basile et J. F. Radavich, « A current TTT diagram for wrought alloy 718 », Superalloys, vol. 718, nº 625, p. 325–335, 1991.

[14] J. M. Oblak, D. F. Paulonis, et D. S. Duvall, « Coherency strengthening in Ni base alloys hardened by DO22 γ′ precipitates », Metall. Trans., vol. 5, nº 1, p. 143, 1974.

[15] H. Feldstein et O. Mendoza, « Analysis and Elimination of Time Dependent Notch Sensitivity in Alloy 718 », Superalloys 718-Metall. Appl., p. 655‑671, 1989.

[16] R. Cozar et A. Pineau, « Morphology of y' and y" precipitates and thermal stability of inconel 718 type alloys », Metall. Trans., vol. 4, nº 1, p. 47‑59, janv. 1973.

[17] F. T. Furillo, J. M. Davidson, J. K. Tien, et L. A. Jackman, « The effects of grain boundary carbides on the creep and back stress of a nickel-base superalloy », Mater. Sci. Eng., vol. 39, nº 2, p. 267‑273, août 1979.

[18] G. YANG, Y. XU, L. JIANG, et S. LIANG, « High temperature tensile properties and fracture behavior of cast nickel-base K445 superalloy », Prog. Nat. Sci. Mater. Int., vol. 21, nº 5, p. 418‑425, oct. 2011.

[19] R. C. Reed et al., « The Effect of Carbide Morphologies on Elevated Temperature Tensile and Fatigue Behavior of a Modified Single Crystal Ni-Base Superalloy », Superralloys Miner. Met. Mater. Soc., p. 489‑497, 2008.

[20] G. A. Knorovsky, M. J. Cieslak, T. J. Headley, A. D. Romig, et W. F. Hammetter, « Inconel 718: a solidification diagram », Metall. Trans. A, vol. 20, nº 10, p. 2149–2158, 1989.
[21] S. T. Wlodek et R. D. Field, « "Freckles" in Cast and Wrought Products », Superalloys 718625706 Var. Deriv.-TMS, p. 167‑176, 1994.
[22] M. F. Ashby et H. J. Frost, Deformation-Mechanism Maps, The Plasticity and Creep of Metals and Ceramics, PErgamon Press. 1982.
[23] M. Chaturvedi et Y. Han, « Creep deformation of Alloy 718 », Superalloys, vol. 718, p. 489–498, 1989.
[24] E. Andrieu, R. Cozar, et A. Pineau, « Effect of environment and microstructure on the high temperature behavior of Alloy 718 », Superalloys 718 625 Var. Deriv., p. 241–256, 1989.
[25] H. Bian et al., « Regulating the coarsening of the γ′ phase in superalloys », NPG Asia Mater., vol. 7, nº 8, p. e212, août 2015.
[26] G. S. Kadam et R. S. Pawade, « Surface integrity and sustainability assessment in high-speed machining of Inconel 718 – An eco-friendly green approach », J. Clean. Prod., vol. 147, p. 273‑283, mars 2017.
[27] S. Olovsjö et L. Nyborg, « Influence of microstructure on wear behaviour of uncoated WC tools in turning of Alloy 718 and Waspaloy », Wear, vol. 282, nº Supplement C, p. 12‑21, avr. 2012.
[28] J. Lanzarini et al., « Thermoplastic filled with magnetocaloric powder », Mater. Des., vol. 87, nº Supplement C, p. 1022‑1029, déc. 2015.
[29] M. Cartón-Cordero, B. Srinivasarao, M. Campos, A. García-Junceda, et J. M. Torralba, « On the role of processing parameters in sintered new Co-based (W,Al) alloys », J. Alloys Compd., vol. 674, nº Supplement C, p. 406‑412, juill. 2016.
[30] D. Whittaker, « Atomising Systems Ltd: Making the equipment that makes the powder for over 20 years », Powder Metall. Rev., vol. 3, nº 4, p. 39‑43, Winter 2014.
[31] T. P. Yadav, R. M. Yadav, D. P. Singh, T. P. Yadav, R. M. Yadav, et D. P. Singh, « Mechanical Milling: a Top Down Approach for the Synthesis of Nanomaterials and Nanocomposites », Nanosci. Nanotechnol., vol. 2, nº 3, p. 22‑48, 2012.
[32] A. Morrison et al., « Mechanism of Electrochemical Dissolution of Nickel Grown by Carbonyl Method », Electrochimica Acta, vol. 248, nº Supplement C, p. 112‑122, sept. 2017.
[33] H. V. Atkinson et S. Davies, « Fundamental aspects of hot isostatic pressing: an overview », Metall. Mater. Trans. A, vol. 31, nº 12, p. 2981–3000, 2000.
[34] D. Cooper, J. Thornby, N. Blundell, R. Henrys, M. A. Williams, et G. Gibbons, « Design and manufacture of high performance hollow engine valves by Additive Layer Manufacturing », Mater. Des., vol. 69, nº Supplement C, p. 44‑55, mars 2015.
[35] F. M. Barreiros et M.-T. Vieira, « Powder Injection Moulding to Recover Slate Wastes », Key Eng. Mater. - KEY ENG MAT, vol. 230‑232, p. 247‑250, janv. 2002.
[36] R. German, Sintering Theory and Practice, Wiley J. & Sons. 1996.
[37] R. M. German, « 1 - Metal powder injection molding (MIM): key trends and markets », in Handbook of Metal Injection Molding, D. F. Heaney, Éd. Woodhead Publishing, 2012, p. 1‑25.
[38] EPMA summer school 2017, Dr Marco Actis Grande, Introduction to PM, course notes.
[39] F. Jafarian, M. Imaz Ciaran, D. Umbrello, P. J. Arrazola, L. Filice, et H. Amirabadi, « Finite element simulation of machining Inconel 718 alloy including microstructure changes », Int. J. Mech. Sci., vol. 88, p. 110‑121, nov. 2014.
[40] Inovar Communications Ltd, « PIM International », vol. Vol-10, nº No-4, déc-2016.
[41] R. K. Enneti, V. P. Onbattuvelli, et S. V. Atre, « 4 - Powder binder formulation and compound manufacture in metal injection molding (MIM) A2 - Heaney, Donald F. », in Handbook of Metal Injection Molding, Woodhead Publishing, 2012, p. 64‑92.

[42] C. Quinard, J. Song, T. Barriere, et J. C. Gelin, « Elaboration of PIM feedstocks with 316L fine stainless steel powders for the processing of micro-components », Powder Technol., vol. 208, nº 2, p. 383‑389, mars 2011.
[43] J. M. Contreras, A. Jiménez-Morales, et J. M. Torralba, « Fabrication of bronze components by metal injection moulding using powders with different particle characteristics », J. Mater. Process. Technol., vol. 209, nº 15–16, p. 5618‑5625, août 2009.
[44] M. E. Sotomayor, A. Várez, et B. Levenfeld, « Influence of powder particle size distribution on rheological properties of 316 L powder injection moulding feedstocks », Powder Technol., vol. 200, nº 1–2, p. 30‑36, juin 2010.
[45] P. Suri, S. V. Atre, R. M. German, et J. P. de Souza, « Effect of mixing on the rheology and particle characteristics of tungsten-based powder injection molding feedstock », Mater. Sci. Eng. A, vol. 356, nº 1–2, p. 337‑344, sept. 2003.
[46] A. Mannschatz, A. Müller, et T. Moritz, « Influence of powder morphology on properties of ceramic injection moulding feedstocks », J. Eur. Ceram. Soc., vol. 31, nº 14, p. 2551‑2558, nov. 2011.
[47] B. Du, J. Yang, C. Cui, et X. Sun, « Effects of grain size on the high-cycle fatigue behavior of IN792 superalloy », Mater. Des. 1980-2015, vol. 65, p. 57‑64, janv. 2015.
[48] R. M. German, « Prediction of sintered density for bimodal powder mixtures », Metall. Trans. A, vol. 23, nº 5, p. 1455‑1465, mai 1992.
[49] J.-P. Choi, H.-G. Lyu, W.-S. Lee, et J.-S. Lee, « Densification and microstructural development during sintering of powder injection molded Fe micro–nanopowder », Powder Technol., vol. 253, p. 596‑601, février 2014.
[50] D. F. Heaney, « 3 - Powders for metal injection molding (MIM) », in Handbook of Metal Injection Molding, Woodhead Publishing, 2012, p. 50‑63.
[51] J. F. Agassant et P. G. Gennes, La mise en forme des matières plastiques, Technique et Documentation. 1996.
[52] J. F. Pichon et C. Guichou, Injection des matières plastiques. Dunod, 2014.
[53] D. F. Heaney et C. D. Greene, « 6 - Molding of components in metal injection molding (MIM) », in Handbook of Metal Injection Molding, Woodhead Publishing, 2012, p. 109‑133e.
[54] T. Barriere, B. Liu, et J. C. Gelin, « Analyses of powder segregation in MIM », Met. Powder Rep., vol. 57, nº 5, p. 30‑33, mai 2002.
[55] T. Barriere, J. C. Gelin, et B. Liu, « Experimental and numerical investigations on properties and quality of parts produced by MIM », Powder Metall., vol. 44, nº 3, p. 228‑234, mars 2001.
[56] « Catalytic Debinding with Catamold - BASF - Monomers ». http://www.catamold.de/cm/internet/en/content/Microsite/Catamold/Produkt_und_Technologie/Katalytische_Entbinderung. [Consulté le: 22-mars-2017].
[57] G. Herranz, « 12 - Control of carbon content in metal injection molding (MIM) A2 - Heaney, Donald F. », in Handbook of Metal Injection Molding, Woodhead Publishing, 2012, p. 265‑304.
[58] S. K. Kim, H. Cho, H. H. Jo, M. K. Han, S. T. Lim, et T. Hur, « Material Life Cycle Assessment for Diecasting Process », Mater. Sci. Forum, vol. 426‑432, p. 3353‑3358, 2003.
[59] M. Mulser, « Joining during shaping: two-component MIM provides new possibilities », Met. Powder Rep., vol. 71, nº 6, p. 445‑449, nov. 2016.
[60] M. Mulser, G. Veltl, et F. Petzoldt, « Development of magnetic/non-magnetic stainless steel parts produced by two-component metal injection molding », Int. J. Precis. Eng. Manuf., vol. 17, nº 3, p. 347‑353, mars 2016.

[61] K. S. Hwang, « 10 - Common defects in metal injection molding (MIM) A2 - Heaney, Donald F. », in Handbook of Metal Injection Molding, Woodhead Publishing, 2012, p. 235‑253.
[62] K. Mori, M. Ohashi, et K. Osakada, « Simulation of microscopic shrinkage behaviour in sintering of powder compact », Int J Mech Sci, vol. 40, nº 10, p. 989‑999, 1998.
[63] R. K. Enneti, S. J. Park, R. M. German, et S. V. Atre, « Review: Thermal Debinding Process in Particulate Materials Processing », Mater. Manuf. Process., vol. 27, nº 2, p. 103‑118, février 2012.
[64] M.-S. Huang et H.-C. Hsu, « Effect of backbone polymer on properties of 316L stainless steel MIM compact », J. Mater. Process. Technol., vol. 209, nº 15–16, p. 5527‑5535, août 2009.
[65] Ö. Özgün, H. Ö. Gülsoy, R. Yılmaz, et F. Fındık, « Microstructural and mechanical characterization of injection molded 718 superalloy powders », J. Alloys Compd., vol. 576, p. 140‑153, nov. 2013.
[66] F. Fareh, V. Demers, N. R. Demarquette, S. Turenne, et O. Scalzo, « Molding Properties of Inconel 718 Feedstocks Used in Low-Pressure Powder Injection Molding », Adv. Mater. Sci. Eng., vol. 2016, p. e7078045, juill. 2016.
[67] D. Moinard, C. Rigollet, et P. Lourdin, « Powder injection moulding PIM of feedstock based on hydrosoluble binder and submicronic powder to manufacture parts having micro-details », Powder Techonology, nº 208(2), p. 472‑479, 2011.
[68] G. Chen, P. Cao, G. Wen, et N. Edmonds, « Debinding behaviour of a water soluble PEG/PMMA binder for Ti metal injection moulding », Mater. Chem. Phys., vol. 139, nº 2–3, p. 557‑565, mai 2013.
[69] J. Hidalgo Garcia, « Development of binder systems based on CAB for powder injection moulding (PIM) and micro powder injection moulding (µ-PIM) of Zircon and Invar powders », 2014.
[70] X. Kong, T. Barriere, et J. C. Gelin, « Determination of critical and optimal powder loadings for 316L fine stainless steel feedstocks for micro-powder injection molding », J. Mater. Process. Technol., vol. 212, nº 11, p. 2173‑2182, nov. 2012.
[71] G. B. Stringari, B. Zupančič, G. Kubyshkina, B. von Bernstorff, et I. Emri, « Time-dependent properties of bimodal POM — Application in powder injection molding », Powder Technol., vol. 208, nº 3, p. 590‑595, avril 2011.
[72] S. Supriadi, E. R. Baek, C. J. Choi, et B. T. Lee, « Binder system for STS 316 nanopowder feedstocks in micro-metal injection molding », J. Mater. Process. Technol., vol. 187–188, p. 270‑273, juin 2007.
[73] G. Thavanayagam, D. L. Zhang, K. L. Pickering, et S. Raynova, « A Study of Polyvinyl Butyryl Based Binder System in Titanium Based Metal Injection Moulding », Key Eng. Mater., vol. 520, p. 167‑173, 2012.
[74] D. Bernache-Assolant et J.-P. Bonnet, Frittage : aspects physico-chimiques- Partie 1 : frittage en phase solide. 2012.
[75] R. M. German, « Powder Metallurgy Review », vol. 5, nº 3, p. 71‑80, Autumn/fall-2016.
[76] M. F. Yan, R. M. Cannon, H. K. Bowen, et U. Chowdhry, « Effect of grain size distribution on sintered density », Mater. Sci. Eng., vol. 60, nº 3, p. 275–281, 1983.
[77] A. Petersson et J. Ågren, « Sintering shrinkage of WC–Co materials with bimodal grain size distributions », Acta Mater., vol. 53, nº 6, p. 1665‑1671, avr. 2005.
[78] R. Kalyanaraman, S. Yoo, M. S. Krupashnkara, T. S. Sudarshan, et R. J. Dowding, « Synthesis and Consolidati on of Iron Nanopowders », Nanostructured Mater., vol. 10, nº 8, p. 1379‑1392, 1998.

[79] R. German, « Powder Injection Molding of Metals, Ceramics & Carbides », MIM2017, Orlando, FL, 2017.
[80] W. D. Callister, Materials science and engineering: an introduction, 7. ed. New York, NY: Wiley, 2007.
[81] E. O. Hall, « The deformation and ageing of mild steel: II characteristics of the lüders deformation », Proc. Phys. Soc. Sect. B, vol. 64, nº 9, p. 742, 1951.
[82] H. Y. Zhang, S. H. Zhang, M. Cheng, et Z. X. Li, « Deformation characteristics of δ phase in the delta-processed Inconel 718 alloy », Mater. Charact., vol. 61, nº 1, p. 49‑53, janv. 2010.
[83] J. J. Valencia, T. McCabe, K. Hens, J. O. Hansen, et A. Bose, « Microstructure and Mechanical Properties of Inconel 625 and 718 Alloys Processed by Powder Injection Molding », Superalloys 718,625,706 and Various Derivatives, p. 935‑945, 1994.
[84] H. Youhua, L. Yimin, H. Hao, L. Jia, et T. Xiao, « Preparation and Mechanical Properties of Inconel718 Alloy by Metal Injection Molding », Rare Met. Mater. Eng., vol. 39, nº 5, p. 775‑780, mai 2010.
[85] H. Miura, H. Ikeda, T. Iwahashi, et T. Osada, « High Temperature and Fatigue Properties of Injection Moulded Superalloy Compacts », PIM Int., nº 4, p. 68‑70, 2010.
[86] W.-W. Yang, K.-Y. Yang, M.-C. Wang, et M.-H. Hon, « Solvent debinding mechanism for alumina injection molded compacts with water-soluble binders », Ceram. Int., vol. 29, nº 7, p. 745‑756, 2003.
[87] M. T. Zaky, « Effect of solvent debinding variables on the shape maintenance of green molded bodies », J. Mater. Sci., vol. 39, nº 10, p. 3397‑3402, mai 2004.
[88] G. Shibo, Q. Xuanhui, H. Xinbo, Z. Ting, et D. Bohua, « Powder injection molding of Ti–6Al–4V alloy », J. Mater. Process. Technol., vol. 173, nº 3, p. 310‑314, avril 2006.
[89] M. Song et al., « Water-soluble binder with high flexural modulus for powder injection molding », J. Mater. Sci., vol. 40, nº 5, p. 1105–1109, 2005.
[90] T. Chartier, F. Bordet, E. Delhomme, et J. François Baumard, « Extraction of binders from green ceramic bodies by supercritical fluid: influence of the porosity », J. Eur. Ceram. Soc., vol. 22, nº 9–10, p. 1403‑1409, sept. 2002.
[91] J. V. Schnitzler et R. Eggers, « Mass transfer phenomena in polymers during treatment in a supercritical CO2 atmosphere. Proceedings of the 5th meeting on Supercritical Fluids », in INPL Press: Vandoeuvre, 1998, p. 93‑98.
[92] H. S. Kim, J. M. Byun, M. J. Suk, et Y. D. Kim, « Powder Injection Molding of Translucent Alumina using Supercritical Fluid Debinding », J. Korean Powder Metall. Inst., vol. 21, nº 6, p. 407‑414, 2014.
[93] T. Shimizu, Y. Murakoshi, T. Sano, R. Maeda, et S. Sugiyama, « Fabrication of micro-parts by high aspect ratio structuring and metal injection molding using the supercritical debinding method », Microsyst. Technol., vol. 5, nº 2, p. 90‑92.
[94] « Data from NIST Standard Reference Database 69: NIST Chemistry WebBook ». http://webbook.nist.gov/. [Consulté le: 09-janv-2017].
[95] T. Yannig et E. Baril, « Benefits of supercrititical CO2 debinding for titanium powder injection moulding? », World PM Proc., vol. 4, p. 315‑321, 2010.
[96] Y. Shengjie, Y. C. Lam, J. C. Chai, et K. C. Tam, « Simulation of thermal debinding: effects of mass transport on equivalent stress », Comput. Mater. Sci., vol. 30, nº 3–4, p. 496‑503, août 2004.
[97] X. LIU, Y. LI, J. YUE, et F. LUO, « Deformation behavior and strength evolution of MIM compacts during thermal debinding », Trans. Nonferrous Met. Soc. China, vol. 18, nº 2, p. 278‑284, avril 2008.

[98] A. Royer, T. Barriere, et J. C. Gelin, « The degradation of poly(ethylene glycol) in an Inconel 718 feedstock in the metal injection moulding process », Powder Technol., vol. 284, p. 467‑474, nov. 2015.
[99] G. Aggarwal, S.-J. Park, I. Smid, et R. M. German, « Master Decomposition Curve for Binders Used in Powder Injection Molding », Metall. Mater. Trans. A, vol. 38, nº 3, p. 606‑614, avr. 2007.
[100] R. M. German, « Theory of Thermal Debinding », Int. J. Powder Metall., vol. 23, nº 4, p. 237‑245, 1987.
[101] G. Lovro, « Wick debinding - an_effective way of solving problems in the debinding process of powder injection molding », in Some critical isues for injection molding, Jian Wang., 2012, p. 89‑104.
[102] K. Inoue, « US Patent, No. 3 241 956 (1966) ».
[103] K. Inoue, « US Patent, No. 3 250 892 (1966) ».
[104] S. Grasso, Y. Sakka, et G. Maizza, « Electric current activated/assisted sintering: a review of patents 1906–2008 », Sci. Technol. Adv. Mater., vol. 10, nº 5, p. 053001, oct. 2009.
[105] R. Orrù, R. Licheri, A. M. Locci, A. Cincotti, et G. Cao, « Consolidation/synthesis of materials by electric current activated/assisted sintering », Mater. Sci. Eng. R Rep., vol. 63, nº 4‑6, p. 127‑287, févr. 2009.
[106] M. Cologna et R. Raj, « Surface Diffusion-Controlled Neck Growth Kinetics in Early Stage Sintering of Zirconia, with and without Applied DC Electrical Field », J. Am. Ceram. Soc., vol. 94, nº 2, p. 391‑395, février 2011.
[107] L. B. Caliman, E. Bichaud, P. Soudant, D. Gouvea, et M. C. Steil, « A simple flash sintering setup under applied mechanical stress and controlled atmosphere », MethodsX, vol. 2, p. 392‑398, oct. 2015.
[108] D. L. Johnson, « Comment on "Temperature-Gradient-Driven Diffusion in Rapid-Rate Sintering" », J. Am. Ceram. Soc., vol. 73, nº 8, p. 2576‑2578, août 1990.
[109] E. Oda, H. Fujiwara, K. Ameyama, et S. Yamaguchi, « Microstructure and Sinterability of Nano-Crystal Tungsten Powders », J. Jpn. Inst. Met. Mater., vol. 69, nº 11, p. 967‑972, 2005.
[110] A. H. Pakseresht, A. H. Javadi, M. Bahrami, F. Khodabakhshi, et A. Simchi, « Spark plasma sintering of a multilayer thermal barrier coating on Inconel 738 superalloy: Microstructural development and hot corrosion behavior », Ceram. Int., vol. 42, nº 2, Part A, p. 2770‑2779, février 2016.
[111] H. U. Kessel, J. Hennicke, R. Kirchner, et T. Kessel, « Rapid sintering of novel materials by FAST/SPS—Further development to the point of an industrial production process with high cost efficiency », FCT Syst. GmbH, vol. 96528, 2010.
[112] V. Delobelle, J. Croquesel, D. Bouvard, J. M. Chaix, et C. P. Carry, « Microwave sinter forging of alumina powder », Ceram. Int., vol. 41, nº 6, p. 7910‑7915, juillet 2015.
[113] S. Charmond, C. P. Carry, et D. Bouvard, « Densification and microstructure evolution of Y-Tetragonal Zirconia Polycrystal powder during direct and hybrid microwave sintering in a single-mode cavity », J. Eur. Ceram. Soc., vol. 30, nº 6, p. 1211‑1221, avril 2010.
[114] D. Bouvard, S. Charmond, et C. P. Carry, « Multiphysics simulation of microwave sintering in a monomode cavity », in Proc. 12th Seminar "Computer Modeling in Microwave Engineering and Applications", Grenoble, France, 2010, p. 21–26.
[115] M. Bhattacharya et T. Basak, « A review on the susceptor assisted microwave processing of materials », Energy, vol. 97, p. 306‑338, février 2016.
[116] J. M. Hill et M. J. Jennings, « Formulation of model equations for heating by microwave radiation », Appl. Math. Model., vol. 17, nº 7, p. 369‑379, juillet 1993.

[117] C. Padmavathi, A. Upadhyaya, et D. Agrawal, « Effect of microwave and conventional heating on sintering behavior and properties of Al–Mg–Si–Cu alloy », Mater. Chem. Phys., vol. 130, nº 1–2, p. 449‑457, oct. 2011.
[118] M. Sparks, Ferromagnetic-relaxation theory. New York, NY: McGraw-Hill, 1977.
[119] T. Santos, M. A. Valente, J. Monteiro, J. Sousa, et L. C. Costa, « Electromagnetic and thermal history during microwave heating », Appl. Therm. Eng., vol. 31, nº 16, p. 3255‑3261, nov. 2011.
[120] A. Chatterjee, T. Basak, et K. G. Ayappa, « Analysis of microwave sintering of ceramics », AIChE J., vol. 44, nº 10, p. 2302–2311, 1998.
[121] T. Nishitani, « Method for sintering refractories and an apparatus therefor. US patent 4147911 (1979) ».
[122] E. Bescher, S. Urmimala, et J. MacKenzie, « Microwave Processing of Aluminum-Silicon Carbide Cermets », MRS Online Proceeding Libr. Arch. 269.
[123] W. L. E Wong et M. Gupta, « Simultaneously Improving Strength and Ductility of Magnesium using Nano-size SiC Particulates and Microwaves », Adv. Eng. Mater., vol. 8, nº 8, p. 735‑740, août 2006.
[124] R. Roy, D. Agrawal, J. Cheng, et S. Gedevanishvili, « Full sintering of powdered-metal bodies in a microwave field », Nature, vol. 399, nº 6737, p. 668‑670, juin 1999.
[125] R. R. Mishra et A. K. Sharma, « Microwave–material interaction phenomena: Heating mechanisms, challenges and opportunities in material processing », Compos. Part Appl. Sci. Manuf., vol. 81, p. 78‑97, février 2016.

III METHODS AND MATERIALS: RAW MATERIALS AND BULK MATERIAL CHARACTERIZATION METHODOLOGY

This chapter introduces the raw materials used for the elaboration of Inconel 718 MIM components. The goal of this chapter is to present the characterization of the raw materials used in the composition of the feedstocks and the different methods used to characterize the bulk material after the debinding and the sintering steps in order to control the quality of the components produced.

The Inconel 718 powder was commercially purchased at Sandvik Osprey Company with a D_{90} below 32 µm, obtained via gas atomization. A second powder was used for the feedstock elaboration with a flake shape and a finer particle size. The binders were developed and optimized by previous thesis in FEMTO-ST and UC3M [1]–[3]. They are both PEG based binders thanks to the high solubility of the polymer into water. The PEG is also one of the polymer exhibiting compatibility with the supercritical state of the CO_2. All of the raw materials were characterized in order to prepare the mixing of the feedstocks and the processing of the MIM components.

The second parts of the chapter is devoted to the bulk material characterization, right after the injection step until the final thermal treatment step. The MIM process main interest is the repeatability of the component elaboration. Most of the work will concern the effects of the new processing methods on the final component. The control of the dimensions along the general aspect of the component, the density and the hardness are the first parameters measured in order to confirm if the component is valid. The next step is the metallographic and the mechanical analysis of the components. In order to perform these analysis, the microscopy techniques, the nano-identation and the micro-tensile strength tests were selected.

III.1 Raw materials selection

During this work, two Inconel 718 powders were used in order to elaborate MIM components (Table III. 1). The first one is a commercial powder provided by Sandvik Osprey with a D_{90} of 27.4 µm with a spherical morphology, this powder will be referenced as Inconel 718 S. This powder was chosen by the ProPIM industrial members. The second one was a part of the commercial powder ball

milled by Uvr-fia during 13 hours. The idea was to reduce the particle size in order to study the influence of a finer powder on the behaviour of the feedstock during the debinding and the sintering steps. The obtained powder is now in a flake shape instead of its spherical morphology. The supplier measured of d_{90} of 18.1 and also measured a Sauber diameter of 2.89 µm. The received powder was sieved below 12 µm in order to take away most of the larger flakes. It will be referenced as Inconel 718 M.

Table III. 1 Data on the powders provided by the suppliers

Powder	supplier	D_{90} (µm)	specific surface (m^2/g)	ρ ($g.cm^3$)	morphology
Inconel 718 S	Osprey	27.4	N/A	8.25	spherical
Inconel 718 M	Uvr-fia	18.1	0.26	8.12	flake

The properties of the CAB are dependent of the percentage of the side groups, and during the thesis of Javier Hidalgo [1] the CAB381-0.1 shows the most interesting results during the solvent debinding and the rheology of the binder was allowing the injection of components composed with an Invar 36 alloy with a D_{90} of 12 µm. The PP670 KH is used as an element of a binder also developed during a thesis by Dimitri Claudel [4] for different powder particle size and the effect on the rheological behaviour. The PEG 20 K having a high Mn of 20000 was chosen for the binders formulations as the solubility in water, the thermal properties and the viscosity are more interesting for the MIM [5]-[6]. The stearic acid is commonly used as a surfactant in the powder industry and is also used for this important role for the homogeneity of the feedstock into both of the binders [7].

Table III. 2 Data on the polymers provided by the supplier

Polymers	supplier	Mn	ρ ($g.cm^3$)	T_g (°C)	T_m (°C)
CAB 381-0.1	Eastman	20000	1.2	123	155-165
PP 670 KH	Sabic	N/A	0.9	N/A	N/A
PEG 20 K	Fluka	20000	1.22	N/A	60-70
SA	Merck kGaA	N/a	0.84	N/A	68-70

III.2 Powders characterization

III.2.1 Morphology of the powders

The morphology of the powders was checked by using both OM and SEM. They were coated with a resin and polished in order to be able to observe the intern porosity of the particles and to facilitate

the dimension measurement. The SEM analysis was performed on the powder thanks to a conductive carbon tape.

The commercial powder shows a good spherical shape and with no intern porosities of the particles (Figure III. 1). The mean size measured of the particles on the pictures is of 18.75±7.8 µm. It shows a mix between particles with a diameter around 20 µm surrounded by much smaller one with a diameter under 10 µm. The SEM image shows a neat surface, without irregularities. The only comment that can be done on the powder is the presence of small particles agglomerated to bigger one, which is happening often in the case of gas atomization [8]. This phenomenon happens during the projection of the melted particles, which are colluding and are cooling down connected together. Thus the spherical shape becomes less neat as planned.

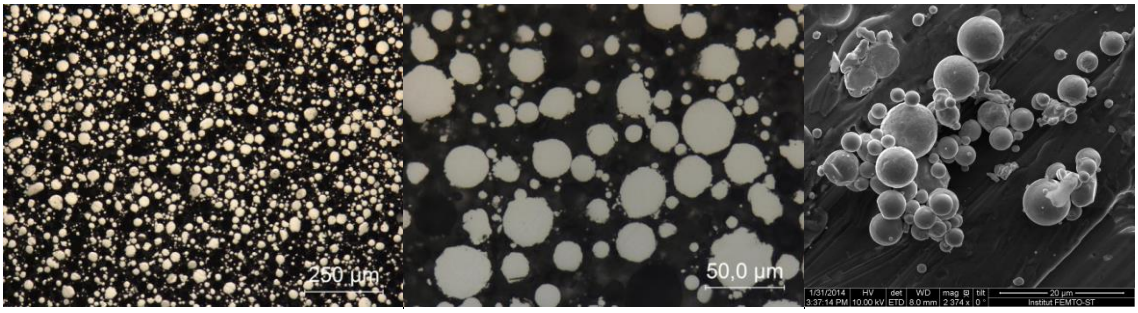

Figure III. 1 OM images and SEM image of the commercial powder (Inconel 718 S)

The milled powder images are given in Figure III. 2. The morphology was completely modified after the ball milling, shows more an irregular flake shape instead of the spherical one, which is not the most adequate during feedstock elaboration. Some of the particles also have cracks in the centre. They can be created during the shocks between the milling balls and the particles or by the forced connection between two or more particles. The particle size measured may be less meaningful as the morphology is not uniform in all the directions. The thickness of the flakes is under 5 µm and the largest particles are around 15 µm.

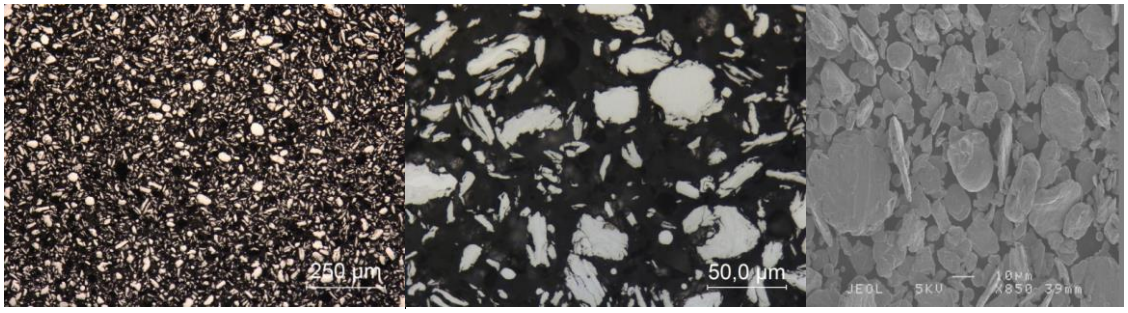

Figure III. 2 OM images (above) and SEM image (below) of the milled powder (Inconel 718 M)

III.2.2 Laser Granulometry

Particle size distribution may be measured by laser granulometry. This method is able to estimate particle size between 0.01 and 3000 µm, by estimating the dimensions of their diameter via the theories of Mie scattering and Fraunhofer diffraction. The method is a fast way to obtain a granulometric distribution on a small quantity of powder. The analysis can be done via a dry way or via a liquid way. The liquid way decreases the chances of agglomeration of the powder during the test and has to be considered in first. The measurement is obtained by observing the interaction between an incident laser beam and a particle group, giving a diffraction shadow of the particle (Figure III. 3).

According to Fraunhofer diffraction theory, the intensity of the diffracted light and the diffraction angle are both function of the particle size [9]. The smaller the particle is, the biggest is the diffraction angle. For particles lower than 100 µm, the Mie scattering theory is more precise [10], which is our case. The granulometric distribution is obtained via images treatment, by converting treatment signal converted with algorithms into a diffraction equivalent diameter. It is leading to a number of particles attributed to a size range, and finally a size distribution. This method can only be applied to specific conditions: the particles must be spherical, non-porous, opaque, and not agglomerated and finally diffract the light in the same way, whatever the particle size. Hence, this method can only be applied to the commercial powder, as the milled powder is not spherical.

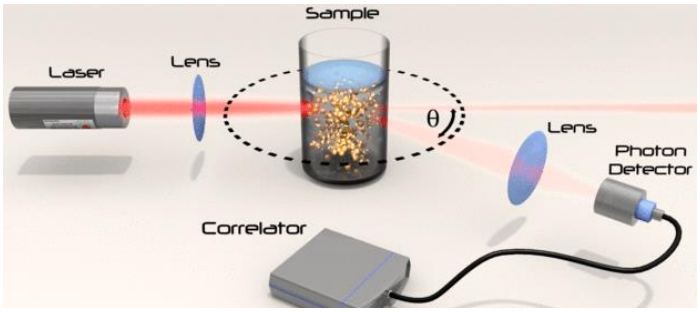

Figure III. 3 Typical set up of a laser granulometer [11]

The powder is introduced in a water circuit, introducing the mix inside a glass cell lit by a laser beam with a wavelength between 33 and 466 nm for a measurement precision of 0.1%. The powder was tested after homogenizing the content of the box and done three times, in order to obtain a representative result of the powder size distribution.

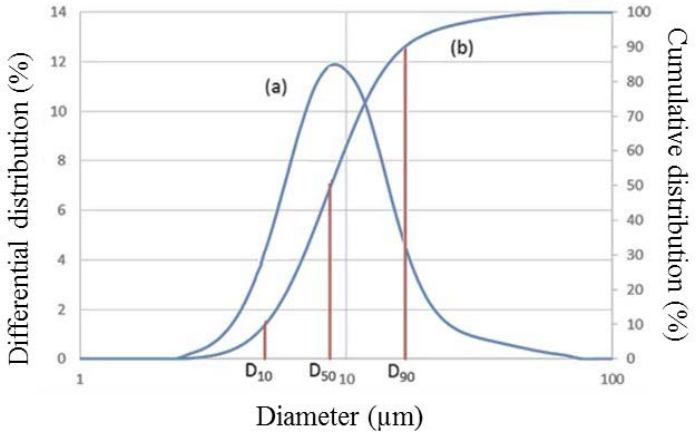

Figure III. 4 Differential distribution (a) and cumulative distribution (b) in function of the particle diameter of Inconel 718 S

The particle distribution follows a mono-modal distribution as the particle size curve is following a normal law. The specific values of the D_{10}, D_{50}, and D_{90} are presented measured as shown on Figure III. 4. The results are presented in Table III. 3.

Table III. 3 Diffraction equivalent diameters obtained by laser granulometry of Inconel 718 S

Powder	D_{10} (µm)	D_{50} (µm)	D_{90} (µm)	S_w	C_u
Inconel 718 S	4.9 ± 0.5	8.7 ± 0.5	16.7 ± 0.5	4.61	1.96

The subscript is corresponding to the percentage of the tested particles group that are under the given value. The D_{90} obtained is of 16.7 ± 0.5 µm, which is inferior to the value given by the supplier. The parameters S_w and C_u are two parameters calculated with the particle distribution. The S_w is representing the slope of the granulometric measurements and is obtained by equation (1). Cu is representing a uniformity coefficient and is obtained by equation (2). They are both values used for checking the injectability of the powder. It is considered to be easy to inject if the parameter S_w is close to a value of 2 and is difficult when over a value of 7 [12]. The uniformity coefficient is helping defining if the distribution size is uniform, if it is under a value of 6. As the S_w coefficient is of 4.61, there could be expectations for some troubles during the injection.

$$Sw = \frac{2.56}{\log\frac{D_{90}}{D_{10}}} \quad (1) \qquad Cu = \frac{D_{60}}{D_{10}} \quad (2)$$

III.2.3 Specific surface analysis

Analysis of the specific surface corresponds to the measurement of the physisorption of nitrogen by the powder. The measurement is obtained via an ASAP 2020 Micrometrics equipment. Samples are weighed and put inside analysis glass tubes. The tube is then placed into a gas extraction unit were the temperature will be progressively raised under vacuum until reaching 90 °C at a heating rate of 10 °C/min. After a dwell time of one hour, the temperature is raised to 350 °C at the same rate. It is maintained during four hours and is cooled down. This step is made in order to get rid of the absorbed gas by the powder before the introduction inside the tube.

The tube is then transferred into the analysing unit, maintained at a temperature of -200 °C with liquid nitrogen. An inert gas is then little by little inserted with a precise control. These gas injections will be absorbed at the surface of the powder, and finally to a uniform layer of gas. The gas volume needed to fill all the porosities is leading to the specific surface. It is obtained by the interpretation of the measures via the model of Brunauer, Emmett and Teller (BET)[13]. The diameter with the equation (3) simplified into equation (4) with the supposition of having a spherical particle and the same particle size.

$$Ss = \frac{4\pi\left(\frac{D}{2}\right)^2}{\left(\frac{4}{3}\right)\pi\left(\frac{D}{2}\right)^3 \rho} \quad (3) \qquad D = \frac{6}{Ss\,\rho} \quad (4)$$

Table III. 4 Specific surface measured on Inconel 718 spherical and flake shape powders and calculated diameters

Sample	Specific surface (m²/g)	D_{BET} (µm)
Inconel 718 S	0.0679 ± 0.0023	10.78
Inconel 718 M	0.3748 ± 0.0011	1.95

The specific surface can be used as an indicator for the feedstock elaboration. In the thesis of Bricout [14], it was shown that the more specific surface is important, the more the powder shows potential for segregation during the mixing. Hence, if the powder agglomerates, the maximum quantity of powder that can be introduced inside the polymeric binder is reduced. In the case of the powders, the measured specific surface gives a particle diameter shown in Table III. 4. These values supports the ones measured during the microscope observations. The diameter obtained for Inconel 718 S of 10.78 µm is between the D_{50} and the D_{90} previously measured. In the case of the milled powder, the specific surface has decreased of half compared to the starting material. Once again, the

size obtained is relative, as it is difficult to consider a spherical diameter for the flake shape particle but it can give an approximation idea of the particle size of the particles. The information that can be extracted is that the particle size was effectively decreased thanks to the milling.

III.2.4 Powder rheology

Powder behaviour in the case of a flow movement is complex, mostly because of inter-particular cohesive forces, that may lead to a segregation of the powder. It is mostly attributed to the different kinds of links that could be created, such as electrostatic attraction, and chemical or Van der Walls bonds [15], [16]. The more cohesive is the powder, the less is its flowability, which can bring difficulties during the feedstock elaboration, and impact the final quality of the components. It is even more difficult to break with mechanical processing [17]. The rheological behaviour of the powder depends of physical and morphological properties of the particles, the particle size and cohesive forces distribution and the environment of the powder such as the temperature, the humidity or the PH if it is in a liquid [18].

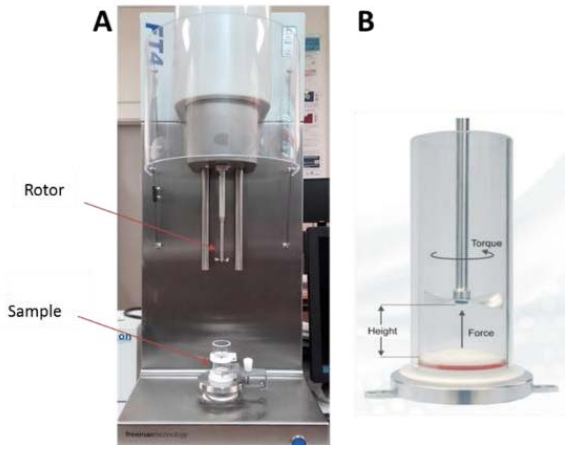

Figure III. 5 FT4 powder rheometer (A) and the shape of the blade used during the tests (B)

The powder rheology measures the dynamic behaviour of the powder. The equipment used to perform the tests is a FT4 from Freeman Technology (Figure III. 5). The measured parameters, under different kind of tests are the normal stress applied, the resistivity of the rotor in contact with the powder and the displacement of the rotor. These parameters are influenced by the properties of the powder, such as the cohesion between the particles, the compressibility and the permeability. Leturia et al [19] shown that the use of powder rheometer, compared to traditional methods of powder characterization, allows repeatable and close estimated values of these parameters.

The different tests are performed five times after a conditioning of the powder which will homogenize the sample tested and erase the history of the powder. This methodology is proposed by Freeman et al [20] in order to obtain the different properties of the powder in standard conditions. In our case, our powder is corresponding to the C group, according to Geldart classification [21] of the powders in function of their particle size. It means that the powder behaviour should belong to the cohesive group. Yet a cohesive group is a problem during the feedstock elaboration as it will reduce the possibility of the polymer to individually surround the powder particles.

The first test performed is a compressibility test (Figure III. 6). As shown on the description of the test, it consists of applying a normal stress on the powder and measure the distance variation with the starting position. The higher is the compressibility percentage is, the lower is the cohesion of the powder. At first, the milled is much more sensitive to compression as the spherical powder, meaning that the milled powder is more filled with empty spaces than the spherical, because of a less homogeneous repartition of the particles. At the end of the test, the final compressibility percentage of the powders is better for the spherical powder than the flake shape.

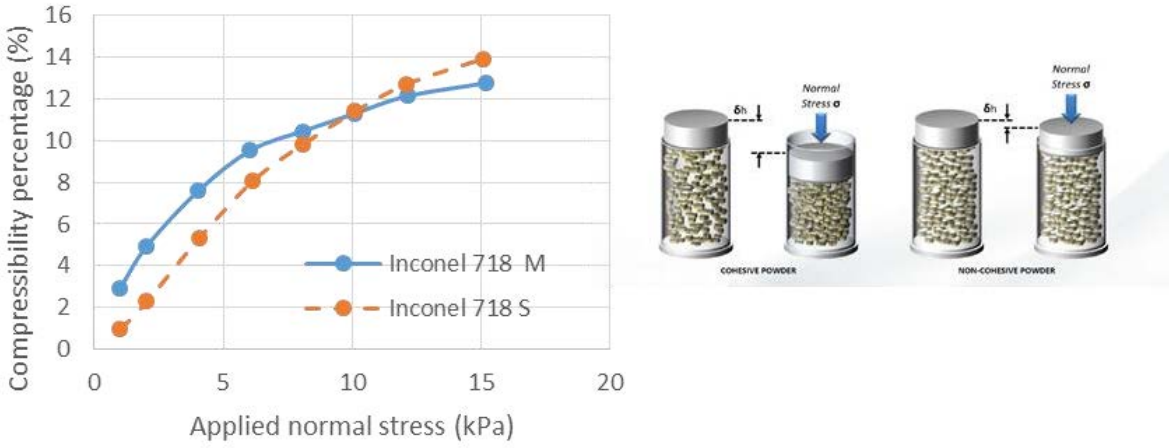

Figure III. 6 Compressibility of the powders in function of the normal stress applied during the compressibility test

The second test is a permeability test (Figure III. 7), set-up just as a compressibility test, but with an air flow applied at the bottom of the powder. It will quantify the capacity of the powder to let trough a fluid. The results are that the milled powder is more permeable than the milled powder, and the effect of the compression is not affecting this parameter. In the case of the spherical powder, it is decreasing constantly with the lowering of free spaces trough the particles. The behaviour of the powders during this test is coherent with the one observed during the compressibility test.

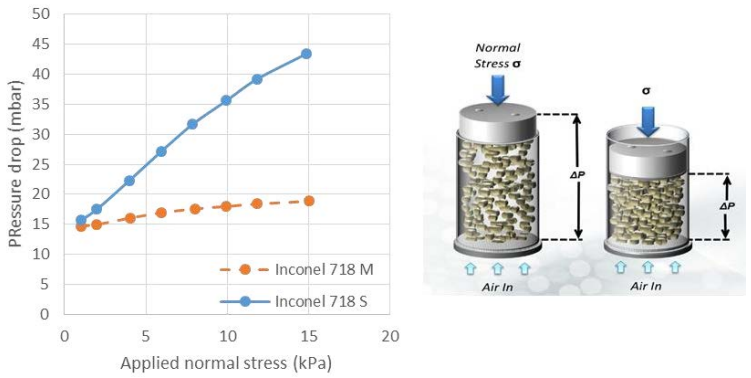

Figure III. 7 Pressure drop inside the powders in function of the normal stress applied during the permeability test

The last test is a ventilation test (Figure III. 8). A blade rotor is introduced inside the powder at constant rotation speed and displacement variation, while measuring the energy needed for the rotor movement. It is performed at different air flow rates. It will help to quantify the cohesion between the particles. The result shows that the milled powder is much less cohesive than the spherical powder. Once again, the rheological behaviour of the powders is coherent with the two previous tests.

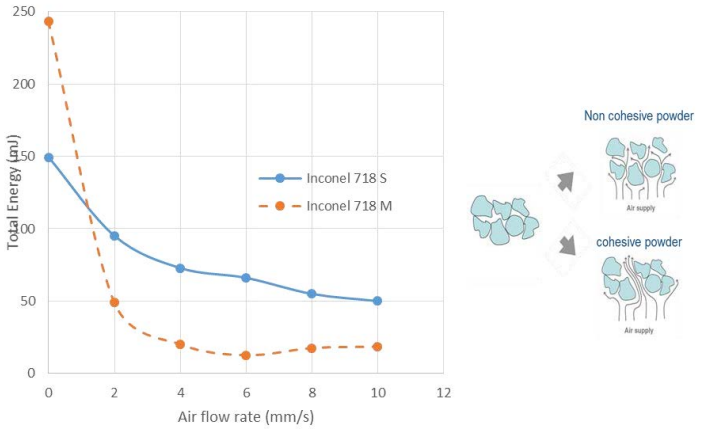

Figure III. 8 Energy needed for the rotation of the blades inside the powders in function of the air flow rate applied during the ventilation test

The different tests realised on the two powders brought important information for the next steps which are the feedstock elaboration and the injection. The spherical powder have a cohesive behaviour, with a high compressibility percentage, confirmed with permeability and the ventilation tests. This could be a sign for some problems during the homogenization of the feedstock inside the mixing chamber. On the other hand, the morphology and the particle size distribution is meeting the requirements for the MIM process.

The milled powder is difficult to conclude on, as it has a flake shape. The particle size distribution was lowered, and shows a less cohesive behaviour than the spherical powder. Nevertheless, the black point of the process is the loss of the spherical that could have a huge impact on the injection, as it will perturb the injection flow and will lower the maximum powder loading. However, it is interesting to compare the difference of behaviour while using the supercritical debinding method.

III.3 Binders characterization

The composition and the characteristics of the binder is of outmost importance in order to assure the homogeneity of the component during the injection. It also has to be easily eliminated smoothly during the debinding, leaving the system without damaging the shape and leaving too much residues after complete degradation. Two binders were used during this work and are presented in Table III. 5. They are both composed of PEG and SA, the difference being the primary binder. The first one was developed with PP (Binder A) and the second one with CAB (Binder B).

Table III. 5 Composition of the binders A and B

Binder A	PP 670 KH	PEG 20K	SA
Vol. fraction (%)	40	55	5

Binder B	CAB 30K	PEG 4K	PEG 20K	SA	PTZ
Vol. fraction (%)	30	50.30	16.75	2.5	0.5

The Binder A is a conventional binder in MIM process for manufacturing components with micro details [22]. It was also recently used for realizing aeronautic parts with intermetallic material for two thesis [4], [23]. The binder B was also developed during two thesis [1], [2] with fine ceramic powders and Invar 36 alloy. The binder B has phenothiazine (PTZ) in its composition, in order to avoid thermal degradation of the CAB properties during the mixing. Both of the binders were optimized in term of rheological behaviour during mixing and injection steps and the solvent extraction and thermal degradation were also successfully performed.

III.3.1 Thermal properties characterization

The thermal properties of the polymers composing the binders are important in order to set up the conditions of mixing, injecting and debinding. The use of the good temperatures will help to avoid degrading the polymers, hence modifying the chemical and mechanical properties of the binder which could lead to defects inside the component. They were determined by analysing differential scanning calorimetry curves. The temperatures for mixing and injection should be found between the fusion and the degradation temperatures and the debinding temperatures above the degradation temperature. As the mixing of the polymers together may bring chemical modifications, the debinding temperature will have to be checked again after the mixing of the feedstock.

Table III. 6 Temperatures of fusion and degradation of the polymers

Materials	PP	CAB	PEG 20K	PEG 4K	SA
Fusion Temperature (°C)	155 ± 2	158 ± 1	67 ± 2	56 ± 2	68 ± 2
Degradation Temperature (°C)	355 ± 1	362 ±2	350 ± 1	274 ± 3	181 ± 1

In accordance with the results of Table III. 6, the mixing and injection temperatures of Binder A have to be between 155 and 180°C, and between 160 and 180°C for Binder B. As most of the PEG will be extracted by solvent debinding, the debinding temperature will be dependent of the degradation temperature of the primary binders CAB and PP, hence it will be tested above 355 °C for Binder A and 362 °C for Binder B.

III.3.2 Rheology of the binders

The rheology tests were realised with both rotating and capillary rheometers at a set temperature of 180°C, above the melting temperatures of the different polymers. The tests were performed in a permanent regime for a shear rate going from 0.01 s^{-1} to 200 000 s^{-1} by combining the two equipment (Figure III. 9). This will help to cover the shear rates met during both the mixing and the injection steps. It is found that all of the polymers displays a typical pseudo plastic behaviour at low shear rate, followed by the shear thinning at high shear rate, similar to most of thermoplastic polymers. The difference between the two primary binders is the shear rate around 100 s^{-1}, corresponding to the

mixing steps. A lower shear rate is allowing a higher maximum powder loading. The PEG and the SA displays a low viscosity with a Newtonian behaviour at low shear rate and the measurements at higher rate were not possible due to their shear viscosity that was too low for the capillary rheometer tests.

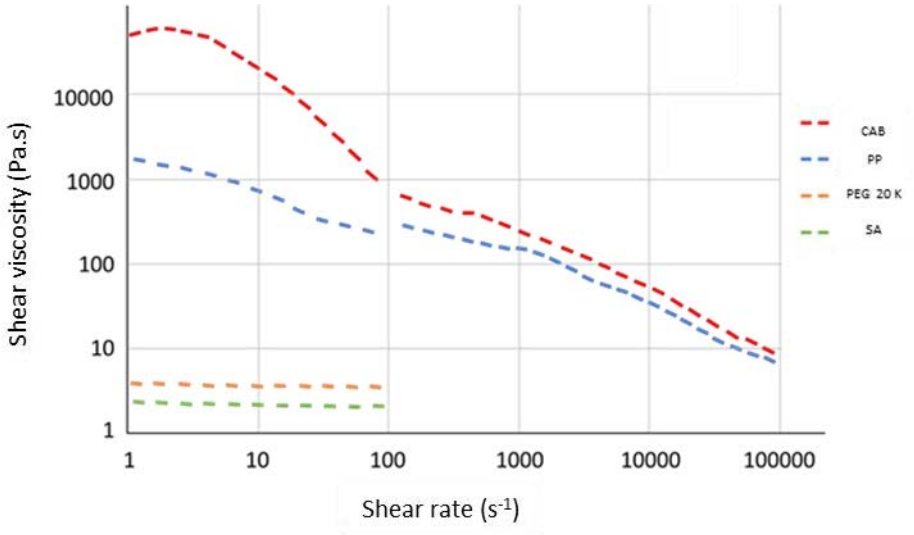

Figure III. 9 Shear viscosity in function of the shear viscosity obtained by rotating and capillary rheometers of the different elements composing the binder

Binder A and Binder B thermal and rheological behaviour were analysed in order to assure the compatibility with the mixing, injection and debinding steps of the MIM process. It is possible for both of them to perform the mixing and the injection around 180 °C. Their degradation temperature are also below the first transformation phase observed in part II.1.4, which are above 500 °C. The thermal debinding of the two binders can be performed without perturbing the thermal treatment of Inconel 718.The decision of using two different binders will help for the supercritical fluid debinding method, in order to determine if the primary binder has an influence on the debinding rate and on the final state of the sample.

III.4 MIM component elaboration and consolidation

The different equipment of each steps of the MIM process are presented in Figure III. 10. First, the feedstocks are elaborated with a twin screw mixer Brabender Plastograph EC W50EHT, which records the evolution of the mixing torque in function of the processing parameters (time, temperature, blade velocity). It will help to observe when the homogenization of the feedstock is

complete. The final mixing torque measured will also be an indicator of the difficulty of injection of the prepared feedstock if its value is too high as it is linked to the shear viscosity of the feedstock. A fixed rotation speed of the rotor was at 50 rpm in order to obtain a homogenous feedstock without powder segregation and all the components of the feedstocks were added at the same time.

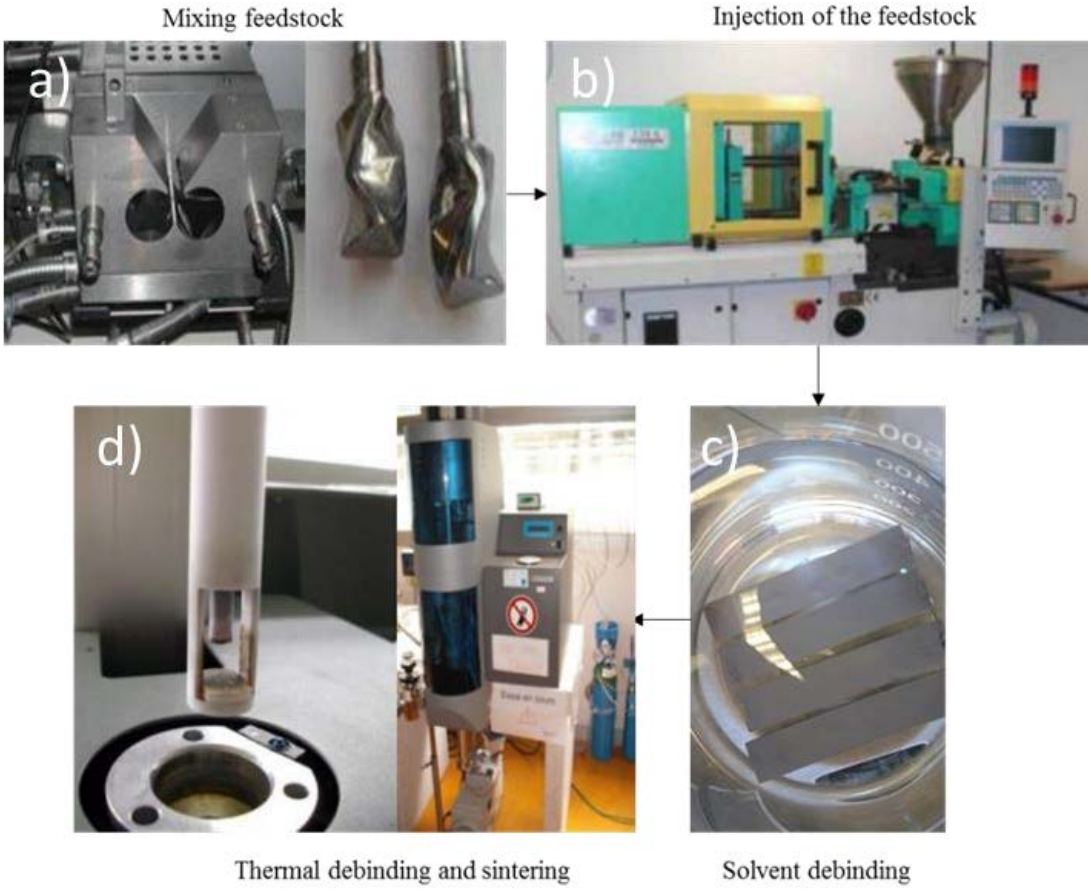

Figure III. 10 Equipment used during conventional MIM process: a) Brabender Plastograph EC W50EHT, b) Arburg 220S, c) solvent debinding set-up, d) Setaram Setsys EVO 2400

The injection temperatures varies between 160 and 180 °C in order to optimize the injection temperatures without reaching the degradation temperatures shown in Table III. 6. Injection pressure and flow were also optimized in function of the binder, the powder selected and the MIM shape selected. The samples were injected with a hydraulic injection press Arburg 220S into two different shapes, one into cylinders of 10 mm diameter and 35 mm length, the second into bars of 60 mm length, 10 mm width and 3 mm thick. The cylinder shape was chosen because of the geometrical restrictions of the FAHP equipment and the dilatometer. They can be cut in samples of 10 mm or 20 mm of length in order to perform the different tests during this thesis.

Table III. 7 Technical specifications of the Arburg 220S

Clamping force	20 kN
Injection volume	3 to 12 cm^2
Screw diameter	15 mm
Screw length	600 mm
Injection speed (max)	366 mm/s
Injection temperature (max)	400°C
Injection pressure (max)	250 MPa
Injection flow (max)	22 cm^3/s

The water soluble PEG is debinded by immerging the components into deionized water, heated and stirred. The temperature can vary from room temperature to 80 °C in order to get rid of the PEG. The temperature of the solvent is important as the PEG is easier to remove when it is in a molten state [24]. The thermal debinding can be done in a debinding oven, under argon atmosphere and continuous flow in order to take out the residues from the degradation of the polymers. The sintering is done in a controlled argon atmosphere in order to reach the sintering temperatures of the Inconel 718 while avoiding pollution of the microstructure by the atmosphere. These two steps are also performed inside a Setaram Setsys evolution 2400, in a dilatometer mode, in order to follow the shrinkage of the components during the sintering.

At the end of each steps, the feedstocks and the components are evaluated in terms of mass, geometry or surface quality. The surface of the samples is also controlled by the use of roughness measurements. They are performed with a microscope combined with an Alicona Infinite Focus equipment in order to obtain a 3D profile of the samples. The same methodology of characterization of the components is performed for the new debinding and sintering methods. These equipment will be further introduced in the next chapters. The three equipment and methodology is developed during the tests, thus it is easier to describe them along the optimization process.

III.5 Bulk material characterization

It is only possible to affirm that the mixing, the injection, the debinding and the sintering parameters are optimized if the MIM components are respecting the needed specifications in terms of shape, geometry, microstructure and mechanical properties. This part describes the methodology used to analyse the consolidated components and the preparations methods in order to perform these analyses.

III.5.1 Microscopy

The polishing of the samples was prepared by standard metallographic techniques, by grinding under water the samples with silicon carbide sand paper and gradually rising the paper grade from 180 to 2400. The surface is getting a mirror finishing via the use of micrometrics alumina particles, allowing the observation by microscopy of the final microstructure of the samples.

Electro-polishing (EP) on a metallic component is also carried out on some samples by polarizing the bulk material while it is in polished with an acid. The commonly used solutions for EP are composed of one or more concentrated acids, such as perchloric, sulfuric, phosphoric and acetic acids [25]. In our case the polished surfaces were electrolytically etched at 4.5V during 10 seconds in a 5% aqueous sulphuric acid solution which preferentially etches the precipitates [26], helping to reveal the grain joints and the niobium phases at the surface as seen on Figure III. 11.

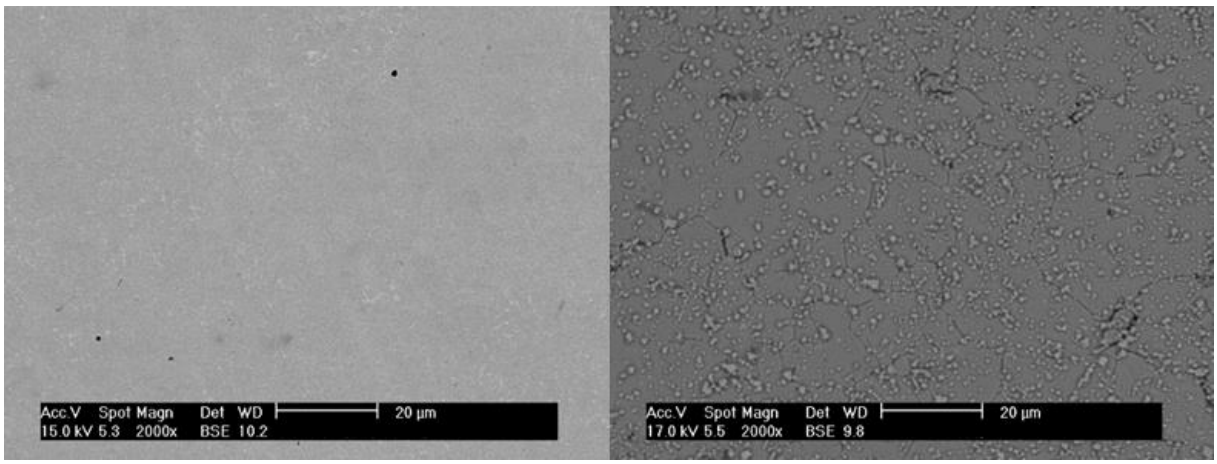

Figure III. 11 SEM images of a sintered Inconel 718 MIM component taken before and after EP

Light optical microscopy (LOM) was used for the microstructure evaluation of the injected and metallic materials evaluated during this work. Microstructure and porosity features can be evaluated with LOM in the case of Inconel 718 thanks to the grinding and the polishing. It asssures that the porosities of the material are properly opened. To reveal the position of the different Niobium phases, the electro-polishing will help to reveal these details.

Scanning electron microscopes (SEM) has also been employed for a more detailed microstructure evaluation. By using the excitation of a tungsten filament at vacuum conditions and an accelerating voltage around 20 kV, an electron beam is created and focused on the surface of the material. The interaction of the beam with the material will release three different signals collected by detectors inside the equipment, which will be used to create magnified image. There are two different modes possible, a backscattering electrons mode will help to reveal compositional contrast as well as the different phases. The secondary electron mode allows distinguish the topographic details, helping in finding possible porosities or cracks.

The equipment has also a chemical analysis system with an energy disperse spectroscopy probe (EDX), allowing to perform semi-quantitative elements analysis. They informs on the quantity percentage of the chemical elements found on a given zone of the observed surface. The relevance of the information given by this test depends of the depth of the beam when reaching the elements presents inside the designated zone.

Finally, transmission electron microscopy (TEM) uses the same kind of interaction between an electron beam and the material. The difference is first in a more powerful the beam being in general accelerated with a voltage between 100 and 300 kV. The second difference is that the material has to be of a thickness under 100 nm in order to let the beam go through the sample. An image is formed from the interaction of the electrons with the sample as the beam is transmitted through the specimen which is then magnified and focused onto an imaging device in order to observe at a magnitude high enough to distinguish the atoms inside the material.

It was performed in order to identify the phases created inside the material. The blade was prepared inside a SEM by milling the material with a focused ion beam (FIB) by following the standard preparation [27]. Once the membrane is prepared (Figure III. 12), it is then mounted on a grid allowing the transfer of the sample into the TEM equipment.

The TEM observations were performed by following the methods described in A. Niang et al [28]. It is explained that the δ, γ’ and γ’’ phases are commonly observed with epitaxial relations with the

FCC structure of the matrix of the Inconel 718. By following the [1 1 1] plane, he was able to observe these phase inside the matrix. The TEM observations will help to identify the created phases inside of the grains of the Inconel 718 bulk material and to determine if the applied thermal treatments are modifying the composition of the microstructure of the material.

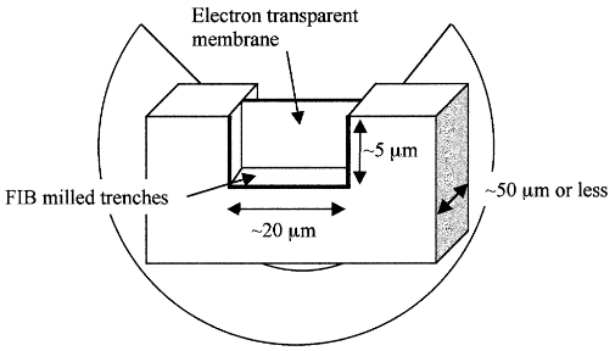

Figure III. 12 schematic diagram of a conventionally prepared FIB TEM specimen [27]

III.5.2 Tensile strength tests

The mechanical tests of some samples was performed by using micro-tensile strength tests because of the small size of the injected samples. Thus, in order to perform this test, the material was cut in the sintered components in order to fit with the geometry and the dimensions needed by the equipment (Figure III. 13). It was performed by using wire electrical discharge machining (EDM). Material is removed from the workpiece by a series of rapidly recurring current discharges between two electrodes separated by a dielectric liquid [29], which is water in our case. This method was chosen because of the precision of the cutting and the absence of modification of the phases of the Inconel during the contact with the wire. [30].

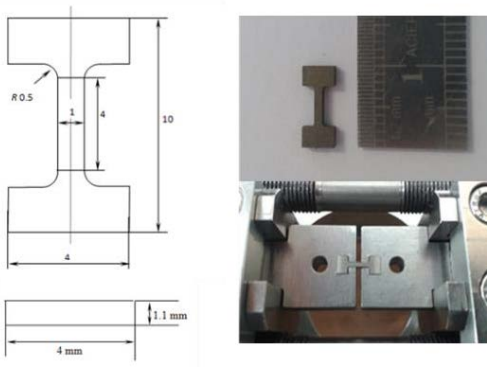

Figure III. 13 Drawings of the samples for the micro-tensile strength tests

In order to confirm the viability of the methods developed in this work, different mechanical characterizations were applied to the materials in order to compare with the specifications asked by the industrial partners. This part will introduce the methodologies of the tests employed. A Kammrath and Weiss micro-mechanical testing stage with a load cell of 1 kN (Figure III. 14) was used to perform micro tensile strength tests at room temperature. The data is collected directly from the cross head displacement without any extensometers. Thus there is a probability of errors in strain measurements [31]. Experiments were also performed inside a SEM in order to observe in-situ, during the test, the behaviour of the material and microstructural changes. It was also possible to obtain fracture images once the material broke in order to conclude on the strain mechanism involved in the fracture type. As the loading cell of 1 kN of the micro-tensile strength test equipment was sometimes not enough to reach the rupture of the material, some tests were also performed on a MTS Criterion Model 45 tensile test equipment. It was possible to observe the elongation of the samples by using a video camera fixed in front of the samples.

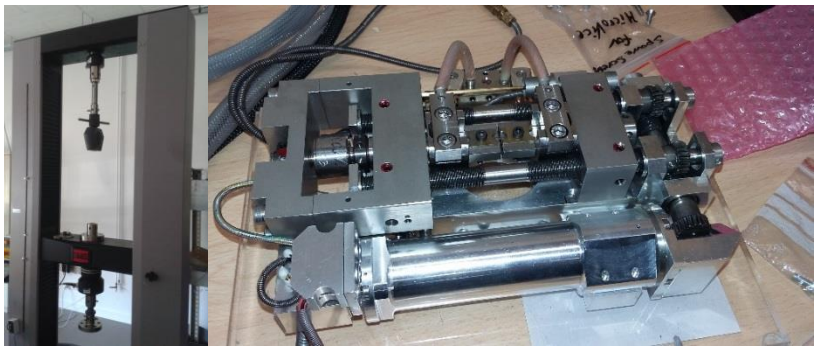

Figure III. 14 Tensile strength test and micro-tensile strength test equipment

III.5.3 Hardness characterization

For the evaluation of the hardness, micro-hardness expressed in Vickers (HV) standard was selected and was measured while following the ASTM E384 standard [32]. They were obtained with a HVS-1000 tester. The tests are done the same as a standard Vickers test, but at a microscopic scale. A load of 1.0 N was applied during 10 seconds in order to obtain a good footprint on the material. The footprint diagonals are measured in order to get the footprint area. Then the applied force divided by this value gives the hardness in HV of the zone tested. In order to confirm the homogeneity of the component, the indentation is repeated between 3 and 5 times, depending of the standard deviation of the results, in different zones between its centre and its extremity (Figure III. 15).

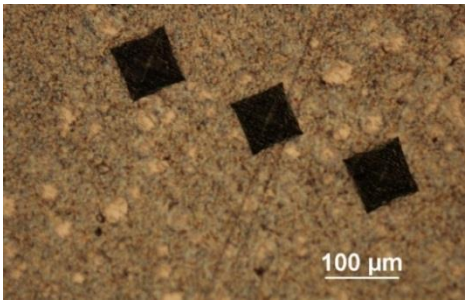

Figure III. 15 Example of Vickers footprint obtained on Inconel 718 samples

III.5.4 Nano-indentation test

The nano-identation method was developed to measure the hardness and elastic modulus of a material from indentation load–displacement data obtained during one cycle of loading and unloading. In our case, it was developed with a triangular pyramid. The load placed on the indenter tip is increased as the tip penetrates further into the specimen and soon reaches a user-defined value. By realizing multiple nano-indentation in a chosen zone, it is even possible to realize a mapping of the distribution of the hardness and the Young modulus. A schematic representation of a typical data set obtained with a Berkovich indenter is presented in Figure III. 16. The parameter *P* designates the load and *h* the displacement relative to the initial un-deformed surface.

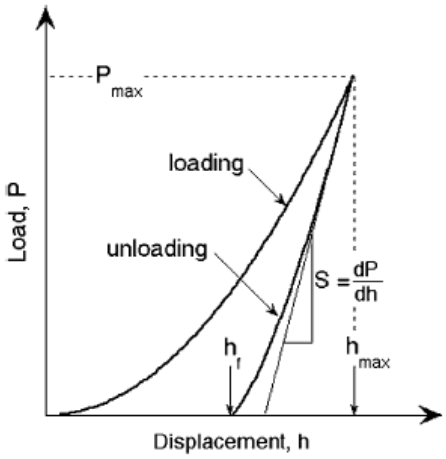

Figure III. 16 Schematic illustration of indentation load–displacement data showing important measured parameters[33]

The area A (h_c) of the residual indentation in the sample is measured on the indentation print after the indentation. The most usual methodology for extraction of the projected contact area developed by Oliver & Pharr [33], where ε is a parameter approximately equal to 0.75 for a Berkovich indenter

and S is the is the unloading contact stiffness at maximum depth (Eq. 2). This value generally includes a contribution from both the material being tested and the response of the test device itself.

$$h_c = h_{max} - \varepsilon \frac{P}{S} \quad (1) \qquad S = \frac{dP}{dh} \quad (2)$$

The hardness is defined at the maximum load P_{max}. The value of H is obtained by dividing this maximum load by the residual indentation area (Eq. 3). The slope of the curve dP/dh, upon unloading, is indicative of the stiffness S of the contact which can be used to calculate the reduced Young's modulus E_{eff} (Eq. 4), where β is equal to 1.034 for a Berkovich indentation. This parameter takes into account the lack of symmetry of this type of indenter [34].

$$H = \frac{P_{max}}{A(h_c)} \quad (3) \qquad E_{eff} = \frac{1}{\beta} \frac{\sqrt{\pi}}{2} \frac{S}{\sqrt{A(h_c)}} \quad (4)$$

III.6 Partial remarks

This part introduced the raw materials that are used during this work as well as their morphologies. The first one is a spherical powder designated Inconel 718 S that will be easy to use in the elaboration of a feedstock. The second powder is a flake shaped powder designated Inconel 718 M that shown difficulties during compaction and that will be more delicate during the feedstock and injection mixing but the permeability test nuances the previous results as this powder has a less cohesive behaviour, meaning that the binder will be able to wrap the particles more easily than the spherical powder. The two selected binders have a rheological behaviour that is adapted to the injection equipment. The thermal properties of the binders will allow a debinding cycle that will not perturb the thermal behaviour of Inconel 718. Finally, all of the equipment and standard methods used to elaborate and characterize the components during this work are presented. They will help to understand the effect of the new methods introduced in this project. The effects on the final quality of the MIM components, being the microstructure, the chemical modifications, the mechanical properties or the final appearance of the component can be characterized. These information will help to adapt both the conventional and the new debinding and sintering methods to the Inconel 718 MIM component behaviour.

REFERENCES

[1] J. Hidalgo Garcia, « Development of Binder Systems Based On Cab for Powder Injection Moulding (Pim) and Micro Powder Injection Moulding (µ-Pim) Of Zircon and Invar Powders », Universidad Carlos III De Madrid and Université De Franche-Comté, 2014.

[2] C. Abajo Clemente, « Development And Optimization Of An Eco-Friendly Binder System For Ceramic Injection Moulding Of Zirconium Silicate », Universidad Carlos III De Madrid, 2016.

[3] A. Royer, « Etude, Caractérisations Et Développement De Mélanges De Polymères Biosourcés Chargés De Poudre D'inconel 718 Pour L'élaboration De Composants Et Micro-Composants Via Moulage Par Injection De Poudres Métalliques », Université De Franche-Comté, 2016.

[4] D. Claudel, « Modélisation Et Identification De Lois Rhéologiques De Polymères Chargés. Application Au Procédé De Moulage Par Injection De Poudres De Superalliages. », Université De Franche-Comté, 2016.

[5] W.-W. Yang, K.-Y. Yang, Et M.-H. Hon, « Effect Of Peg Molecular Weights On Rheological Behavior Of Alumina Injection Molding Feedstock », *Mater. Chem. Phys. 782416-424 · Febr. 2003*.

[6] B. O. Haglund, « Solubility Studies Of Polyethylene Glycols In Ethanol And Water », *Thermochim. 114 1987 97-102*.

[7] S. T. Lin Et R. M. German, « Interaction Between Binder And Powder In Injection Moulding Of Alumina », *J. Mater. Sci.*, Vol. 29, Nº 19, P. 5207‑5212, Oct. 1994.

[8] X. Liang, J. C. Earthman, Et E. J. Lavernia, « On The Mechanism Of Grain Formation During Spray Atomization And Deposition », *Acta Metall. Mater.*, Vol. 40, Nº 11, P. 3003‑3016, Nov. 1992.

[9] N.-N. Wang, H. J. Zhang, Et X.-H. Yu, « A Versatile Fraunhofer Diffraction And Mie Scattering Based Laser Particle Sizer », *Adv. Powder Technol.*, Vol. 3, Nº 1, P. 7‑14, 1992.

[10] G. B. J. De Boer, C. De Weerd, D. Thoenes, Et H. W. J. Goossens, « Laser Diffraction Spectrometry: Fraunhofer Diffraction Versus Mie Scattering », *Part. Part. Syst. Charact.*, Vol. 4, Nº 1‑4, P. 14‑19, Janv. 1987.

[11] « Dynamic Light Scattering For Particle Sizing And Measurement Of Particle Size Distribution ».Http://Www.Lsinstruments.Ch/Technology/Dynamic_Light_Scattering_Dls/.

[12] B. Mamen, J. Song, T. Barriere, Et J.-C. Gelin, « Experimental And Numerical Analysis Of The Particle Size Effect On The Densification Behaviour Of Metal Injection Moulded Tungsten Parts During Sintering », *Powder Technol.*, Vol. 270, Part A, P. 230‑243, Janv. 2015.

[13] S. Brunauer, P. H. Emmett, Et E. Teller, « Adsorption Of Gases In Multimolecular Layers », *J. Am. Chem. Soc.*, Vol. 60, Nº 2, P. 309–319, 1938.

[14] J. Bricout, « Fabrication Du Combustible Nucleaire Par Injection: Etude De La Formulation Et Du Déliantage D'une Pâte Contenant Des Actinides », Franche-Comté, 2008.

[15] R. H. R. Castro, G. J. Pereira, Et D. Gouvêa, « Surface Modification Of Sno2 Nanoparticles Containing Mg Or Fe: Effects On Sintering », *Appl. Surf. Sci.*, Vol. 253, Nº 10, P. 4581‑4585, Mars 2007.

[16] S. Ross Et I. D. Morrison, *Colloidal Systems And Interfaces*. Wiley, 1988.

[17] C. Xu Et J. Zhu, « Experimental And Theoretical Study On The Agglomeration Arising From Fluidization Of Cohesive Particles—Effects Of Mechanical Vibration », *Chem. Eng. Sci.*, Vol. 60, Nº 23, P. 6529‑6541, Déc. 2005.

[18] M. D. Ashton, D. C.-H. Cheng, R. Farley, Et F. H. H. Valentin, « Some Investigations Into The Strength And Flow Properties Of Powders », *Rheol. Acta*, Vol. 4, Nº 3, P. 206‑218, Oct. 1965.

[19] M. Leturia, M. Benali, S. Lagarde, I. Ronga, Et K. Saleh, « Characterization Of Flow Properties Of Cohesive Powders: A Comparative Study Of Traditional And New Testing Methods », *Powder Technol.*, Vol. 253, P. 406‑423, Févr. 2014.
[20] R. Freeman, « Measuring The Flow Properties Of Consolidated, Conditioned And Aerated Powders — A Comparative Study Using A Powder Rheometer And A Rotational Shear Cell », *Powder Technol.*, Vol. 174, Nº 1–2, P. 25‑33, Mai 2007.
[21] O. Molerus, « Interpretation Of Geldart's Type A, B, C And D Powders By Taking Into Account Interparticle Cohesion Forces », *Powder Technol.*, Vol. 33, Nº 1, P. 81–87, 1982.
[22] D. Moinard, C. Rigollet, Et P. Lourdin, « Powder Injection Moulding Pim Of Feedstock Based On Hydrosoluble Binder And Submicronic Powder To Manufacture Parts Having Micro-Details », *Powder Techonology*, Nº 208(2), P. 472‑479, 2011.
[23] P. Tourneroche, « Développement De Mélanges Chargés En Poudres D'aluminure De Titane Pour Moulage Par Injection Et Applications Aéronautiques », 2016.
[24] W.-W. Yang Et M.-H. Hon, « In Situ Evaluation Of Dimensional Variations During Water Extraction From Alumina Injection-Moulded Parts », *J. Eur. Ceram. Soc.*, Vol. 20, Nº 7, P. 851‑858, Juin 2000.
[25] J. R. Scully Et R. G. Kelly, « An Electrochemical Test For Detecting The Intergranular Corrosion Susceptibility Of A Duplex Stainless Steel », *Corrosion*, Vol. 42, Nº 9, P. 537‑542, Sept. 1986.
[26] P. A. Davies, G. R. Dunstan, R. I. L. Howells, Et A. C. Hayward, « Metal Injection Moulding Of Heat Treated Alloy 718 Master Alloy », *Adv Powder Met. Part Mater*, Vol. 8, P. 8‑12, 2003.
[27] L. A. Giannuzzi Et F. A. Stevie, « A Review Of Focused Ion Beam Milling Techniques For Tem Specimen Preparation », *Micron*, Vol. 30, Nº 3, P. 197–204, 1999.
[28] A. Niang, J. Huez, J. Lacaze, Et B. Viguier, « Characterizing Precipitation Defects In Nickel Based 718 Alloy », *Mater. Sci. Forum*, Vol. 636‑637, P. 517‑522, Janv. 2010.
[29] Y. Takayama, Y. Makino, Y. Niu, Et H. Uchida, « The Latest Technology Of Wire-Cut Edm », *Procedia Cirp*, Vol. 42, P. 623‑626, Janv. 2016.
[30] L. Li, Y. B. Guo, X. T. Wei, Et W. Li, « Surface Integrity Characteristics In Wire-Edm Of Inconel 718 At Different Discharge Energy », *Procedia Cirp*, Vol. 6, P. 220‑225, 2013.
[31] Y. H. Zhao *Et Al.*, « Influence Of Specimen Dimensions And Strain Measurement Methods On Tensile Stress–Strain Curves », *Mater. Sci. Eng. A*, Vol. 525, Nº 1, P. 68‑77, Nov. 2009.
[32] *Standard Test Method For Microindentation Hardness Of Materials*. Astm International, 2016.
[33] W. C. Oliver Et G. M. Pharr, « Measurement Of Hardness And Elastic Modulus By Instrumented Indentation: Advances In Understanding And Refinements To Methodology », *J. Mater. Res.*, Vol. 19, Nº 01, P. 3‑20, Janv. 2004.
[34] E. Jiménez-Piqué, Y. Gaillard, Et M. Anglada, « Instrumented Indentation Of Layered Ceramic Materials », *Key Eng. Mater.*, Vol. 333, P. 107‑116, 2007.

IV CONVENTIONAL MIM PROCESS OF INCONEL 718 COMPONENTS

This part introduces the conventional MIM process for the elaboration of Inconel 718 components. The goal of this work is to obtain information on the behaviour of the components during the water solvent debinding and the furnace sintering steps as well as their characteristics after both treatments.

In the first part the feedstock elaboration is presented, using two binders based on CAB and PP as well as two different morphologies of powders. The first step of the elaboration is to optimize the maximum powder loading volume of the binder. The second step is to optimize the mixing parameters which are the temperature and the time of the cycle. The second part is to check the homogeneity of the feedstocks via thermal analysis.

The second part introduces the rheological behaviour and the injection moulding of the components. The injection conditions of the two different shape of component and the optimization of the injection conditions as function of the feedstocks.

The third part determines the effects of solvent and thermal debinding and their influence on the MIM component. The solvent debinding characterizations will be compared to the one obtained after performing the supercritical fluid debinding. The three points that will be important to observe are the efficiency of the debinding cycles of the PEG, the debinding rate and the deformations that the water will bring to the component. The thermal debinding has to be optimized according to the thermal characterization of the binders. It is necessary to optimize this step in order to obtain the best debinding rate while avoiding the apparition of defects on the component. The residual compounds after thermal degradation have to be kept at a lower level possible.

The last part is focused on the sintering and the thermal treatment applied to the Inconel 718 powder. The sintering parameters are optimized since the development of the material [1], [2]. However, the properties of the components shown in the literature where made with different feedstocks and different furnaces. Hence, the furnace sintering is necessary in order to obtain data on the material with our feedstocks. It will also help to understand and compare the behaviour of the material when it will be sintered with FAHP and microwave sintering methods.

The main difficulty of this work is that all of the steps of the MIM process needs to be optimized in order to avoid future problems or defects with the components at the next steps. In order to

complete each steps optimization, the components are characterized via their deformation, density, roughness, and microstructure.

IV.1 Feedstock elaboration

IV.1.1 Mixing and Torque measurement

Torque curve evolution (torque rheology) is one of the main characteristics to be determined to optimize the mixing of the binder with the powder. The torque represents the momentum that is exerted upon the rotors to displace the feedstock during the blending process. It is expressed in N.m and is proportional to the feedstock viscosity and is dependent of the temperature, the shape and the rotation speed of the rotors. In the case of a melted feedstock, the viscosity is influenced by the binder viscosity and the characteristics of the powder such as the morphology and the specific surface. Hence, the powder loading volume, expressed in mass fraction (wt.) %, impacts on the torque rheology and on its stability [3].

The torque rheology shows how the different elements of the feedstock are behaving during the mixing and the difficulty for the system to reach equilibrium. Thus, this method provides a good idea of the homogeneity of the feedstock [4], [5]. By monitoring the torque rheology, it is possible to search for the best experimental processing parameters and the optimal and critical powder loading volume [6].

In order to obtain the critical powder loading, a test is performed by introducing in the mixer a determined quantity of binder then the powder on an incremental basis [7]. If the torque rate is stabilized after the introduction of the elements of the feedstocks inside the mixing chamber, it is a sign of a homogeneous repartition between the powder and the thermoplastic polymer. On the contrary, when the torque rate is unstable, that means that the powder loading has passed a critical value. If a feedstock is prepared with a powder loading volume superior at this value, the homogeneity will be not assured on the totality of the prepared volume. Hence, a lot of the problems may occur during the debinding, the injection and the sintering steps.

All of the mixing tests were performed with a rotation speed of the blades of 50 tr/min [8]. The temperature for mixing the feedstock A was of 175°C and 160°C for feedstock B. The mixing was kept at least 30 min once the torque rate was stable in order to assure the homogeneity of the feedstock.

This first feedstocks were prepared with the spherical powder. The critical powder loading volume was investigated during the mixing of binders A and B. The Figure IV. 1 shows the results obtained with binder B. The torque rate is evolving quite smoothly. At the powder loading volume of 71 (wt.) % the torque rate increases quite brutally, indicating a difficulty for the binder to envelop the powder. Hence, the critical powder loading of the spherical powder is of 71 (wt.) %.

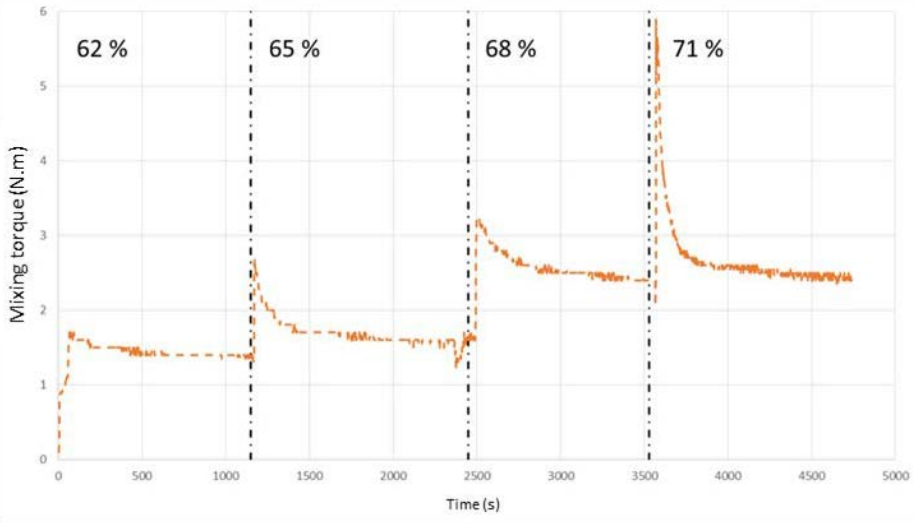

Figure IV. 1 Mixing torque vs time during the elaboration of the feedstock composed of binder B with the spherical powder

The same test was performed with the binder A and the results displayed in Table IV. 1. In the case of binder A, the critical powder loading was obtained at 78 (wt.) %. The binder A can assure the homogeneity with a higher powder loading than the binder B. However, it can also be noticed that the Binder A is opposing more resistance on the blades of the rotor than the Binder B.

From these results, two powder loading volume were selected for binder A, which are 62 and 70 (wt.) %, and only one for binder B, which is 62 (wt.) %. It was observed that the critical powder loading volumes obtained by the incremental method were superior at the volumes tolerated during the injection because of the difference of range of shearing rates [9]. Hence a 62 (wt.) % loading volume was chosen as a safe value in order to avoid problems during the injection. Moreover, it is also possible to create defects when performing the debinding of the polymer inside the MIM component if there is not enough porosity left while the polymer is taken out of the component. In the case of binder A, the powder loading volumes were selected in order to observe its influence on the debinding rate with a supercritical fluid.

Table IV. 1 Mixing torque obtained during the elaboration of the feedstock composed of binder B with the spherical powder

Binder	Powder loading volume (wt.) %	Maximum mixing torque (N.m)	Final mixing torque (N.m)
A	70	16.8	7.1
	72	15.2	8.6
	74	16.1	9.3
	76	21.9	12.4
	78	17.0	-
B	62	1.7	1.3
	65	2.8	1.5
	68	3.3	2.2
	71	6.5	2.3

The same test was performed in order to optimize a feedstock composed of the binder A with the milled powder, presented in Figure IV. 2. At 62 (wt.) %, it is not seen on the curve but the powder was not mixed properly with the powder even after a long mixing time. At 55 (wt.) %, the mixing is easier for the equipment and the obtained feedstock does not show the same behaviour as with 62 (wt.) % of powder loading rate. Thus the chosen powder loading rate will be of 55 (wt.) %.

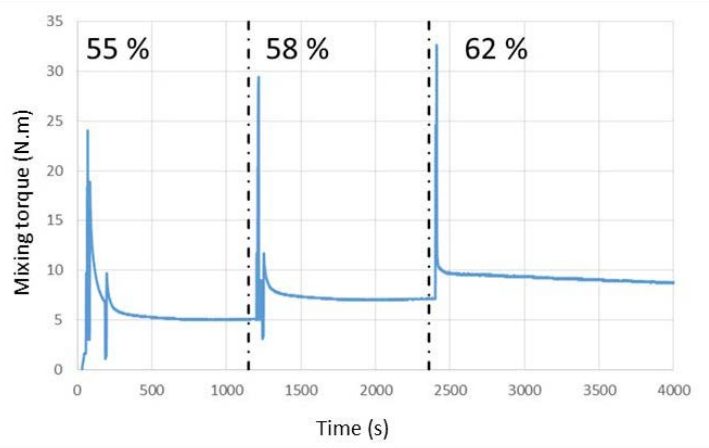

Figure IV. 2 elaboration of the feedstock composed of binder A with the flake shape powder

As it was introduced during the powder rheology, the milled powder shows a low permeability to a fluid, explaining a torque rate much higher and much more difficulty to reach a high powder loading rate than with a spherical powders, as seen in *Table IV. 2*. The low powder loading rate can be a source of problems during the debinding, as the component may collapse because of too large voids created during the debinding and injection steps.

Table IV. 2 Mixing torque obtained during the elaboration of the feedstock composed of binder A with the spherical powder

Powder loading volume (wt. %)	Maximum mixing torque (N.m)	Final mixing torque (N.m)
55	23.8	5.5
58	27.1	7.6
62	29.4	8.7

IV.1.2 Thermal characterization

The thermal characterization was performed on the elbaorated feedstock in order to determine if the quantity of polymer present in the feedstock is corresponding to the one introduced during the mixing and shown in Figure IV. 3. It can also be used to determine the temperature when the polymer part in the feedstock is degraded and help to determine the thermal debinding temperatures. The tests were performed from 20 to 600 °C at a heating rate of 2 °C/min under argon atmosphere. Table IV. 3 shows the maximum weight loss observed for each feedstocks. It appears there is no significant difference between the introduction of the polymer during the mixing and the obtained feedstocks.

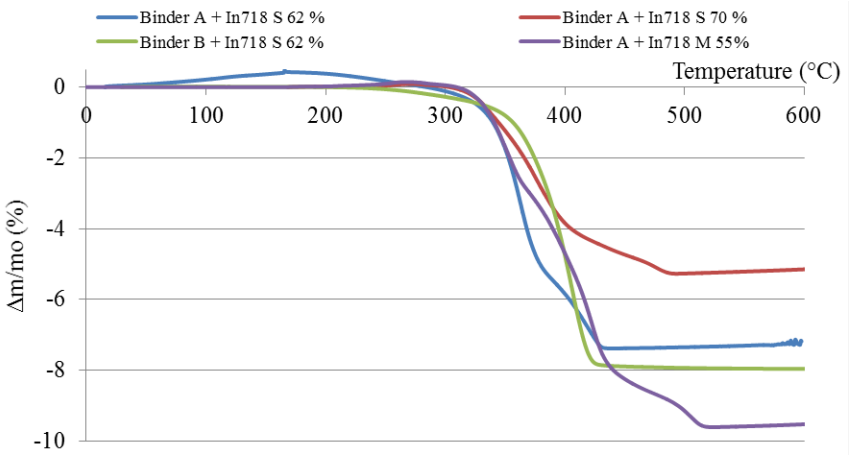

Figure IV. 3 TGA results on the prepared feedstocks from 0 to 600 °C at 2 °C/min in argon atmosphere

Regarding the DSC curves of the feedstocks prepared with binder A and B, a difference of the behaviour of the degradation can be noted. On one hand, it appears that binder A is degraded at two different temperatures, as observed on the TGA curves. On the other hand, the degradation peaks of the CAB and the PEG are displaced for binder B. It seems that the two peaks have merged together, which could be explained by a better interaction between the CAB and the PEG molecular bonds

[10]-[11]. This better compatibility between the two polymers may have an effect on the debinding step of the injected feedstock. In the case of Binder A, a temperature of around 480 °C has to be reached din order to degrade all of the polymer present inside the feedstock instead of around 400 °C for binder B. The thermal debinding temperatures will be adapted with these two values.

Table IV. 3 Weight loss of the feedstocks after TGA from 0 to 600 °C under argon atmosphere

Feedstock	Polymer mass ratio inside the feedstock (wt.) %	Weight loss (%)
Binder A + In718 S 62 %	7.38	7.25
Binder A + In718 S 70 %	5.27	5.19
Binder B + In718 S 62 %	8.35	8.1
Binder A + In718 M 55 %	9.6	9.7

The powder loading volumes of the different feedstocks was decided thanks to the study of the mixing torque. It appears that the binder A can be used with a high powder loading volume without impacting the homogeneity of the feedstock. Thus, two feedstocks were prepared with a powder volume of 62 and 71 (wt.) %. The binder B powder critical volume was less important and only one feedstock was prepared with a powder volume of 62 (wt.) %. The use of the spherical commercial powder allowed a smooth mixing with a low torque rate. The thermal behaviour of the two binders was also investigated and the degradation temperatures found ion the TGA analysis will help during the thermal debinding step.

On the other hand, the mixing of the milled powder was more difficult, with a low powder critical volume and high mixing torque rates. Thus, the chosen powder volume is 55 (wt.) % for the feedstock elaboration. Its thermal behaviour doesn't seem to be impacted as shown on the TGA curves as it is degrading completely at the same temperatures and with the same behaviour. The results of the weight loss are also close to the one expected, meaning that the thermal debinding can be performed with the same parameters. If the component is debinding properly, the carbon residue level inside the component should be of the same level as for the spherical powder.

IV.2 Feedstock injection

IV.2.1 Feedstock rheology

In order to avoid the damage of the tools and the injection equipment, it is important to check the rheological behaviour of the feedstocks. The tests are made with a capillary rheometer at 180 °C and the results are shown in Figure IV. 4. All of the feedstocks have a shear viscosity below 50 Pa.s, which is assumed to be injected into a MIM component. They have a pseudo-plastic behaviour as the shear viscosity is decreasing with the shear rate.

The feedstock composed of the milled powder and the binder A seems to be the one with the highest viscosity, which could be expected from the powder rheology and the mixing rheology. The shear viscosity is also slightly rising with the shear rate, meaning that during the test, there was a packing of the particles inside the channel. It can also be noted, in the case of the feedstock composed of binder A and the spherical powder, that the powder loading has low influence on the shear viscosity as they are far from the critical powder loading rate. However, the binder B presents a gap between the 62 and 71 (wt.) % powder loading rates. The critical powder loading rate of the two binders could explain this difference, as it is reached in the case of binder B.

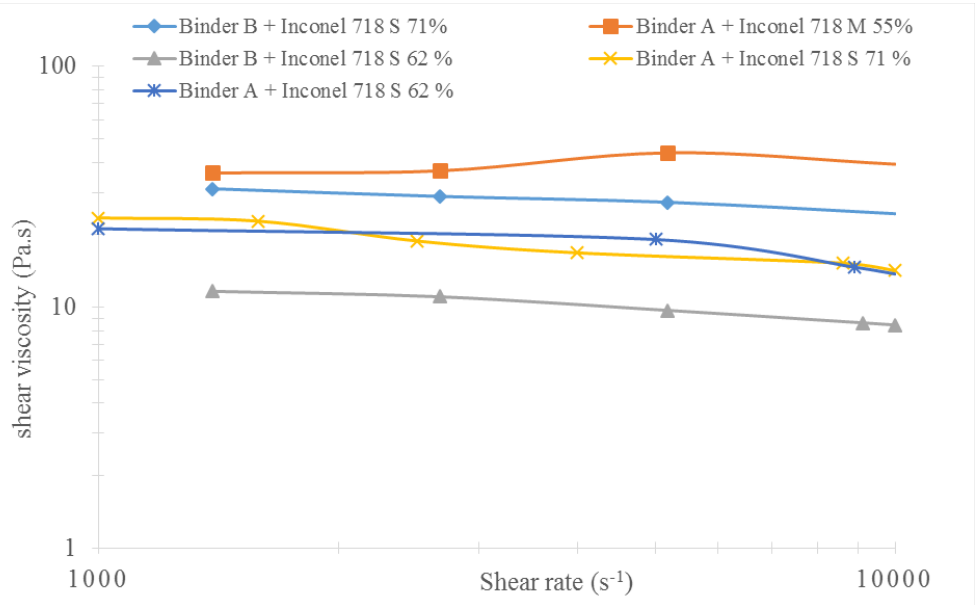

Figure IV. 4 Shear viscosity vs Shear rate of the prepared feedstock at 180 °C with a shear die channel of 1 mm and 16 mm length

IV.2.2 Injection conditions

The injection of the different elaborated feedstocks was performed in order to obtain for each different compositions cylinders of 10 of diameter and 35 mm of height. The feedstock with the binder B was also injected into bars in order to work with larger test specimens. The cylinder geometry was chosen because of the restrictions of the dilatometer and of the FAHP sintering equipment. The bars are used in the conventional, the FAHP and the MW sintering steps.

	Injection temperature (°C)	Injection pressure (MPa)	Injected volume for cylinders (cm^3)	Injected volume for bars (cm^3)
Binder A + In718 S 62 %	175	180	4.8	-
Binder A + In718 S 70 %	175	180	4.5	-
Binder B + In718 S 62 %	160	180	4.8	7.8
Binder A + In718 M 55 %	175	220	5.2	-

The injection parameters were obtained to determine the injection volume. It was first set at a low volume in order to fill partially the mould. Then it was increased until fully filling the cavity of the mould. From this point, the injection pressure and injected volume were optimized. The injected components were weighed until reaching a maximum and reproducible mass, in order to assure the complete filling of the cavity of the mould and limiting the presence of voids inside the components. For each feedstocks, there no particular difficulties to obtain injected components, even in the case of the milled powder, thanks to the low powder loading volume.

IV.2.3 Thermal characterization

The injected components were characterized by TGA from 0 to 600 °C at 2 °C/min under argon atmosphere. The objective was the same as for the feedstock, which is to check the homogeneity between the powder and the binder inside the component and to check if the thermal degradation temperatures are the same as the one observed before the injection. In the case of the cylinder, the surface and the centre of the component were tested. In comparison, there were three tests performed for the bar, at the start to the furthest from the injection point and one in the middle. The results are shown on Figure IV. 5. In the case of the bar, the three tests are almost mixed up, meaning that the feedstock is well injected. In the case of the cylinders, there is a 0.41 % difference of weight loss

between the surface and the centre of the cylinder. That difference could be explained by the absence of temperature control around the mould cavity. As the temperature difference between the mould and the injected feedstock is quite large, the cooling time will be different. Thus, a skin effect is formed around the component [12], which could cause problems during the debinding and sintering steps.

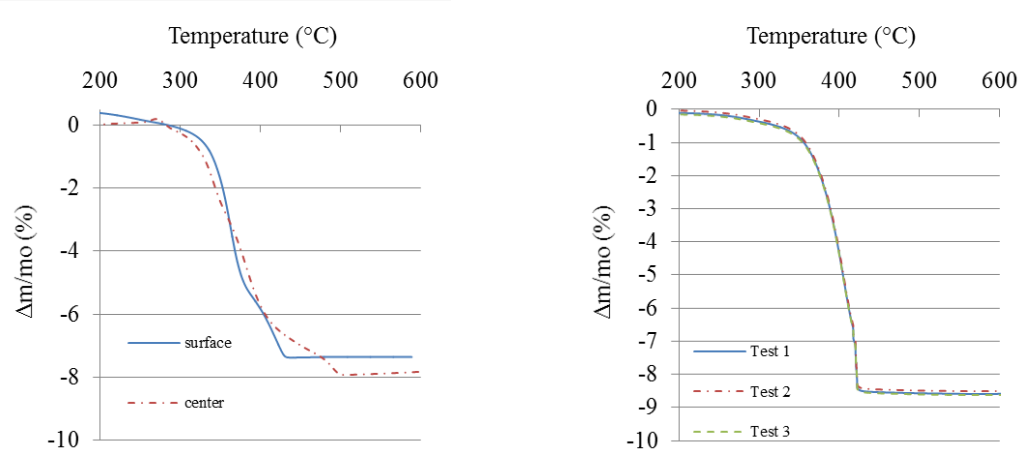

Figure IV. 5 TGA results for the injected components. Left side is the cylinder composed of Binder A + Inconel S 718 62 %, right side is the bar composed of Binder B + Inconel S 718 62 %

IV.3 Solvent and thermal debinding

IV.3.1 Water solvent debinding

The water debinding was performed with deionised water stirred with a magnetic barrel and a fixed temperature during the tests. The tests were performed with the cylinder geometry. The components were immerged at different times and temperatures in order to obtain the fastest debinding rate without damaging the component. The component immerged were dried at 50°C during 12 hours then weighed. The Figure IV. 7 and the Figure IV. 6 shows the results for the debinding of the different injected components in function of the time and the temperature.

The feedstock composed of binder B display a slower debinding rate of the PEG than for binder A. However, they both need at least 72 hours in order to reach the complete removal of the PEG. The feedstock composed of binder A + Inconel 718 M 55 % loses a lot of weight in the early beginning, which could be explained by a much bigger volume of PEG present inside of it.

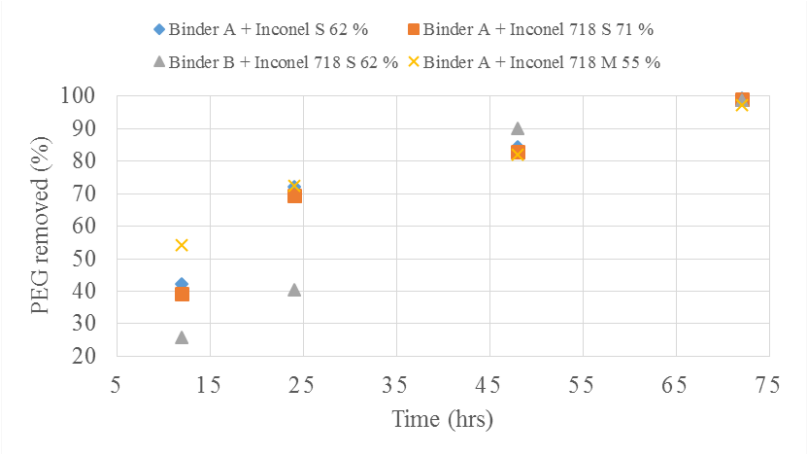

Figure IV. 6 Water debinding of the feedstocks at 30 °C in function of the time

In the case of the binder A + Inconel M 718 55 %, if the temperature is higher than 30 °C, the component loses more weight than the PEG quantity, meaning it loses another component. As the other polymers present in the feedstock are not water soluble, it can be assumed that a bit of powder is taken out of the component. For the three other feedstocks, complete removal of the PEG is not reached as around 2 % of PEG remaining inside the component. Hence, it is necessary to adapt the thermal debinding cycle in order to degrade all of the remaining PEG while avoiding defects of the component.

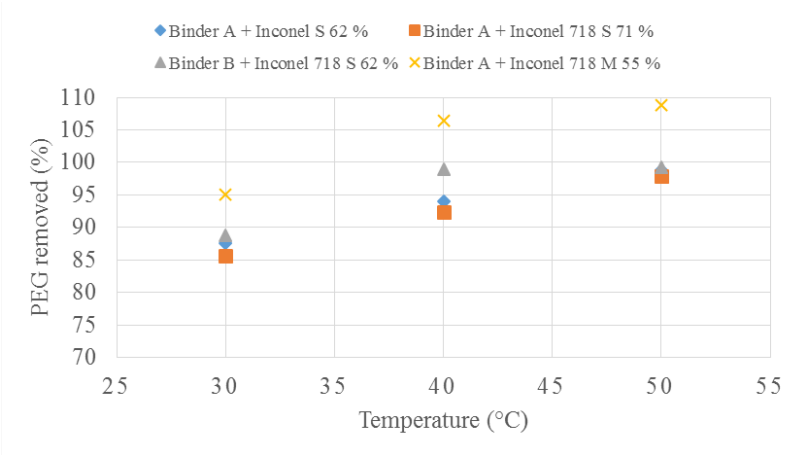

Figure IV. 7 Water debinding of the feedstocks prepared during 72 hours in function of the temperature

IV.3.2 Thermal debinding

The thermal debinding goal is to degrade the CAB and the PP while leaving the less carbon residue as possible. As seen in the polymer characterization part, the CAB degradation temperature is around

the 362 °C and the one of the PP is around 355 °C. In order to assure the complete removal of the binder, the cycle applied was to apply first a temperature of 350 °C during 2 hours then a temperature of 500 °C during 1 hour into argon atmosphere. The debinding rate was set at 1 °C/min in order to avoid the creation of an overpressure inside the component during the degradation of the polymer into a gas. After applying this cycle to the feedstocks, no damage of the components was observed. There was a light shrinkage observed around 150 °C. The shrinkage could be explained by the pressure applied on the component by the sensor, and a small collapse of the component under its own weight once the melting temperature of the component is reached.

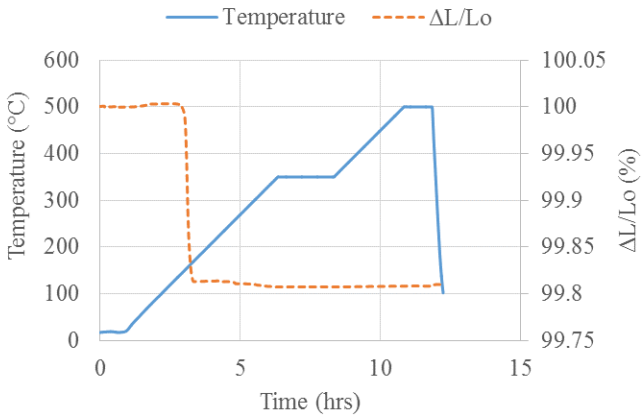

Figure IV. 8 Shrinkage vs time during a debinding cycle from 0 to 600°C at 1 °C /min of binder A +Inconel 718 S 62 %

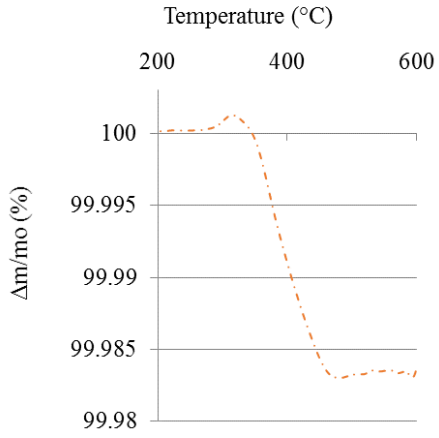

Figure IV. 9 TGA results after performing a thermal debinding cycle on a component binder A +Inconel 718 S 62 %

The Figure IV. 9 shows the results of a TGA analysis performed under argon atmosphere at 5 °C/min on the fully debinded component. It displays a weight loss of around 0.016%. In the paper of Tsuno et al [13], it was found that it needed to have a carbon content of 0.1 (wt.) % inside their Inconel 718 component at the end of MIM process to lower the fatigue life. They concluded that it was only at this level of carbon pollution that the carbides were impacting significantly the γ'' precipitation. In our case, the level of carbon content found in the component should not impact the microstructure and the mechanical performances.

IV.4 Sintering of the MIM components

IV.4.1 Optimization of the sintering parameters

As seen in the literature [14], the sintering parameters of Inconel 718 have to be optimized in order to promote the γ'' phase. Moreover, in the case of the MIM process, it is also dependent of the selected feedstock and its powder loading. Hence, the sintering cycle parameters such as the heating rate, the dwell time and temperature need to be investigated in order to obtain the reference characteristics of our material. In order to obtain them, different dilatometry tests were performed on the component injected with the feedstock binder A + Inconel 718 71 % after the thermal debinding. They were all performed with a heating rate of 5 °C/min and a cooling down of 20 °C/min by following the criteria of Valencia et al [15]. The two parameters needing to be optimized are the sintering temperature and the dwell time in order to obtain the lowest porosity while having a homogeneous microstructure. The shrinkage measured during dilatometry tests will show when the components complete the sintering mechanism and filling the porosity created during the debinding. The homogeneity of the hardness measurements also indicates if the microstructure is homogeneous.

The Figure IV. 10 shows the evolution of the shrinkage of the MIM cylinder after the application of a sintering cycle at different temperature maintained during 2 hours. It can be observed that once the 1200 °C is reached, the variation of length of the sample drops fast. This result confirms the melting temperature advanced by Knovorosky et al [16] The best shrinkage was obtained when the sample was sintered at 1290 °C. The sensor during the dilatometry test at 1300 °C deformed the sample, thus it was decided that 1290 °C was the highest temperature that can be used for the sintering cycle.

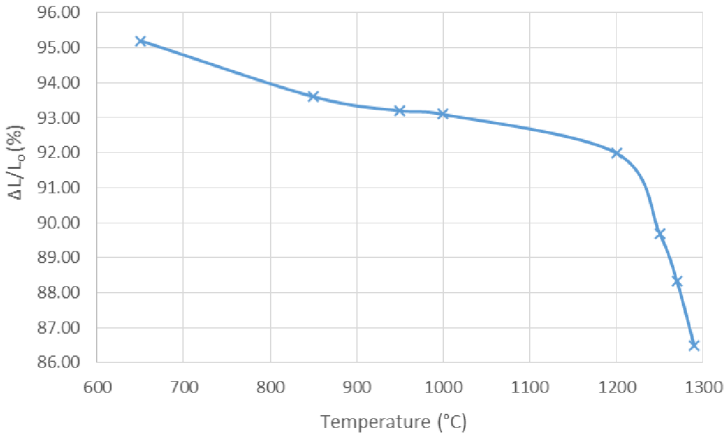

Figure IV. 10 Maximum shrinkage vs temperature after sintering of binder A+ Inconel 718 S 71 % at different temperatures during 2 hours under argon atmosphere

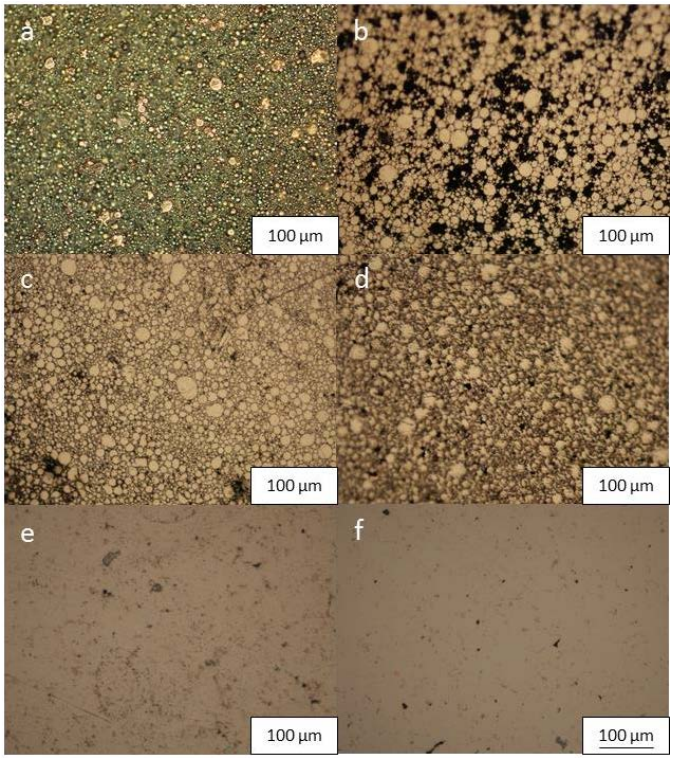

Figure IV. 11 OM images of the sintered component binder A + Inconel 718 S 71 % at (a) 850 °C, (b) 1000 °C, (c) 1200 °C, (d) 1250 °C, (e) 1275 °C, (f) 1290 °C during 4 hours

The Table IV. 4 resumes the evolution of the microstructure of the components with the evolution of the sintering temperature. At 850 °C, the powder just starts to show signs of grain coarsening. Once the component reached 1000°C, the coarsening of the grains brought a rearrangement of the material, as a lot of porosity can be observed. At 1200 °C, bigger grains can be observed with a lowering of the porosity level, and at 1250 °C, a matrix can be observed around the grains because of the liquid

phase being formed at this temperature. Between 1275 and 1290 °C, a metallic microstructure is formed with a low level of porosity. From the density and the hardness measured presented in Table IV. 4, it is possible to obtain the best performances by using 1290 °C as sintering temperature.

Table IV. 4 Density and hardness obtained at different sintering temperature for binder A + Inconel 718 S 71 %

Sintering temperature	Density (%)	Hardness (1.0 HV)
1000	78.2 ± 2.8	98.3 ± 25.3
1200	81.5 ± 1.3	106 ± 8.6
1250	85.3 ± 1.2	155 ± 4.3
1275	96.8 ± 0.8	206 ± 5.5
1290	97.8 ± 1.2	212 ± 3.2

The Figure IV. 12 shows the dilatometry curves of sintering cycles performed at different dwell times at a heating rate of 5 °C/min and a cooling rate of 20 °C/min. From the three tests, the shrinkage is increased from 85.9 % of the height of the cylinder to 84.9 % by sintering with two supplementary hours and is not progressing anymore if the dwell time is increased again.

Figure IV. 12 Dilatometry curves performed on Binder A+ Inconel 718 S 71 % at 1290 °C maintained at different times under argon atmosphere

IV.4.2 Application to all of the feedstocks

The sintering cycle of 1290 °C maintained during 4 hours was applied to the other injected feedstocks (Figure IV. 13). The shrinkage is increased by around 6 % between the 62 and 71 % powder loading rate for the components injected with the binder A. The difference in shrinkage comes

from the powder which occupies a lower volume and during the grain coarsening, a bigger porosity network need to be suppressed.

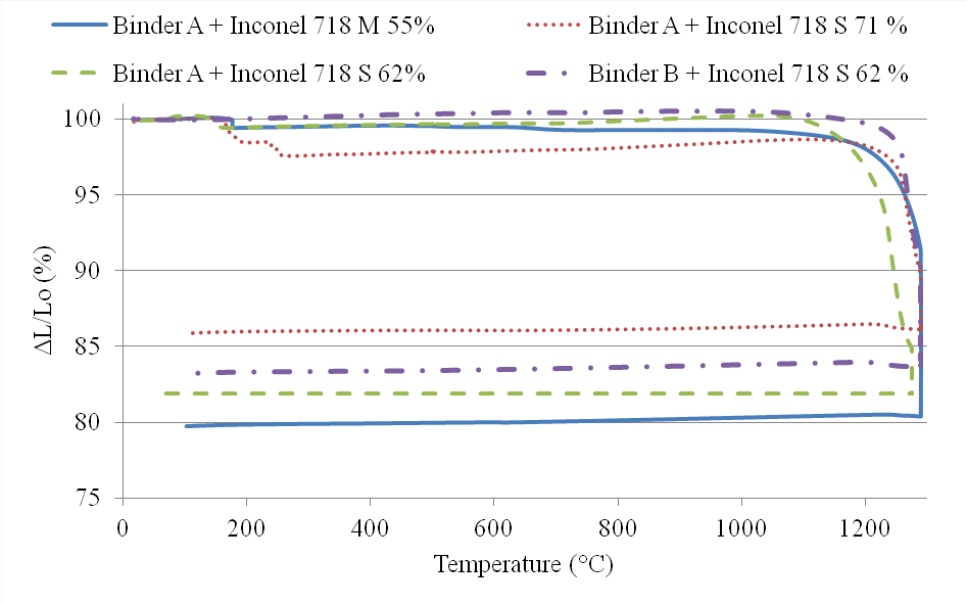

Figure IV. 13 Dilatometry curves performed on the injected components at1290 °C for 2 hours and 5 °C/min under argon atmosphere

The density obtained with 62 (wt.) % is of 95.2 % while it reached 99.3 % with 71 (wt.) %. This level of porosity did not impact the hardness measurements, meaning that the microstructure are similar. The difference of density between the two components is explained by cavities formed during sintering close to the surface of the sample as shown on Figure IV. 14. A higher powder loading rate seems to reduce the risks of this defect to happen.

In the case of the component sintered with the feedstock binder B + Inconel 718 S 62 %, the properties obtained are close to the one obtained with binder A. The microstructure also presents no difference with the binder A + Inconel 718 S 71%. The two binders give dense components with a homogeneous microstructure and confirms the feedstock elaboration and the debinding parameters.

Finally, the sintering of the milled powder shows good results compared to the difficulties seen during the mixing of the feedstock. The low powder loading content did not impact the microstructure as for the spherical powder as the organization of the particles inside the component is different. It is supposed that during the injection, a difference of orientation of the particles is happening between the outer surface and the centre of the component [17]

Table IV. 5 Density and hardness obtained for the different feedstock sintered at1290 °C for 2 hours and 5 °C/min under argon atmosphere

Feedstock	Density (%)	Hardness (1.0 HV)
Binder A + Inconel 718 S 62 %	95.2 ± 0.3	229 ± 8
Binder A + Inconel 718 S 71 %	99.3 ± 0.1	245 ± 7
Binder B + Inconel 718 S 62 %	98.8 ± 0.1	237 ± 3
Binder A + Inconel 718 M 55 %	97.3 ± 0.4	233 ± 9

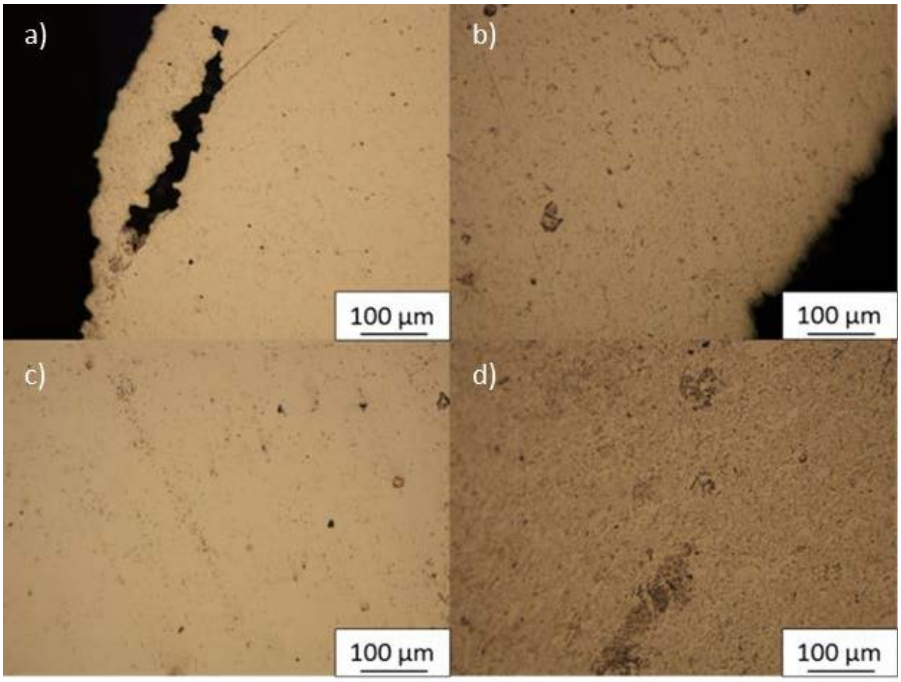

Figure IV. 14 OM image of sintered component of a) binder A + Inconel 718 S 62 %, b) binder A + Inconel 718 S 71 %, c) binder B + Inconel 718 S 62 %, d) binder A + Inconel 718 M 55 %

IV.4.3 MIM component characterization

The Figure IV. 15 shows SEM images taken after sintering of the milled powder. The microstructure obtained with the milled powder does not show signs of porosity between the grains, however, some cracks can be seen, which may appear in case of a too long milling time. The EDX analysis made on zone 1 indicates the presence of carbon and titanium inside the microstructure

indicating the formation of carbides. Zone 2 is composed with most of the elements of the Inconel 718 in the same ratio at the exception of the molybdenum. As the microstructure is not composed of spherical particle, the grain size was obtained by using the method of the equivalent spherical diameter. The mean grain size measured is of 12.35 ± 7.75 µm.

The microstructure of the sintered component composed of the spherical powder shows the same kind of porosity observed on the OM images. Two phases can be observed on the image. The EDX performed on zone 3 shows the presence of nitrogen and a high level of titanium, which indicates the formation of titanium nitride. These may appear during all of the manipulation of the powder from the mixing to the debinding. The zone 4 is the same as zone 2, displaying the same ratio of chemical elements as the initial powder. There is also the presence of molybdenum that was not observed in the case of the milled powder, meaning that during the milling, a part of this element may have been lost during the process. The mean grain size measured is of 6.01 ± 5.52 µm.

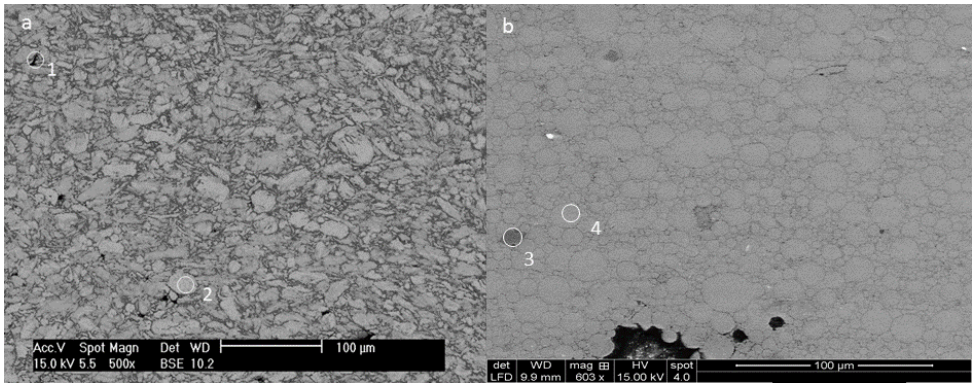

Figure IV. 15 SEM images of the furnace sintered at 1290 °C during 4 hours after electro-polishing of (a) binder A + Inconel 718 M 55 % and (b) binder A + Inconel 718 S 62 %

Table IV. 6 EDX analysis of the zones marked on Figure IV. 15

Element (wt.) %	Zone 1	Zone 2	Zone 3	Zone 4
C K	5.3	0.69	-	0.2
N K	-		18.23	-
Al K	-	0.71	-	-
Nb L	1.36	5.74	14.12	3.86
Mo L	-	-	-	3.12
Ti K	58.01	1.31	55.98	-
Cr K	-	19.43	-	15.21
Fe K	10.0.1	18.91	1.56	18.51
Ni K	35.33	53.21	10.11	59.1

The tensile strength tests was performed at room temperature on the component binder A + Inconel 718 71 % as it has the best results in terms of density and hardness (Figure IV. 16). The sample shows a yield stress (YS) of 465.4 MPa and an ultimate stress of 817 MPa. These results can be compared with the properties obtained by Özgun et al [1], the difference being a higher elongation. However, these results are inferior compared to the results of Valencia et al [2] and of Slama et al [18], obtained after the application of a thermal treatment.

Table IV. 7 Mechanical properties obtained from the tensile strength test of the sintered component binder A + Inconel 718 S 71 %

YS (MPa)	E (GPa)	UTS (MPa)	Elongation (%)
465.4 ± 13.7	63 .38 ± 3.78	817 ± 14	31.5

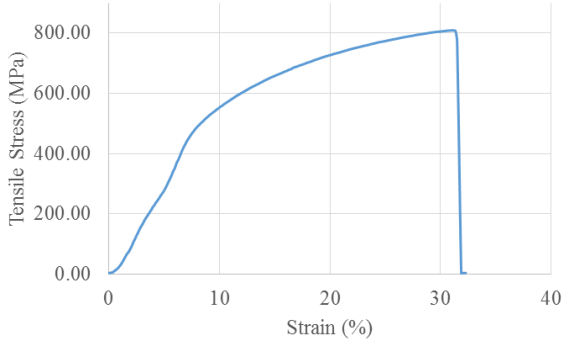

Figure IV. 16 Tensile strength test of the sintered component binder A + Inconel 718 S 71 %

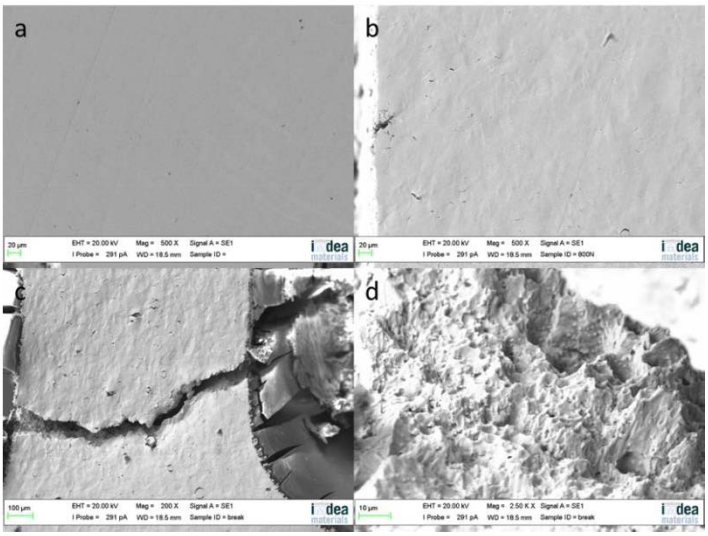

Figure IV. 17 SEM images obtained during an in-situ tensile strength test at (a) 0 MPa, (b) 800 MPa (c) breaking point and (d) is the rupture profile of the broken sample

An in-situ tensile strength test was also performed on the component (Figure IV. 17). There were no cracks on the sample until reaching a strain of 400 MPa. As can be seen at 800 MPa, a crack start to appear in the border of the specimen, very near to the fracture strength. Fracture takes place very fast and in a brittle manner. Despite we are in front of a brittle failure, in the fracture surface can be seen dimples produced by micro void coalescence [19]-[20]. In sintered alloys is quite usual to find ductile micro mechanisms when the macro behaviour is brittle.

IV.4.4 Thermal treatment of MIM sintered component

The results obtained after sintering at 1290 °C during 4 hours have shown results below the conventional standards for superalloys, hence a thermal treatment was applied to a sintered component. The applied cycle was following the treatment described in part II.1.4. A temperature of 720 °C was applied followed by a temperature of 620 °C during 8 hours each. The obtained hardness is 341 ± 19 HV and a grain size of 20.75 ± 9.2 µm. The hardness is closer to the one measured by Özgun et al [1] or Miura et al [21] which were respectively at 348 HV and 330 HV The thermal treatment induces an increase of the grain size by 3.45 times more compared to the sintered components. The Figure IV. 18 shows a SEM image of the obtained microstructure. Inside of the sintered particles, two phases seems to have appeared. The Table IV. 8 resumes the EDX analysis of the 4 marked zones. There is still a presence of carbides at the grain joints in zone 2. The zone 3 displays the same elements as the initial powder corresponding to the γ matrix. The zone 1 is mostly composed of chromium and zone 4 is rich in niobium. These two phases can be assimilated to the increase of the γ'' phase. These phases are also homogeneously distributed inside the grains.

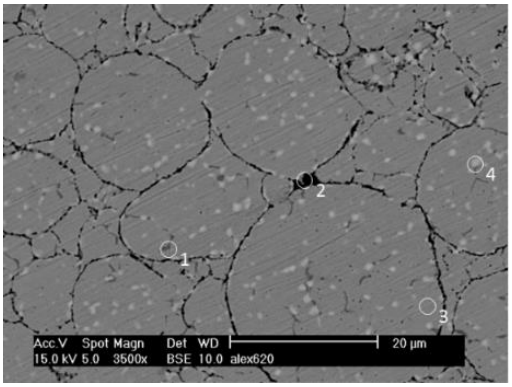

Figure IV. 18 SEM image of sintered component binder A + Inconel 718 S 62 % after thermal treatment at 720 and 620 °C during 8 hours each

Table IV. 8 EDX analysis of the zones marked on Figure IV. 18

Element (wt.) %	Zone 1	Zone 2	Zone 3	Zone 4
C K	-	9,36	-	-
Al K	-	7,8	-	-
Nb L	4,28	16,34	2,49	19,38
Ti K	0,49	3,69	0,52	2,72
Cr K	42,75	19,87	19,05	15,55
Fe K	13,31	10,88	18,5	14,44
Ni K	39,18	32,05	59,44	47,9

IV.5 Partial remarks

In this chapter, four feedstocks were prepared with binder A and binder B and two different powder morphologies. The critical powder loading rate was identified thanks to the incremental method. In the case of the spherical powder, the critical powder loading rate for the binder A is quite high, hence two feedstocks were prepared with a rate of 62 (wt.) % in volume and of 71 (wt.) % . The first one is commonly used by industrials and feedstocks providers. However the capillary rheology shown that there is not a big difference in terms of shear viscosity under shear stress. The critical powder loading rate for binder B was smaller, thus only one a rate of 62 (wt.) % was chosen. Finally, in the case of the milled powder, the binder A was used and feedstock with a 55 (wt.) % powder loading rate, because of the high torque force needed to mix the feedstock.

As the rheology shown that the four feedstocks satisfies a shear viscosity small enough for the injection process, they were all injected into cylinders and bars. The optimization of the injection parameters has assured the homogeneity of the rate powder/binder. It was also confirmed by TGA of the components at different zones of the components. The cylinders, as the mould temperature was not thermally controlled, having a small difference between the surface and the centre of the sample.

The solvent debinding, by immerging the components into water, takes 72 hours in order to reach a satisfying PEG removal rate. It is an obligation to respect this time in order to apply without problems the thermal debinding treatment. The thermal debinding is applied at the degradation temperatures of the CAB and the PP during 2 hours and at 500 °C in order to remove completely the binder. The carbon content inside the components is low enough to avoid the formation of too much

carbides. The solvent and thermal debinding can be applied to all of the elaborated feedstocks without damaging the components.

The fully debinded components have then to undergo the furnace sintering cycle. The parameters of the cycle were optimized and applied to all the feedstocks. The components obtained with feedstock binder A + Inconel 718 S have shown a different porosity level of the bulk components. It seems that a higher powder loading rate is reducing the apparition of defects at the surface of the material during the sintering. Finally, in the sintered components were not obtained the desired properties for the project, thus a thermal treatment was applied to a sintered component. The microstructure is clearly optimized, as the γ'' phases are promoted inside the grains.

At the end of the optimization of the MIM process, the components obtained displays results expected by the industry for this material. The Figure IV. 19 shows the time repartition of the different steps that were presented in this chapter. The solvent debinding is taking a lot of time to be completed, taking almost two third of the total processing time. The next chapter introduces a new debinding method in order to reduce this parameter.

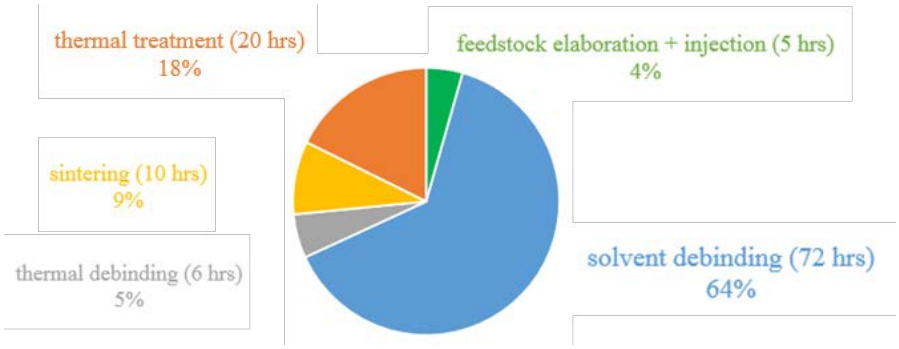

Figure IV. 19 Time repartition of the conventional MIM process

REFERENCES

[1] Ö. Özgün, H. Ö. Gülsoy, R. Yılmaz, Et F. Fındık, « Microstructural And Mechanical Characterization Of Injection Molded 718 Superalloy Powders », *J. Alloys Compd.*, Vol. 576, P. 140‑153, Nov. 2013.

[2] J. J. Valencia, « Sintering Effect On The Microstructure And Mechanical Properties Of Alloy 718 Processed By Powder Injection Molding », *Miner. Met. Mater. Soc.*, Vol. Superalloys 718,625,706 And Various Derivatives, 1997.

[3] B. Hausnerová, L. Marcaníková, P. Filip, Et P. Sáha, « Rheological Characterization Of Powder Injection Moulding Using Feedstock Based On Aluminium Oxide And Multicomponent Water-Soluble Polymer Binder », *Proc. Recent Adv. Fluid Mech. Heat Mass Transf.*, P. 245–250, 2011.

[4] P. J. Vervoort, R. Vetter, Et J. Duszczyk, « Overview Of Powder Injection Molding », *Adv. Perform. Mater.*, Vol. 3, Nº 2, P. 121–151, 1996.

[5] A. Royer, « Etude, Caractérisations Et Développement De Mélanges De Polymères Biosourcés Chargés De Poudre D'inconel 718 Pour L'élaboration De Composants Et Micro-Composants Via Moulage Par Injection De Poudres Métalliques », 2016.

[6] F. M. Barreiros Et M. T. Vieira, « Pim Of Non-Conventional Particles », *Ceram. Int.*, Vol. 32, Nº 3, P. 297‑302, Janv. 2006.

[7] J. Hidalgo, A. Jiménez-Morales, Et J. M. Torralba, « Torque Rheology Of Zircon Feedstocks For Powder Injection Moulding », *J. Eur. Ceram. Soc.*, Vol. 32, Nº 16, P. 4063‑4072, Déc. 2012.

[8] B. Berginc, Z. Kampus, Et B. Sustarsic, « Influence Of Feedstock Characteristics And Process Parameters On Properties Of Mim Parts Made Of 316l », *Powder Metall.*, Vol. 50, Nº 2, P. 172‑183, Juin 2007.

[9] S. K. Samanta, H. Chattopadhyay, Et M. M. Godkhindi, « Thermo-Physical Characterization Of Binder And Feedstock For Single And Multiphase Flow Of Pim 316l Feedstock », *J. Mater. Process. Technol.*, Vol. 211, Nº 12, P. 2114‑2122, Déc. 2011.

[10] A. Royer, T. Barriere, Et J. C. Gelin, « The Degradation Of Poly(Ethylene Glycol) In An Inconel 718 Feedstock In The Metal Injection Moulding Process », *Powder Technol.*, Vol. 284, P. 467‑474, Nov. 2015.

[11] J. Hidalgo Garcia, « Development Of Binder Systems Based On Cab For Powder Injection Moulding (Pim) And Micro Powder Injection Moulding (µ-Pim) Of Zircon And Invar Powders », 2014.

[12] T. S. Shivashankar, R. K. Enneti, S.-J. Park, R. M. German, Et S. V. Atre, « The Effects Of Material Attributes On Powder–Binder Separation Phenomena In Powder Injection Molding », *Powder Technol.*, Vol. 243, P. 79‑84, Juillet 2013.

[13] N. Tsuno, T. Yoshinouchi, S. Ikeda, Et H. Yoshizawa, « The Effect Of Carbon Content On High Cycle Fatigue Behavior Of Metal Injection Molded 718 Superalloys », *8th Int. Symp. Superalloy 718 Deriv. 2014*, P. 751‑755, Déc. 2014.

[14] J. W. Brooks Et P. J. Bridges, « Metallurgical Stability Of Inconel Alloy 718 In S. Reichman Et Al. (Eds.), Superalloys 1988, Tms, Warrendale, Pa », P. 33‑42, 1988.

[15] J. J. Valencia, T. Mccabe, K. Hens, J. O. Hansen, Et A. Bose, « Microstructure And Mechanical Properties Of Inconel 625 And 718 Alloys Processed By Powder Injection Molding », *Superalloys 718,625,706 And Various Derivatives*, P. 935‑945, 1994.

[16] G. A. Knorovsky, M. J. Cieslak, T. J. Headley, A. D. Romig, Et W. F. Hammetter, « Inconel 718: A Solidification Diagram », *Metall. Trans. A*, Vol. 20, Nº 10, P. 2149–2158, 1989.
[17] A. Mannschatz, A. Müller, Et T. Moritz, « Influence Of Powder Morphology On Properties Of Ceramic Injection Moulding Feedstocks », *J. Eur. Ceram. Soc.*, Vol. 31, Nº 14, P. 2551‑2558, Nov. 2011.
[18] C. Slama Et G. Cizeron, « Étude Du Comportement Structural De L'alliage Nc 19 Fe Nb (Inconel 718) », *J. Phys. Iii*, Vol. 7, Nº 3, P. 24, 1997.
[19] N. Candela, F. Velasco, Et J. M. Torralba, « Fracture Mechanisms In Sintered Steels With 3.5%(Wt.) Mo », *Mater. Sci. Eng. A*, Vol. 259, Nº 1, P. 98‑104, Janv. 1999.
[20] J. M. Torralba, L. Esteban, E. Bernardo, Et M. Campos, « Understanding Contribution Of Microstructure To Fracture Behaviour Of Sintered Steels », *Powder Metall.*, Vol. 57, Nº 5, P. 357‑364, Déc. 2014.
[21] H. Miura, H. Ikeda, T. Iwahashi, Et T. Osada, « High Temperature And Fatigue Properties Of Injection Moulded Superalloy Compacts », *Pim Int.*, Nº 4, P. 68‑70, 2010.

V EXTRACTION OF PEG FROM INCONEL 718 MIM SAMPLE BY SUPERCRITICAL STATE CO_2

In accordance with the conclusions of the previous chapter, the developed binders with PEG, during water debinding, the time needed to obtain its complete extraction is 72 hours. The use of water as solvent is an answer to the replacement of the organic solvents during debinding to the detriment of the debinding speed rate. The debinding rate may be improved by adding an organic solvent to the water[1]. However, it brings the question about the treatment of the debinding water used in the debinding process containing feedstock residues and the organic solvent. With the evolution of the environmental regulations, a treatment of the water may be needed in order to get rid of the polymer residue. The supercritical fluid state, and particularly the CO_2, is used by industry to perform extraction of organic elements like perfumes and aroma [2] or for cleaning mechanical parts [3]. This method represents an environmentally safe alternative and was recently developed to perform binder extraction for MIM components [4].

As it was mentioned in the introduction, the supercritical state is obtained at the triple point of the phase diagram. The CO_2 density and viscosity is dependent of the temperature and the pressure, helping the diffusion of the fluid inside of the organic binder. Hence, the first part of this work will optimize the pressure and the temperature of the CO_2 in order to reach the best debinding rate without damaging the components. Once these parameters are found, the rates and time of the debinding cycle will be developed in order to eliminate as much as possible in the smaller time the PEG inside of the components. It is also important to consider that the debinding method is selective, thus some tests must be performed in order to identify if the method reacts only with the PEG and if there is no influence of the method on the rest of the binder. The performance of the binder extraction from the sample will be determined by mass difference weighing before and after treatment and by using TGA.

The components will undergo high pressure of at least 7.5 MPa at a temperature that could go from 30 °C to higher temperatures. These conditions may be difficult for the shape of the components and the powder/binder repartition obtained during the injection moulding step. In order to confirm if the method can replace the solvent debinding, the effect of the method on the structural integrity of the component will be observed by roughness observation and optical microscopy.

The supercritical debinding was performed only on binder A injected into cylinders of 10 mm of diameter and a height of 20 mm. After the first tests was performed with the binder B, there were no

components that kept their shape. There could be two explanations to the failure of binder B. The first one is the possibility of a reaction between the CAB and the CO_2 in a supercritical state. This is may be due to the fact that CAB is possessing hydroxyl groups which are weak against strong oxidants. The second possibility is the fast debinding of the structure of the component obtained during the injection. The CAB is sometime associated to another strong backbone polymer such as PMMA in order to avoid this kind of problems [5].

V.1 Supercritical fluid debinding process

V.1.1 Supercritical fluid debinding equipment

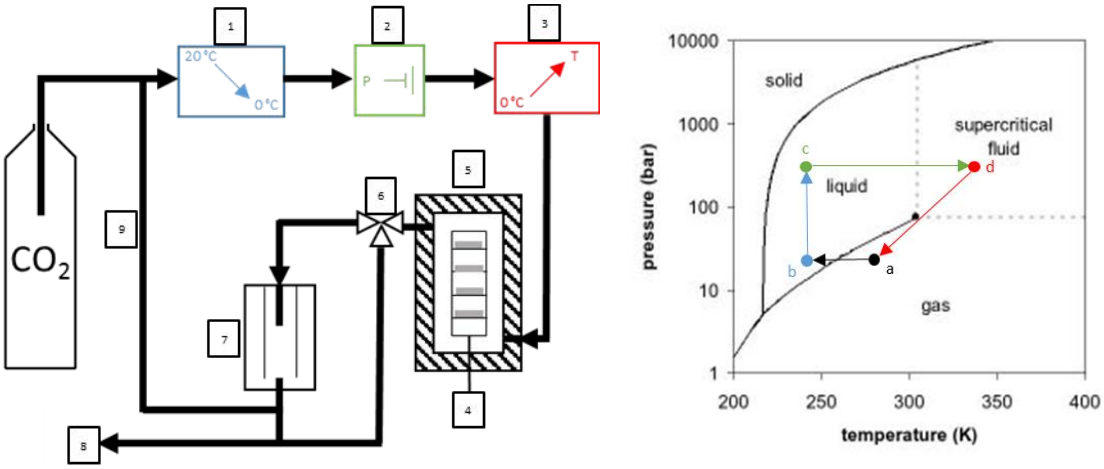

Figure V. 1 Description of the equipment and CO_2 diagram phase

The supercritical fluid debinding was performed on an equipment developed by Separex. It is composed of different parts described in Figure V. 1. All the tests were performed with this configuration. First, the CO_2 is in a gaseous state (a) at room temperature and a pressure of around 5-6 MPa. It is introduced into a cooling system (1) in order to reach a liquid state (b). In this state, it is easier to apply a high level of pressure than when CO_2 is in a gaseous state. The pressure is applied with a high performance pump (2). Then the CO_2 is heated inside a thermal exchanger (3) in order to reach the supercritical state (d). It is introduced into a reactor (5) devised to resist until 75 MPa and maintained at the testing temperature. Inside of the reactor there is a support holding the MIM components (4). The pressure inside the reactor is regulated with a manometer (6) that sends the excess of CO_2 into an extractor that separate the extracted polymer from the CO_2. The exit of the reactor is linked to a recycling line (9) where the CO_2 is refrigerated and reinjected towards the

cooling system for a new complete cycle, reducing the volume of CO_2 used during the experiment. At the end of a test, the system is purged to an evacuation line (8).

V.1.2 Supercritical fluid debinding tests methodology

The supercritical fluid debinding tests depend on the pressure, the temperature, the holding time and the rates of pressure rise and decrease. These parameters can be defined in a programmed cycle of the controlling software of the equipment. In the case of the rate of pressure rate, it was advised to use by Separex a constant rate of 1 MPa/min until the desired pressure. During the decrease of pressure, it is important to take into account the change of state from a supercritical into gas state with a change of density. In order to avoid damaging the components the decrease of the pressure is separated in two rates, one of 2 MPa/min until 9 MPa and one of 1 MPa/min until the end of the test. The temperature of the system is maintained during all of the test until the end of the holding time.

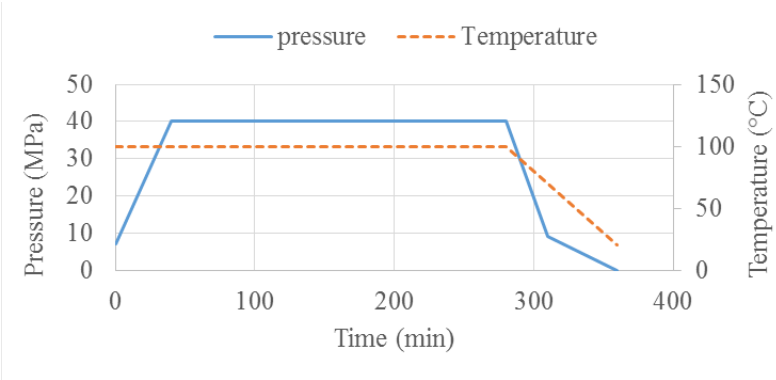

Figure V. 2 Example of the evolution of the pressure and the temperature vs time during the tests

The MIM components are weighed and measured before each test. In order to assume that there is only polymer extracted from the components and not the powder, TGA are also performed at the surface and the centre of the component. Some of the components are also tested with a roughness probe and with optical microscopy in order to observe the effect on the surface of the components. Once the optimal parameters are found, the component will be thermally debinded and sintered in the same conditions as shown in part IV, in order to analyse the effect of the new debinding method on the microstructure.

V.1.3 Selectivity of the CO_2 in supercritical state

Before starting the tests on the MIM components, it is important to assure the selectivity of the method because only the PEG can be affected by the method and not the other polymers that are present inside the binder. Hence, injected components were made with binder A with a bar geometry of 60 mm length, 10 mm width and 3 mm thickness. The supercritical fluid debinding test was performed at 40 MPa and 150 °C during 2 hours.

The obtained component was then tested with infra-red (IR) spectroscopy using the Fourier transform. This method is based on the absorption of the IR light by the material. Depending on the chemical bond of the material and of the wavelength, the material will answer by absorbing the energy of the light and this difference of energy is observed on the transmitted light. The material will be exposed to different wavelength, from 500 to 4000 cm^{-1} and a detector will register the transmitted light. The information that can be obtained from this test is first qualitative as the spectrum is specific to the chemical bond. By using identification tables, it is possible to attribute them to a specific chemical bond. Secondly, it is quantitative, as the intensity of the absorption is dependent on the chemical bond if the concentration of the chemical bond is high inside the material, a higher absorbance will be observed.

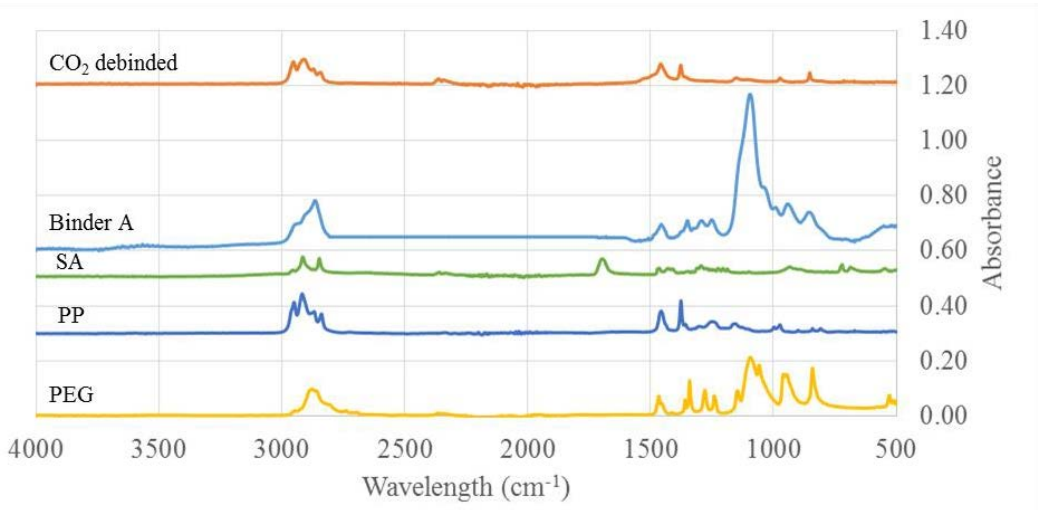

Figure V. 3 IR spectrum of each elements of Binder A, after injection and CO_2 in supercritical state debinding

The Figure V. 3 shows the IR spectrum of the 3 polymers composing the binder A, the injected component and the supercritical fluid debinded. The PP and PEG spectrum can be identified inside the injected component. The SA is present in a small ratio in the composition of the binder A. This

could explain that it is not present in the binder spectrum. After the supercritical debinding cycle, there are no more signs of the presence of the PEG. Moreover, only the PP spectrum can be identified, meaning that all of the PEG was extracted and that there were no degradation of the PP on the level of the chemical bonds. The CO_2 in the supercritical state is only interacting with the PEG and leave the other polymers as required for completing a good debinding.

V.2 Optimization of the supercritical fluid debinding cycle

The Figure V. 4 shows the results obtained during the optimization of the parameters. They were optimized one at a time with the binder A + Inconel 718 S 62 %. The pressure was searched with a temperature of 50 °C. This temperature was chosen as it is at the beginning of the supercritical state of the CO_2 and it is under the melting temperature of the binder. It appears that a pressure of 40 MPa gives the best results at 50 °C but the quantity of PEG removed from the components is under the 40 %. It can also be noticed that if the pressure is increased, the quantity of PEG removed decreases. Hence the temperature optimization is performed at 40 MPa. The evolution of the PEG removal as a function of the temperature did not show a lot of improvement until a temperature of 150 °C was reached. At this temperature, from the weight measurement, most of the PEG was removed from the component. It seems that a temperature close to the melting temperature of the binder needs to be reached in order to obtain the best debinding rate. Similar results were also obtained with paraffin wax [6], [7].

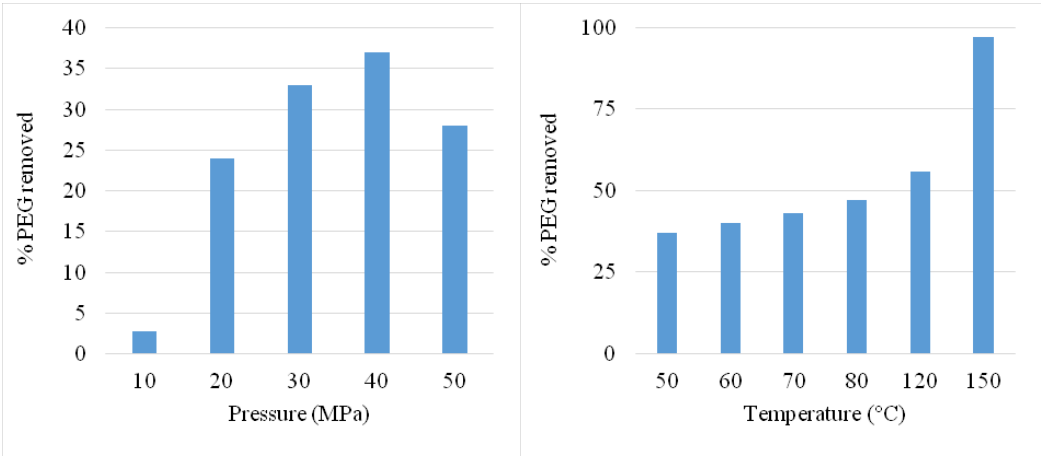

Figure V. 4 Quantity of PEG removed vs pressure at 50 °C and vs temperature at 50 MPa, both during 4 hrs after supercritical fluid debinding of binder A + Inconel 718 S 62 %

The previous tests were performed for 4 hours but the duration of the tests was arbitrarily chosen. Hence, the debinding time was tested from 1 hour to 5 hours, on the 3 feedstocks composed with binder A. The Figure V. 5 shows the results of the time optimization. In the case of the binder A + Inconel 718 S 62%, it appears that 4 hours was the needed time to obtain the complete removal of the PEG. However, it was not obtained with a higher powder loading rate of 71 %. It was necessary to increase the debinding time.

In the case of solvent debinding, Lin et al. [8] and other groups [9], [10] developed numerical models on a diffusion mechanism. Those models were based on a diffusion going from the exterior to the centre of the component in a unidirectional way at a constant rate. The starting condition is the initial concentration of the polymer. They all show that the higher is the polymer concentration, the higher is the extraction time. Thus, it seems that the diffusion mechanism of a supercritical fluid depending, for this binder, works the same way as for the solvent debinding. Chartier et al [11] also used this model for numerical simulation on supercritical debinding and obtained similar results between the numerical data and their experimental results. The tests performed on binder A + Inconel 718 M 55% did not completely remove all of the PEG, as 5 % still remained inside the component. The shape of the powder has an effect on the extraction of the polymer and these parameters may not be the best for this feedstock.

Figure V. 5 Quantity of PEG removed vs pressure at 50 °C and vs temperature at 50 MPa, both during 4 hrs after supercritical fluid debinding of binder A + Inconel 718 S 62 %

In order to obtain better results for the milled powder, different pressures were again tested, but this time at 150 °C. The Figure V. 6 shows the results obtained with both powders. If the pressure is

decreased, the quantity of PEG removed follows the same behaviour as it was seen during the previous pressure optimization. The complete removal of the PEG was obtained at 50 MPa with the milled powder. However, in case of the spherical powder, reached 100 % of PEG weight loss.

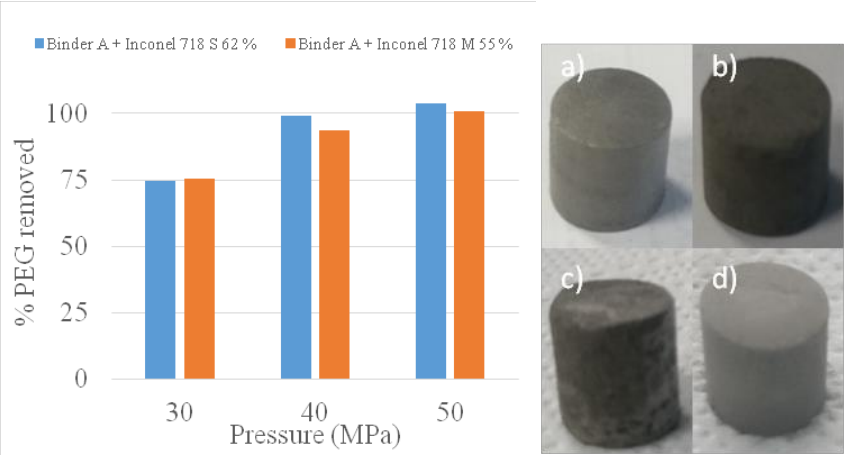

Figure V. 6 Quantity of PEG removed in function of the pressure at 150 °C after supercritical fluid debinding of binder A + Inconel 718 S 62 % (image a) before and c) after debinding) and binder A + Inconel 718 M 55 % (image b) before and d) after debinding)

The pictures of the components before and after debinding are also shown in Figure V. 6. At 50 MPa, the component binder A + Inconel 718 62% is damaged as opposed to the Inconel 718 M 55 % component. In conclusion, in the case of spherical powder, if the pressure is too high for the component, the method damages it. In the case of a flake shape powder, the debinding rate is highly influenced and it is more difficult to reach the PEG inside the component.

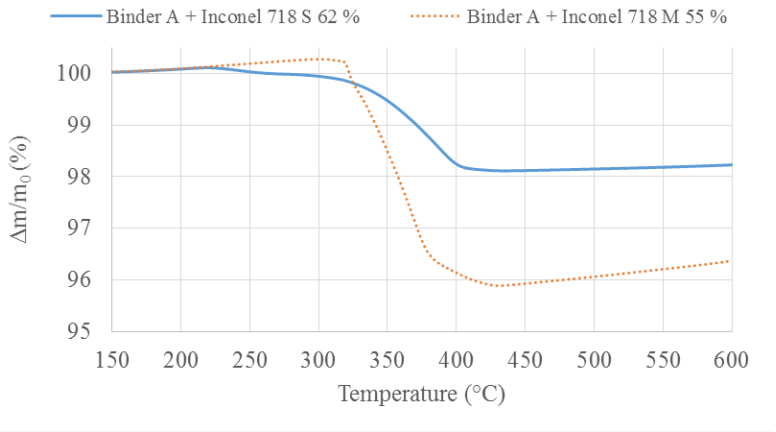

Figure V. 7 TGA curves under argon atmosphere and 5 °C/min of the components after supercritical fluid at the optimized conditions

The Figure V. 7 shows the TGA curves obtained after the optimized supercritical fluid debinding cycles. The measured weight loss ratio for the binder A+ Inconel 718 S 62% is 1.85 % and is 3.62 % for binder A + Inconel 718 M 55 %. A weight loss of 1.9 % was expected for the first feedstock and of 3.6 % for the second one. There is no sign of alteration of the behaviour of the thermal degradation on the rest of the polymer as they degrade around the same temperature. The supercritical fluid debinding is confirmed to react only with the PEG and does not damage the sample by taking away some of the powder of the component.

V.3 Effect on the sintering step after a supercritical fluid debinding

V.3.1 Carbon and oxygen analysis

The supercritical fluid debinding allowed a complete removal of the PEG from the components. The next step is to check if we can expect side effects which could impact the rest of the MIM process. After thermal debinding, one of the components was used to perform a combustion analysis via a LECO equipment. The sample was introduced into a high temperature flame and the resulting combustion was analysed with a mass spectrometer. The Table V. 1 shows the carbon and oxygen levels present inside a debinded component with water and a debinded component with supercritical state CO_2. The carbon and oxygen contents is very similar between the two methods. As the sintering after water debinding did not show any signs of carbon or oxygen pollution, the same can be expected during the sintering of a component after supercritical fluid debinding.

Table V. 1Carbon and Oxygen rates inside the powder after solvent or supercritical fluid and thermal debinding

	C (ppm)	O (ppm)
Water debinding	540	1200
CO_2 supercritical debinding	780	1000

V.3.2 Effect on the microstructure

The Figure V. 8 shows the OM images obtained after sintering of a component binder A + Inconel 718 S 71 % and is compared with one obtained after water debinding. In the centre of both samples,

signs of porosity or cavities coming from a poor debinding cannot be found. However, on the surface of the sample, a different problem can be observed. The supercritical fluid debinding helped to maintain the roundness of the component with a neat shape while the water debinding left an irregular microstructure at the surface of the component. The use of the supercritical fluid was less damaging to the surface of the component than the water debinding.

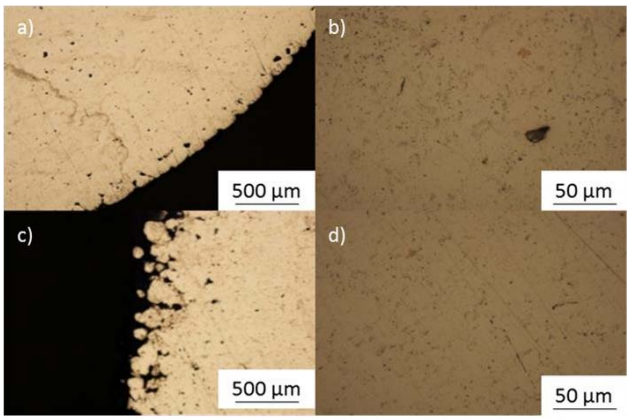

Figure V. 8 OM images of binder A + Inconel 718 S 71 %, sintered at 1290 °C during 4 hours, after supercritical fluid debinding at 150 °C, 40 MPa during 4 hours (a and b) and water debinding at 50 °C during 72 hours (c and d)

The Figure V. 9 shows the OM images obtained after sintering of a component binder A + Inconel 718 M 55 % and is also compared with the one obtained after water debinding. The microstructure was more impacted by the supercritical fluid debinding as cavities were found at the surface of the component. The pressure during the cycle was 50 MPa and components with a spherical powder were damaged. The water debinding worked better with the milled powder than the supercritical fluid debinding.

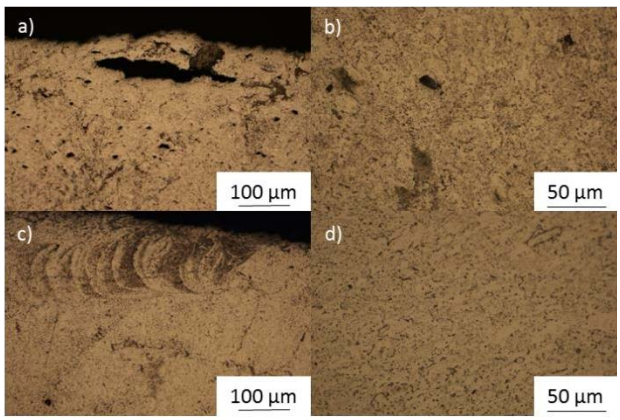

Figure V. 9 OM images of binder A + Inconel 718 M 55 %, sintered at 1290 °C during 4 hours, after supercritical fluid debinding at 150 °C, 50 MPa during 4 hours (above) and water debinding at 50 °C during 72 hours (below)

V.3.3 Roughness characterization

As the supercritical debinding shows an impact on the surface of the component, roughness analyses were performed via an Alicona infinite focus equipment. The optical analysis, by detecting the distance necessary to obtain a focus on the component, builds a 3D topographic model. It was made for two samples, one water debinded at 50 °C during 72 hours and one supercritical fluid debinded at 40 MPa, 150 °C and during 4 hours. The tests were performed along the whole length of the cylinders.

They were analysed after each step of the MIM process (Figure V. 10). In the case of water debinding, the obtained roughness was doubled after applying the method and reached a Rp of 9.27 µm and a Ra of 3.77 µm. On the other hand, in the case of supercritical debinding, the roughness was limited to a Rp of 6.03 µm and Ra of 2.21 µm.

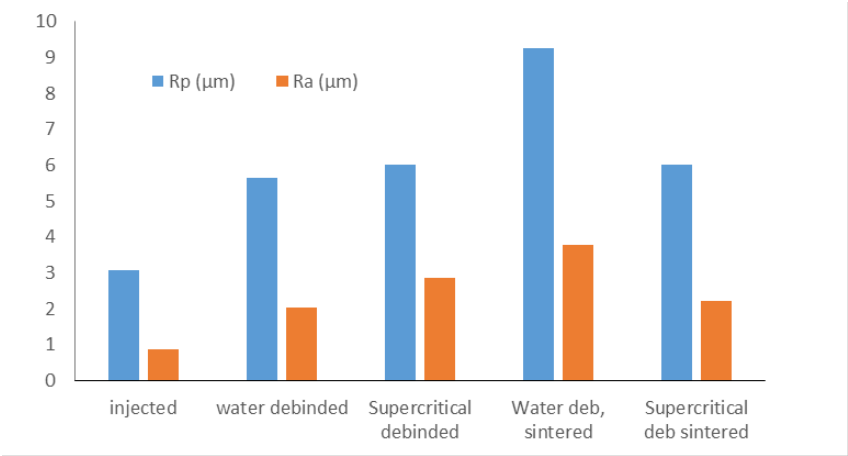

Figure V. 10 Roughness results after each treatments on the MIM samples

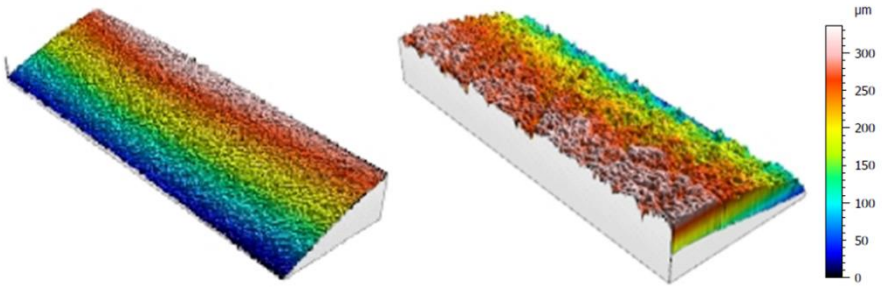

Figure V. 11 3D Roughness profile of sintered samples debinded by supercritical CO_2 and in water

The 3D roughness profile was more regular thanks to a less brutal debinding for the structure of the component obtained after the injection. This behaviour was also observed by Yannig et al [12] in

the case of paraffin debinding. The possibility to obtain a better surface quality could be interesting for an industrial application, as the need for treating the surface of the component is less important.

V.4 Partial remarks

The supercritical fluid debinding was performed only with the binder A, as the binder B was not suitable for this method. It was important to assure the selectivity of the supercritical fluid with only the PEG and not the backbone polymer. In the case of the PP, there were no signs of reaction with the CO_2 in the supercritical state, as seen on the infra-red spectrum.

The tests were performed easily thanks to the possibility to create programs managing the debinding cycles. The debinding cycles were optimized in terms of pressure, temperature and debinding dwell time. The components composed of spherical powders were successfully debinded in a short time. The optimized debinding cycle at 150 °C, 40 MPa during 4 hours allowed a complete extraction of the PEG present inside the component. The temperature needed to optimize the debinding rate is relatively high as it is close to the mixing and injection temperature. Even so, the component did not show signs of defects.

In order to obtain the complete removal of the PEG inside the components composed with the milled powder, it was necessary to use harsher conditions. The pressure of 50 MPa was chosen as it showed the best extraction rate but it was also the maximum allowed pressure before the component could be damaged. The morphology of the powder has an impact on the maximum quantity of PEG that can be extracted by using supercritical fluid debinding. The flake shape particles lowers the diffusion rate of the CO_2 inside the binder. One explication is an irregular structural organisation of the particles inside the MIM component.

Thanks to the metallographic analysis and the pollution tests performed by LECO analysis, it can be concluded that the supercritical debinding method does not change the microstructure of the Inconel 718 in terms of porosity and carbon pollution. The roughness analysis of the components after water debinding and supercritical fluid debinding showed an effect on the surface quality of the final component. After performing the debinding steps and the sintering steps, the quality of the surface of the component debinded by supercritical fluid was improved compared to the water debinding.

After replacing the water debinding by the supercritical fluid debinding, this step became the fastest of the MIM process (Figure V. 12). This process provides an answer to the expectations in terms of time reduction and allows a better quality of the components. However, the main disadvantage at the moment of this method is the price of the equipment compared to the water debinding. Unless the environmental regulations changes, an industrial application for mass production may be difficult.

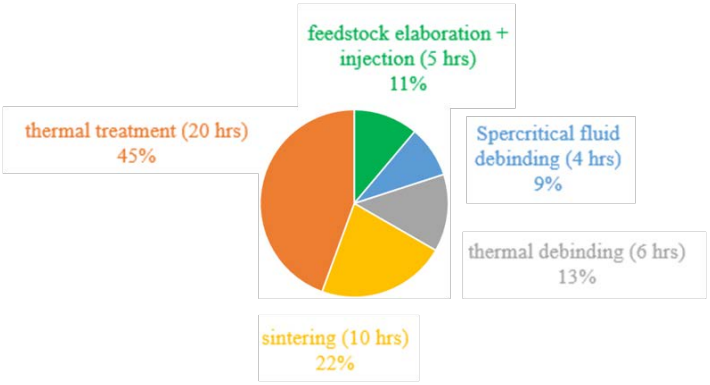

Figure V. 12 Time repartition of the MIM process after using supercritical debinding

REFERENCES

[1] M. T. Zaky, « Effect Of Solvent Debinding Variables On The Shape Maintenance Of Green Molded Bodies », *J. Mater. Sci.*, Vol. 39, Nº 10, P. 3397‑3402, Mai 2004.

[2] M. E. Paulaitis, V. J. Krukonis, R. T. Kurnik, Et R. C. Reid, « Supercritical Fluid Extraction. », *Rev. Chem. Eng.*, Vol. 1, Nº 2, P. 179‑250, Avr. 1983.

[3] J. L. Hedrick, L. J. Mulcahey, Et L. T. Taylor, « Supercritical Fluid Extraction », *Microchim. Acta*, Vol. 108, Nº 3‑6, P. 115‑132, Mai 1992.

[4] T. Shimizu, Y. Murakoshi, T. Sano, R. Maeda, Et S. Sugiyama, « Fabrication Of Micro-Parts By High Aspect Ratio Structuring And Metal Injection Molding Using The Supercritical Debinding Method », *Microsyst. Technol.*, Vol. 5, Nº 2, P. 90‑92.

[5] G. Chen, P. Cao, G. Wen, Et N. Edmonds, « Debinding Behaviour Of A Water Soluble Peg/Pmma Binder For Ti Metal Injection Moulding », *Mater. Chem. Phys.*, Vol. 139, Nº 2–3, P. 557‑565, Mai 2013.

[6] H. S. Kim, J. M. Byun, M. J. Suk, Et Y. D. Kim, « Powder Injection Molding Of Translucent Alumina Using Supercritical Fluid Debinding », *J. Korean Powder Metall. Inst.*, Vol. 21, Nº 6, P. 407‑414, 2014.

[7] T. Chartier, F. Bordet, E. Delhomme, Et J. François Baumard, « Extraction Of Binders From Green Ceramic Bodies By Supercritical Fluid: Influence Of The Porosity », *J. Eur. Ceram. Soc.*, Vol. 22, Nº 9–10, P. 1403‑1409, Sept. 2002.

[8] S. T. Lin Et R. M. German, « Extraction Debinding Of Injection-Molded Parts By Condensed Solvent », *Int. J. Powder Metall.*, Nº 21(5), P. 19‑24, Ocotber 1989.

[9] W.-W. Yang, K.-Y. Yang, M.-C. Wang, Et M.-H. Hon, « Solvent Debinding Mechanism For Alumina Injection Molded Compacts With Water-Soluble Binders », *Ceram. Int.*, Vol. 29, Nº 7, P. 745‑756, Janv. 2003.

[10] D.-S. Tsai Et W.-W. Chen, « Solvent Debinding Kinetics Of Alumina Green Bodies By Powder Injection Molding », *Ceram. Int.*, Vol. 21, Nº 4, P. 257‑264, Janv. 1995.

[11] T. Chartier, M. Ferrato, Et J.-F. Baumard, « Influence Of The Debinding Method On The Mechanical Properties Of Plastic Formed Ceramics », *J. Eur. Ceram. Soc.*, Vol. 15, Nº 9, P. 899‑903, 1995.

[12] T. Yannig Et E. Baril, « Benefits Of Supercrititical Co2 Debinding For Titanium Powder Injection Moulding? », *World Pm Proc.*, Vol. 4, P. 315‑321, 2010.

VI FIELD ASSISTED HOT PRESSING OF INCONEL 718 MIM COMPONENTS

The complete sintering cycle of the Inconel 718 by using a conventional sintering furnace needs, at least, 10 hours to obtain a densified material and a subsequent thermal treatment of 20 hours in order to obtain the best properties of the material. The furnace provides to the powder the needed temperature by heating the atmosphere around it and this heat is transferred by diffusion to the powder. The principal flaw with the use of furnaces is the energy to maintain the temperature for a long time. Moreover, it also consumes a lot of gas if the material has to be sintered (and this is the case for the Inconel) in a controlled atmosphere.

In the part II, the FAHP sintering is introduced as a method to heat the material thanks to an electric current while the powder is maintained under pressure. By adjusting the intensity of the current, it is possible to reach high temperatures with a high heating rate, sintering components in a few minutes. It was decided to apply this method to Inconel 718 powders and MIM samples with the goal to find an alternative to the furnace sintering and to obtain a dense material faster than with conventional sintering in order to reduce the energy costs.

The FAHP sintering method has yet to be investigated on the sintering of Inconel 718. Hence, there is no information on the effect of this method on the material. In this chapter, the methodology and the equipment used are first introduced. This is followed by the application of the method on the MIM components and the effects observed on the microstructure of the material and its mechanical performances. The tests are all performed with the goal of not damaging them and to keep the shape of the MIM components.

The last part introduces the application of a second heating cycle after the optimized sintering cycle in order to perform a thermal treatment of the material. The effects on the microstructure were observed by TEM in order to observe the effect of the FAHP sintering on the γ', γ'' and δ phases. All of the FAHP tests were performed on the components binder B + Inconel 718 S 62 % in both bars and cylinder shape. They were all solvent and thermal debinded before performing the tests.

VI.1 FAHP sintering process

VI.1.1 Description of the equipment

The FAHP method has some similar parameters with the Spark Plasma Sintering process. It is mainly characterized by the sintering produced by an alternative direct current circulating through a die, maintained under uniaxial pressure; in SPS the sintering is produced with a continuous current supply system. As seen on Figure VI. 1, the powder is placed between two sets of punches that are part of the current path. In our case, the temperature distribution in the sample between the jaws is not uniform and a parabolic temperature results with a peak temperature at the centre of the sample [1]. The sintering is performed inside a chamber with a controlled atmosphere. It was chosen to perform the sintering into a high level vacuum (at least 10^{-4} Pa). During the tests, the Inconel 718 powder is directly introduced into a graphite die, composed of a main cylinder pierced with an intern diameter of 10mm and of two punches of the same diameter. In order to protect the equipment and to improve the electric contacts between the different parts of the system, a foil is placed between the powder and the die.

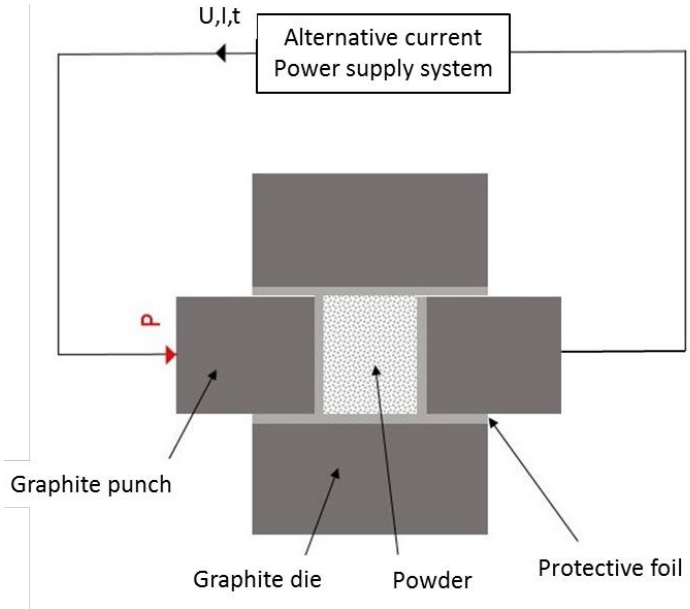

Figure VI. 1 Gleeble 3800 representative system

The temperature is followed in situ via two thermocouples placed in the middle of one punch and the second one in the die, as close as possible to the powder. The shrinkage of the powder is also in-situ observed thanks to the measurement of the displacement of the punch. The alternative current

that is applied during the tests is managed by the software of the equipment. The intensity and the voltage is regulated in function of the answer between the heating rate and the programmed temperature and the measured temperature.

The Figure VI. 2 shows the applied cycles to the samples during the tests. The minimum pressure to hold the set-up is applied at 5 MPa until reaching 600 °C. At this temperature, the programmed pressure is applied during 40 seconds and the temperature is raised until the programmed temperature. Once the dwell time is over, the current is stopped and the pressure is maintained until reaching the end of the cooling. The followed cooling rate between 60 and 80 °C/min, depending of the programmed temperature.

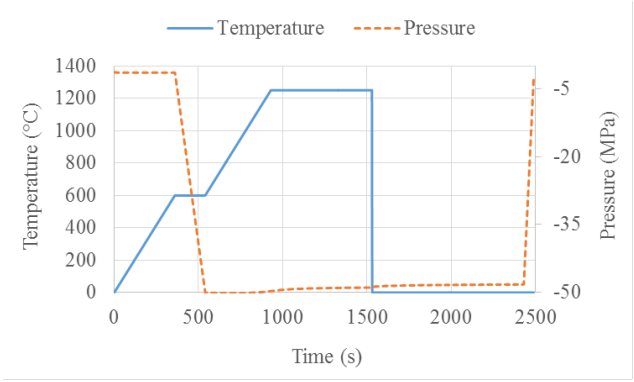

Figure VI. 2 Example of FAHP sintering cycle applied at each tests

VI.1 FAHP sintering of Inconel 718 powder

VI.1.1 Protective foil

The first tests were performed with a SPS equipment FCTsystem HPD 125, at the University of Burgundy (Dijon, France), with the help of the MaNaPi research team of the ICB laboratory. The equipment is working in the same way as the FAHP equipment, the difference is the type of current used. The SPS equipment provides a pulsed current instead of an alternative current. The temperature is also not followed via thermocouples but via infra-red pyrometer focused on the centre of the die. The tests were realized with the usual set-up, by using die, punch and protective foil, all in graphite, in order to extend the working life of the tools.

The Figure VI. 3 shows the Inconel 718 shrinkage with a heating rate of 50 °C/min, a pressure of 10 MPa and temperature of 1290 °C as it was the best sintering temperature with a furnace. This test

was made in order to obtain a dilatometric curve and to identify the best sintering temperature. The maximum was obtained around 1250 °C. The shrinkage rate indicates that the powder started shrink slower once 1200 °C was reached. It can be considered that once this temperature is reached, it is the most efficient to obtain full densification of the powder. The next test will be performed around this temperature with a dwell time in order to complete the densification.

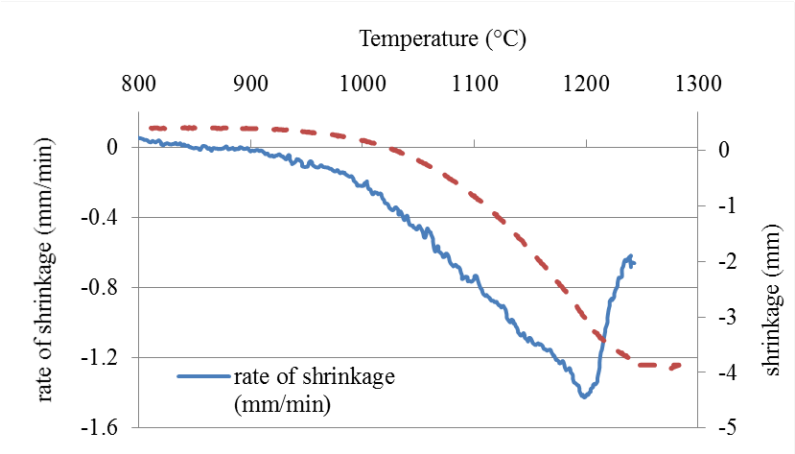

Figure VI. 3 Shrinkage and rate of shrinkage vs temperature during SPS sintering of Inconel 718 powder at 50 °C/min maintained 5 minutes

The next tests performed was set at 1200 °C and maintained 5 minutes. The extraction of the bulk material was difficult as the punches were stuck on the sample. It was cut in the middle and observed by SEM. The Figure VI. 4 shows the obtained microstructure. A multi-layer microstructure with three distinct phases can be observed. The EDX analysis resumes the chemical composition of the different phases observed on the different marked zones. The zone 1, which is close to the centre of the bulk material, has the composition of the Inconel 718 powder. The zone 2, compared to zone 1, contains less nickel, titanium, chromium and a higher carbon and iron concentration. The zone 3 is a chromium rich phase and the zone 4 is composed of almost half of carbon and the rest is mostly iron and nickel. The zone 5 has 10 % of carbon, 64 % of niobium, 7 % of molybdenum, 11 % of titanium and almost no traces of iron and nickel. The 3 later zones are close to the contact surface of the carbon punch. During the sintering, it seems that a diffusion of the carbon inside the bulk material attracted elements such as the titanium, the niobium and the chromium from the centre of the bulk sample and produced a layer full of carbides.

This kind of reaction was shown by another study by Garcia-Junceda et al. on the diffusion of carbon during FAHP sintering of an iron powder [2]. From the surface to the centre, it was formed the same kind of multilayer material with the formation of cementite and perlite thanks to the carbon

diffusion. They were able to block completely the carbon diffusion by replacing the graphite foil with a tungsten foil. Hence, it will be used for the next tests in our set-up in order to protect the Inconel 718 powder.

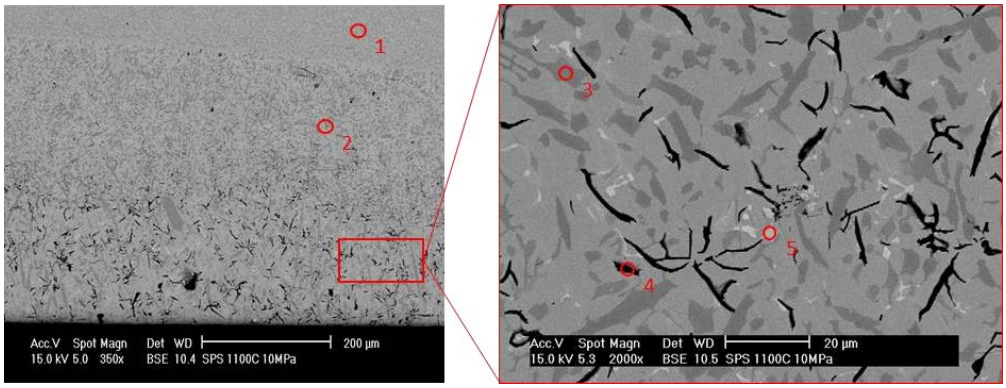

Figure VI. 4 SEM images obtained after sintering at 1200 °C during 5 min at 50 °C/min

Table VI. 1 EDX analysis of the zones marked on Figure VI. 4

Element (wt.) %	Zone 1	Zone 2	Zone 3	Zone 4	Zone 5
C K	2.8	4.3	-	42.98	11.04
Al K	-	-	-	0.33	1.21
Nb L	2.49	11.3	-	0.7	64.2
Mo L	-	-	4.3	0.7	7.03
Ti K	0.82	0.52	-	-	11.37
Cr K	18.08	10.3	67.02	3.27	3.14
Fe K	17.3	23.87	16.48	12.81	1.39
Ni K	58.51	49.71	12.19	39.91	1.83

VI.1.2 Optimization of the pressure

The firsts FAHP tests were performed on the Inconel 718 S powder in order to observe the behaviour of the material while sintering with the FAHP equipment. The different parameters allowing the best shrinkage is described through the analysis of the sintering temperature. During the SPS sintering, it was found that 1200°C was the best temperature. However, the FAHP equipment is different and the graphite foils were changed by tungsten. These two modifications force to do new tests.

The tests were performed on MIM samples, introduced inside the graphite die and the tungsten protective foils. The debinding was performed at a higher temperature of 600 °C instead of 500 °C, which allowed the components for manipulation and transport to the FAHP equipment. The Figure VI. 5 shows the results, obtained after FAHP sintering at different pressures, square shaped components inside the cylindrical die. A starting pressure of 50 MPa was chosen but the component was crushed and lost its shape. The minimum pressure that has to be applied in order for the equipment to work properly is 5 MPa. It was possible to reach 10 MPa without destroying the shape or observing cracks at its surface.

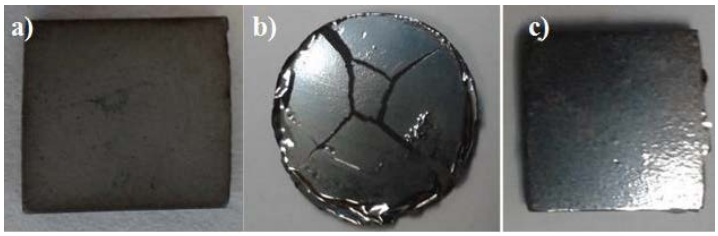

Figure VI. 5 Images of the sample a) debinded at 600 °C during 2 hours b) sintered by FAHP at 50 MPa and c) 10 MPa, both at 1250 °C during 10 min

VI.1.3 Optimization of the temperature

The Figure VI. 6 shows the shrinkage observed during FAHP sintering cycles at different temperatures and a dwell time of 10 minutes. Between 1100 and 1200 °C it can be seen that at the end of the dwell time, a temperature of 1100 °C is not high enough to complete the shrinkage of the powder. Between 1200 °C and 1250 °C, the two peaks are closer and it is difficult to conclude on which temperature is ideal for a good sintering of the powder.

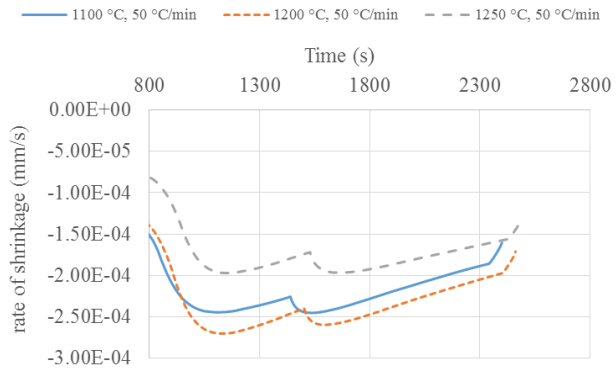

Figure VI. 6 Rate of shrinkage vs sintering time during FAHP sintering of Inconel 718 S powder maintained 10 minutes and under 50 MPa

The bulk materials were characterized and their microstructure is shown in Figure VI. 7. At 1100°C, as expected from the evolution of the shrinkage, the porosity is important inside of the material with a relative density of 87.1 ± 1.3 %. At 1200 °C, it is reaching 91.4 ± 0.9 % of relative density, while it is 98.8 ± 1.1 % once the temperature is of 1250 °C. Hence, the sintering temperature for the Inconel powder with the FAHP method needs to be at least 1250 °C in order to reach near full density of the component.

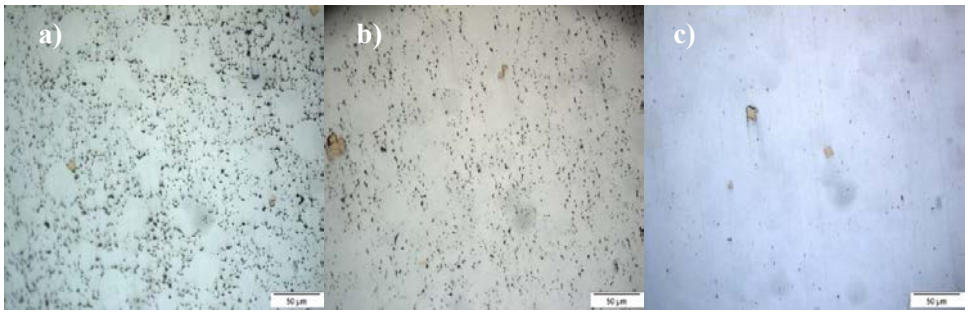

Figure VI. 7 OM images of the samples sintered by FAHP at a)1100°C, b) 1200°C and c) 1250°C at 50 °C/min

The Figure VI. 8 shows the SEM images of the sample obtained at 1250 °C, 50 °C/min of heating rate and a dwell time of 10 minutes. There are no signs of carbon diffusion at the surface of the components and the tungsten did not affect the chemical composition of the material as shown in the EDX analysis results in

Table VI. 2.

The composition is close to the starting powder and carbon is not observed. The only defect that was seen is the presence of titanium nitride grains as revealed in zone 2. It can come from the multiple powder manipulation and the thermal debinding of the polymers. These images confirm the use of 1250 °C as sintering temperature and that the tungsten foil are effective against the carbon diffusion.

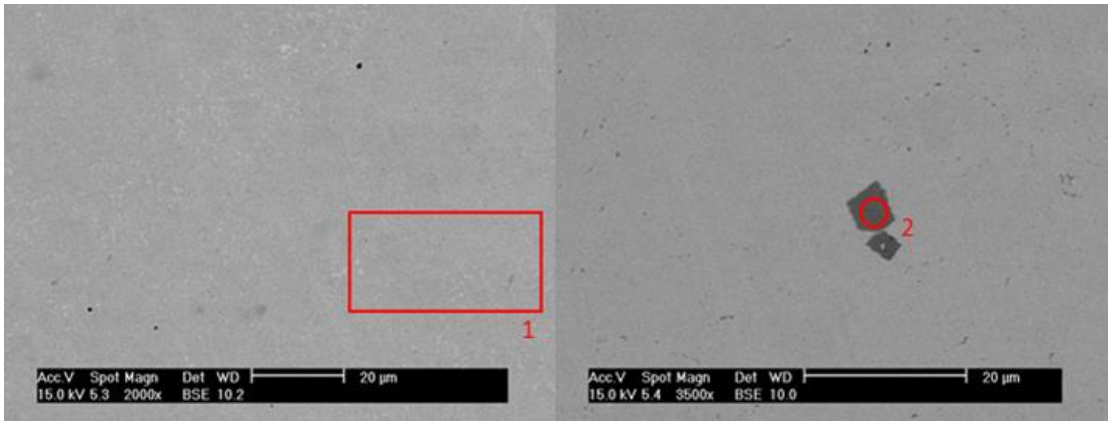

Figure VI. 8 SEM images of MIM component sintered at 1250 °C under 10 MPa at 50 °C/min during 10 minutes

Table VI. 2 EDX analysis of the zones marked on Figure VI. 8

Element (wt.) %	Zone 1	Zone 2
C K	-	2.27
N K	-	16.27
Al K	0.62	-
Nb L	5.1	6.9
Mo L	2.33	-
Ti K	1.06	71.04
Cr K	18.94	1.88
Fe K	18.62	-
Ni K	53.34	1.64

VI.1.4 Optimization of the heating rate

The advantage of the FAHP sintering is the application of a high heating rate. Once the sintering temperature was decided, it is now possible to adjust this parameter. The Figure VI. 9 shows the shrinkage as function of the time during FAHP sintering at a heating rate comprised between 300 and 600 °C/min. The shrinkage was improved between 50 and 100 °C/min by around 0.22 % of the initial length of the MIM component. Between 100 and 300 °C/min, the shrinkage is once again lowered by around 0.40%. .However at 600 °C/min the shrinkage is lesser than with all the other heating rates. This heating rate is close to the limit of the equipment and the temperature regulation was not as regular as during the other experiments. Hence, it was chosen to keep working with the speed of 300 °C/min in order to avoid troubles with the equipment and reducing the repeatability of the tests at 600 °C/min.

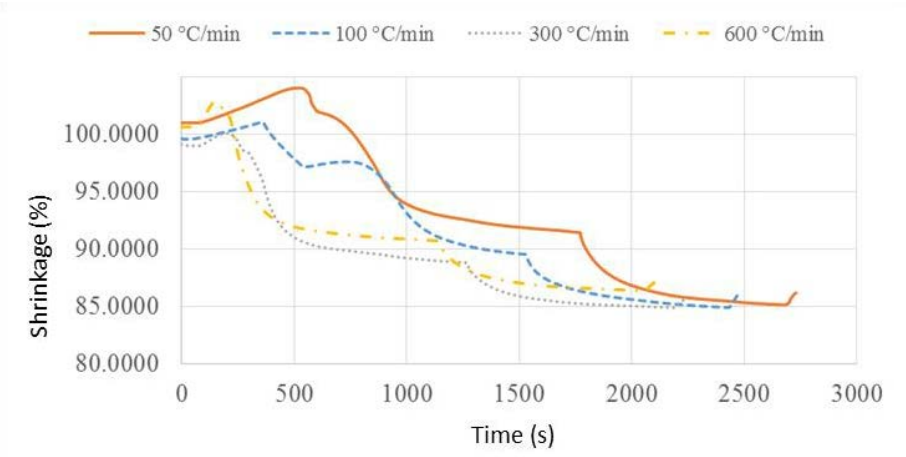

Figure VI. 9 Shrinkage vs time during FAHP sintering at 1250 °C of Inconel 718 S powder at different heating rate

The Figure VI. 10 shows the microstructure of the MIM component sintered at 1250 °C at 300 °C/min and obtained after electro-polishing. It can be found a homogeneous repartitions of small white phases inside the grains of the microstructure.

The Figure VI. 10 resumes the chemical elements measured by EDX on the observed zones. The zone 1 is composed of 10 % of carbon, meaning that carbides are still present inside the microstructure. It is difficult to conclude if they are caused by the graphite set-up or if they were not correctly eliminated during the thermal debinding. The zone 2, corresponding to the matrix of the material, and the zone 4, being on the grain boundaries, are both close to the chemical composition of the Inconel 718 starting powder. Carbon traces are also observed but in a fewer proportion. Finally, the white inclusions, observed in zone 5 are chromium and niobium rich phases, corresponding to the composition of the γ', γ'' and δ phases.

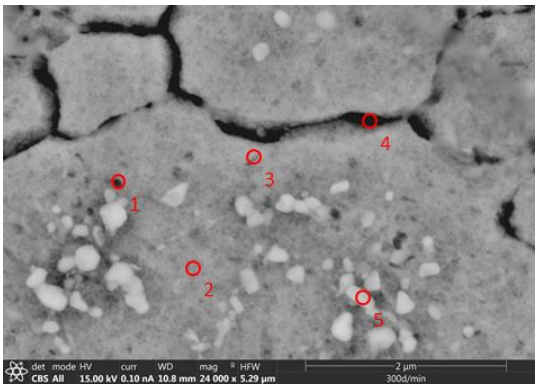

Figure VI. 10 SEM image after electro-polishing of MIM component sintered at 1250 °C, 300 °C/min under 10 MPa during 10 minutes

Table VI. 3 EDX analysis of the zones marked on Figure VI. 10

Element (wt.) %	Zone 1	Zone 2	Zone 3	Zone 4	Zone 5
C K	10.73	0.22	0.32	0.28	0.11
Al K	0.98	-	-	1.22	0.93
Nb L	5.82	7.68	19.59	4.23	15.42
Mo L	0.95	1.01	2.12	1.81	-
Ti K	4.52	4.84	1.74	1.28	-
Cr K	15.33	17.2	12.93	18.98	16.55
Fe K	19.2	18.55	14.26	19.19	18.2
Ni K	42.47	50.5	49.03	53.01	48.79

VI.1.5 Optimization of the dwell time

The last parameter to optimize is the dwell time at the sintering temperature. Two test were performed at the temperature of 1250 °C: 10 and 15 minutes of dwell time. The final shrinkage is really close and the rate of shrinkage does not show any particular differences of behaviour between the two cycles (Figure VI. 11). Moreover, the microstructures are both really close with a low porosity level and no particular phases appearing in the SEM images in Figure VI. 12. A longer sintering time may have affected the performance of the material, meaning that the mechanical characterization will help to conclude on the best dwell time. They are both tested for the tensile strength tests in order to observe if their behaviour is different.

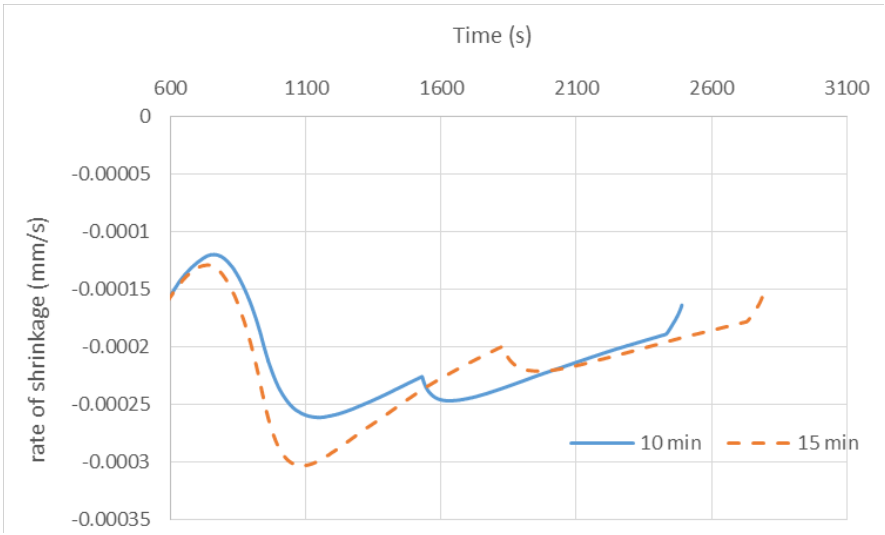

Figure VI. 11 Rate of shrinkage vs time during FAHP sintering at 1250 °C, 300 °C/min under 10 MPa at different dwell times

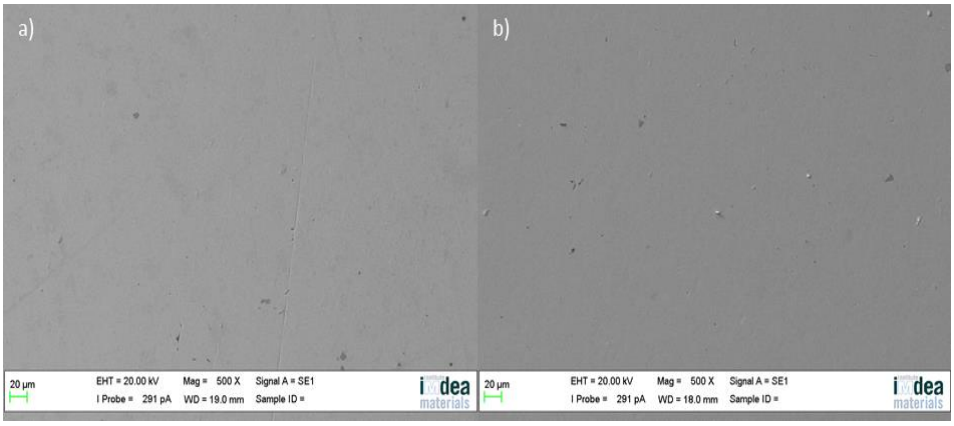

Figure VI. 12 SEM images of MIM component sintered at 1250 °C under 10 MPa at 50 °C/min during 10 minutes (left) and 15 min (right)

VI.1.6 Bulk material mechanical characterization

In order to conclude on the FAHP sintering parameters the Table VI. 4 shows the density and hardness results obtained with the parameters previously introduced. It sums up the different density and hardness values obtained with the different cycles performed with the FAHP equipment. The best cycle, in terms of hardness seems to be of 1250 °C at 300 °C/min during 10 minutes. In terms of density, adding 5 minutes to dwell times slightly improves the final density, but the measured hardness is lowered. The final decision on the best sintering cycle will be taken after the mechanical characterization of the two components.

Table VI. 4 Density and hardness obtained after different FAHP sintering cycles under a pressure of 10 MPa

Sintering temperature (°C)	Heating rate (°C/min)	Dwell time (min)	Density (%)	Hardness (HV)
1100	50	10	87.1 ± 1.3	198 ± 12.3
1200	50	10	91.4 ± 0.9	216 ± 6.4
1250	50	10	98.8 ± 1.1	253 ± 11.0
1250	100	10	99.3 ± 1.2	258 ± 3.3
1250	300	10	99.2 ± 0.8	265 ± 4.5
1250	600	10	97.8 ± 1.2	235 ± 6.8
1250	300	15	99.5 ± 1.2	251 ± 3.6

The Figure VI. 13 resumes the results of the tests performed on the two components with a MTS Criterion Model 45 tensile test equipment. The two components have two different behaviours. The FAHP sintering at the optimized conditions maintained during 10 minutes displays an important elongation during the test until a mean value of 48 % of the working length of the tested samples. The component sintered during 15 minutes is breaking after a much shorter strain around 12.5 %, yet it is breaking at a higher tensile strength and the yield strength is also higher.

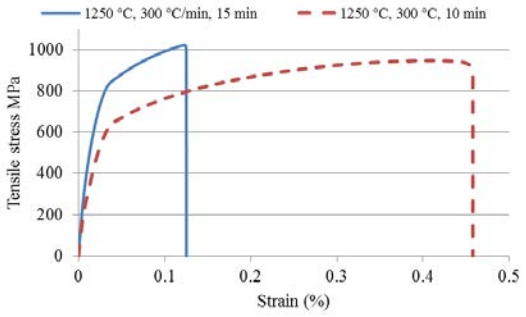

Figure VI. 13 Tensile strength test of the FAHP sintered component Binder B + Inconel 718 S 62 % at 1250 °C maintained during 10 and 15 min

The Table VI. 5 resumes the different properties obtained after the tensile strength tests and is compared with the results obtained with the MIM component after conventional sintering, and the properties obtained by Valencia [3] after applying a heat treatment. The properties after FAHP treatment are higher than during the conventional sintering, but the elongation behaviour is close to the component FAHP sintered during 10 minutes. The properties obtained by Valencia are more close to the component FAHP sintered during 15 minutes. It was observed that a material with a higher density obtained after sintering is displaying a better behaviour under tensile stress [4]. The difference of density between the two components is of 0.3 %, the difference in behaviour may also come from a different microstructure, as the behaviour is closer to a thermally treated material. Thus, it can be concluded that leaving the FAHP sintering 5 minutes longer at 1250 °C has an effect close to a heat treatment applied during at least 10 hours.

Table VI. 5 Mechanical properties obtained from the tensile strength test of the sintered component by FAHP and compared to the conventional MIM components

Sample	YS (MPa)	E (GPa)	UTS (MPa)	Elongation (%)
10 min	634 ± 8	34.91 ± 3.11	948 ± 85	48
15 min	814 ± 27	48.71 ± 3.14	1022 ± 47	12.5
furnace	465 ± 13	63.4 ± 3.8	817 ± 14	31.5
Valencia [3]	972	-	1194	17.4
Project specifications	> 500	-	> 700	12

The Figure VI. 14 shows the SEM images taken during the in-situ micro-tensile strength tests. The images indicates a brittle breaking behaviour for both of the sintering time. For the component FAHP sintered 10 minutes, the development of a crack around a particle is observed at 900 MPa. It is the origin of the fracture. The crack is formed around a poorly sintered particle. The propagation of the crack lead to the fracture of the sample around 950 MPa. This mechanical behaviour is typical of the powder sintered components [5] and was already observed for the component sintered in a furnace. However, the fracture profile is different as no dimples is present. The fracture profile shows a cleavage fracture.

The component FAHP sintered during 15 minutes displays the same brittle fracture profile with the same cleavage fracture. It was not possible to observe the starting point of the fracture. On the fracture profile, a particle with cracks around it could have led to the same fracture mechanism

observed for the component FAHP sintered 10 min. It can be concluded that the FAHP sintering of the Inconel 718 MIM components increases the contact surface between the particles on the contrary of a material usually obtained with the traditional powder metallurgy [6] and explains the better performances of the FAHP sintered components under a tensile stress.

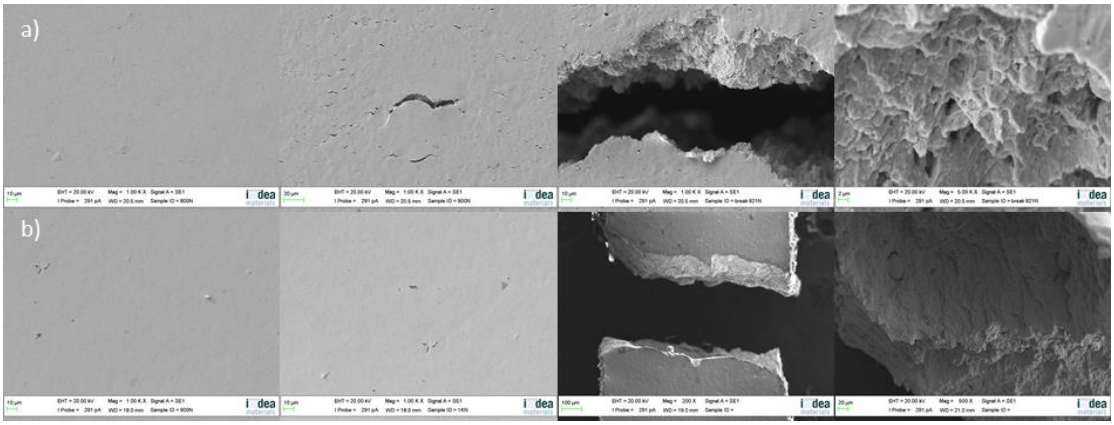

Figure VI. 14 SEM images obtained at different tensile stress of the FAHP sintered components at 1250 °C, 300 °C/min under 10 MPa and during a) 10 min and b) 15 min

VI.2 Heat treatment after sintering.

The results obtained after the optimized sintering cycle were good in terms of microstructure and mechanical behaviour, yet they were still below the properties obtained after a full heat treatment. Thus a second heating cycle was applied after the sintering cycle as shown on Figure VI. 15. A second cycle of 750 °C at 300 °C/min during 15 minutes and under 10 MPa was applied after the cooling of the optimized sintering cycle.

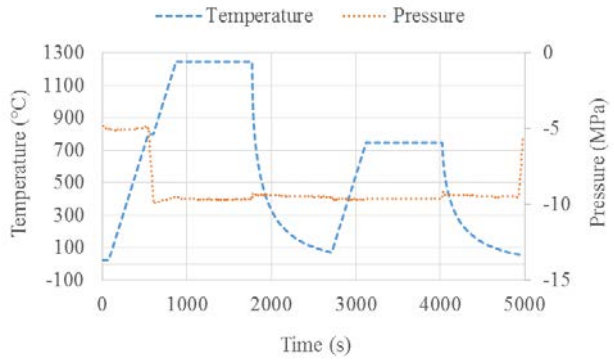

Figure VI. 15 Thermal treatment applied with FAHP equipment to a MIM component

The obtained relative density was of 99.4 ± 0.3 % and a hardness of 394 ± 6 HV. The SEM images displays the obtained microstructures. A microstructure close to the one observed after the furnace heat treatment with white reach phases composed in majority of niobium. The presence of these phases was confirmed inside the grains after electro-polishing. Compared to the image obtained after the sintering cycle, the white crystals are more concentrated at the grain boundaries.

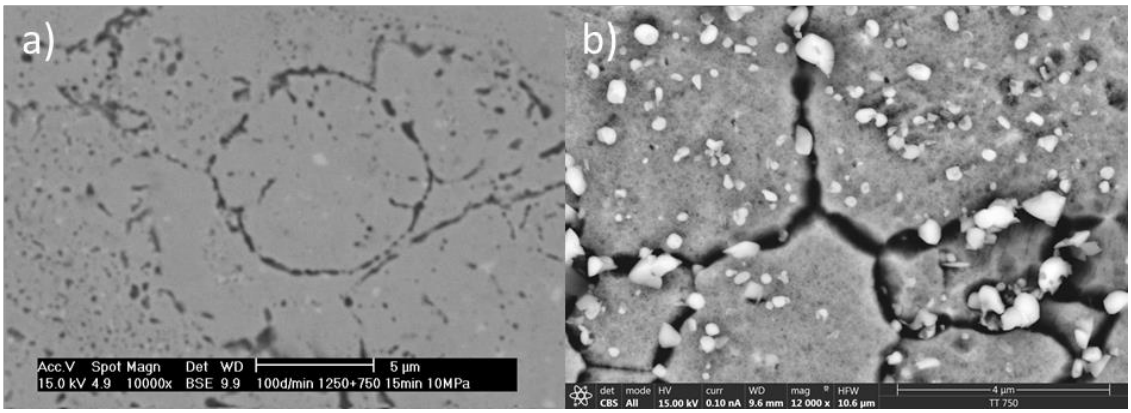

Figure VI. 16 SEM images of MIM component sintered at 1250 °C under 10 MPa at 50 °C/min during 10 minutes a) before and b) after electro-polishing

The Figure VI. 17 shows the TEM images of the component treated at 750 °C. The images were taken on the (111) axis of the material as identified in image a). It follows the same procedure as Sundaraman et al [7]–[9] explained. By using this orientation, it is possible to observe both γ' and γ'' phases and the δ as well. They are the three main phases that can be promoted during the heat treatment.

On the image from b) to d), a grain size of 782.9 ± 211.8 nm can be observed with inclusions at the grain boundaries with a size of 130.8 ± 42.2 nm. It can be noted that some of the grains exhibits twins, which could explain the high hardness measured. Fournier et al shown that a inhomogeneous propagation of the plastic deformation was favorited by mechanical twins [10]. The image e) and f) are images taken at high resolution inside the grain matrix. Two different kind of precipitates can be observed. The first ones are elliptical and was attributed to γ' and γ'' phases [9], [11]. The second one displays a needle shape and this one is attributed to the δ phase [12]. This confirms the presence of the hardening phases inside of the grains, however they are in presence of the less performant δ phase under tensile stress. The TEM images also indicates that more than ten times a lower grain size compared to the one observed during furnace sintering (12.7 µm). The Hall-Petch effect is the inverse relationship between the yield strength and the grain size, which could explain the better mechanical results obtained after the FAHP sintering [13].

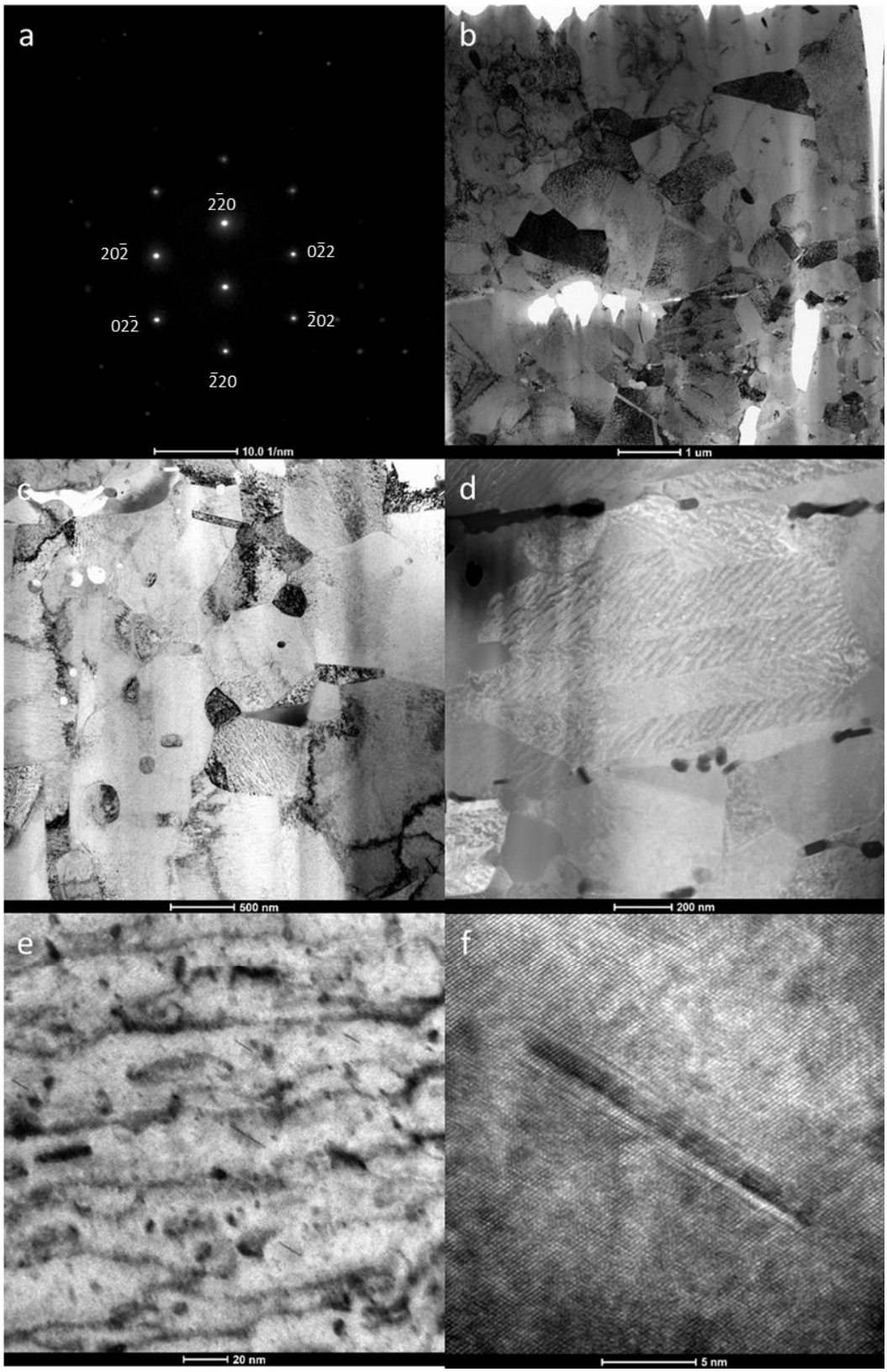

Figure VI. 17 (a) SAD pattern identified as the zone [111]γ axis for the matrix and (b) to (f) TEM images of Inconel 718 62% + binder B sintered by FAHP at 1250 °C at 100 °C/min, during 15 min and a second FAHP cycle applied at 750 °C, 100 °C/min during 15 min

The Figure VI. 18 resumes the results of the mapping performed by EDX on the image d) of the previous figure The copper was measured as it is composing the support used for the sample. It was performed in order to identify the element repartition inside and around one the grains. The first thing that can be noted is that the aluminium, the niobium and a part of titanium and of the chromium is found into the inclusions at the grain boundaries. It is important to note that the nickel, the iron is not present inside of these inclusions. There are inclusions that corresponds to both chromium and niobium. The molybdenum is homogeneously distributed inside the grain. The iron, chromium and nickel are corresponding to the matrix inside the grain as expected.

The carbon element was observed all over the grain but that kind of carbon pollution was not observed during SEM measurements. It means that it can come from pollution during the preparation of the sample or the carbon element can only be observed at this kind of scale. There is still a high chance that some of the niobium precipitates are corresponding with the observed higher carbon concentration, meaning that the presence of Niobium carbides is confirmed at the grain joints.

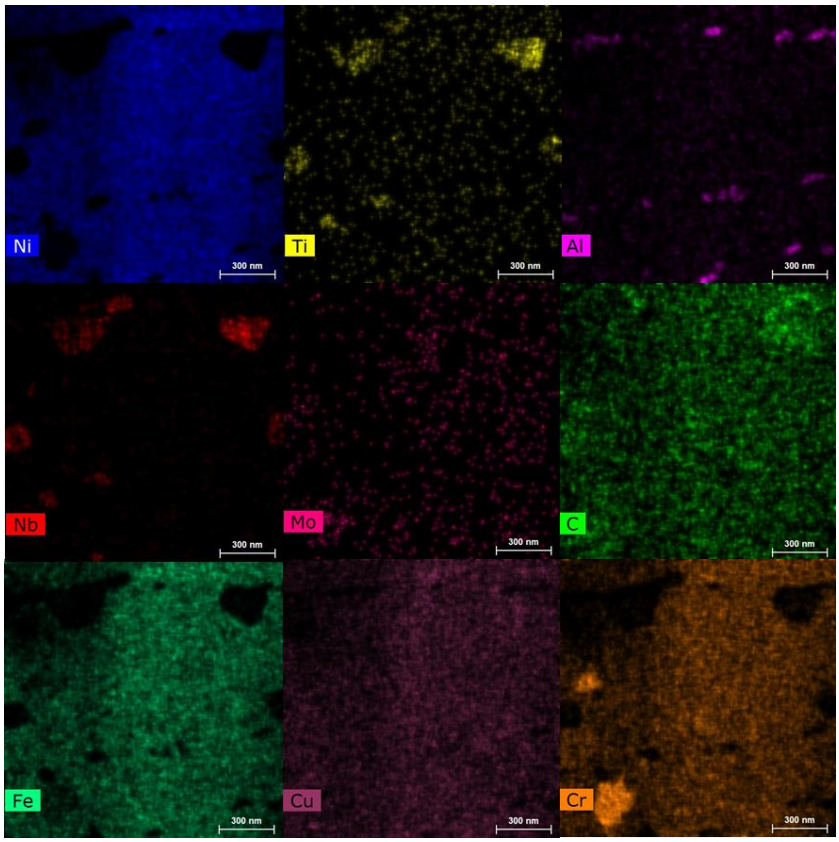

Figure VI. 18 EDX analysis performed with TEM on a grain of Inconel 718 62% + binder B sintered by FAHP at 1250 °C at 100 °C/min, during 15 min and a second FAHP cycle applied at 750 °C, 100 °C/min during 150 mins

VI.3 Partial remarks

The FAHP sintering of MIM Inconel 718 was successfully developed in order to obtain components. The sintering cycle is optimized for each parameters in order to obtain a fully dense material without damaging the shape of the component. The condition to perform a good sintering process without damaging the tools and polluting the material is to use tungsten foil in order to protect the set-up.

The applied pressure is almost at the minimum limit necessary for the method to be performed. However, during the injection, the powder compact was obtained after being injected at a high pressure. This may have helped to perform the tests without applying high pressure on the set-up. The sintering temperature was lower than during the furnace sintering with 40 °C less. The dwell time and the heating rate are allowing a sintering cycle in around 45 minutes thanks to the method a rapid cooling.

The bulk material were characterized in order to compare the mechanical performances with the components obtained during the furnace sintering and the literature. It appears that the properties obtained after FAHP sintering are higher than after a sintering cycle of 10 hours, but are still lower than after applying a heat treatment of 16 hours. Hence, a second heating cycle at 750 °C was performed after the sintering cycle at 1250 °C and the obtained hardness was much higher. The observations by SEM and TEM put in evidence a much finer grains and the presence of hardening phases inside the matrix, but also at the grain boundaries as inclusions. The negative aspect is the presence of the carbon pollution at the surface of the component which leaves room for improvement of the process.

REFERENCES

[1] Dynamic Thermal/Mechanical Metallurgy Using The Gleeble 1500, 2nd Ed. NY: Duffers Scientific, 1985.

[2] A. García-Junceda, « Study And Suppression Of The Microstructural Anisotropy Generated During The Consolidation Of A Carbonyl Iron Powder By Field-Assisted Hot Pressing », Metall. Mater. Trans. A, Vol. 46(7), 2015.

[3] J. J. Valencia, « Sintering Effect On The Microstructure And Mechanical Properties Of Alloy 718 Processed By Powder Injection Molding », Miner. Met. Mater. Soc., Vol. Superalloys 718,625,706 And Various Derivatives, 1997.

[4] N. Chawla, X. Deng, M. Marucci, Et K. Narasimhan, « Effect Of Density On The Microstructure And Mechanical Behavior Of Powder Metallurgy Fe-Mo-Ni Steels », Janv. 2003.

[5] S. Carabajar, C. Verdu, Et R. Fougeres, « Damage Mechanisms Of A Nickel Alloyed Sintered Steel During Tensile Tests », Mater. Sci. Eng. A, Vol. 232, Nº 1‑2, P. 80–87, 1997.

[6] N. Candela, F. Velasco, Et J. M. Torralba, « Fracture Mechanisms In Sintered Steels With 3.5%(Wt.) Mo », Mater. Sci. Eng. A, Vol. 259, Nº 1, P. 98‑104, Janv. 1999.

[7] M. Sundararaman, P. Mukhopadhyay, Et S. Banerjee, « Some Aspects Of The Precipitation Of Metastable Intermetallic Phases In INCONEL 718 », Metall. Trans. A, Vol. 23, Nº 7, P. 2015‑2028, Juill. 1992.

[8] M. Dehmas, J. Lacaze, A. Niang, Et B. Viguier, « TEM Study Of High-Temperature Precipitation Of Delta Phase In Inconel 718 Alloy », Advances In Materials Science And Engineering,2011.

[9] L. Chang, W. Sun, Y. Cui, F. Zhang, Et R. Yang, « Effect Of Heat Treatment On Microstructure And Mechanical Properties Of The Hot-Isostatic-Pressed Inconel 718 Powder Compact », J. Alloys Compd., Vol. 590, P. 227‑232, Mars 2014.

[10] D. Fournier Et A. Pineau, « Low Cycle Fatigue Behavior Of Inconel 718 At 298 K And 823 K », Metall. Trans. Vol. 8a July 1977-1095.

[11] C. Slama Et G. Cizeron, « Étude Du Comportement Structural De L'alliage NC 19 Fe Nb (Inconel 718) », J. Phys. III, Vol. 7, Nº 3, P. 24, 1997.

[12] A. Niang, J. Huez, J. Lacaze, Et B. Viguier, « Characterizing Precipitation Defects In Nickel Based 718 Alloy », Mater. Sci. Forum, Vol. 636‑637, P. 517‑522, Janv. 2010.

[13] E. N. Hahn Et M. A. Meyers, « Grain-Size Dependent Mechanical Behavior Of Nanocrystalline Metals », Mater. Sci. Eng. A, Vol. 646, P. 101‑134, Oct. 2015.

VII MICROWAVE SINTERING AND HEAT TREATMENT

Microwave heating offers a number of advantages over the conventional heating methods, such as non-contact heating, selective material heating, rapid heating, quick start-up and stopping, reduction in processing time and unique material microstructure and properties [1]. The use of microwaves (MW) in order to sinter powders is well developed in the case of ceramic powders [2], [3]. However, it is only recently that the process was applied to metal powders[4] such as pure nickel [5] or carbides [6]. The tests performed on metallic materials did not show an exceptional heating rate, around 30 °C/min for the sintering of a 316L steel powder [7], [8] but the interesting point is the reduction of dwell time at the peak temperature for only 10-15 minutes [9].

Most of the research was performed on pressed components and the application of the MW sintering method on MIM green or brown components is not too developed [9], [10]. The process is still highly sensitive to the material and to its shape, as it is ease to create an electric discharge such as electrics arcs due to the interaction metal-microwave. This chapter's topic is the application of a thermal treatment to brown MIM component and sintered bodies. They were performed on an equipment designed by Sairem (Neyron, France). The first equipment is a single mode cavity microwave sintering equipment that can work in inert atmosphere. The second one is a plasma microwave equipment. It is designed to maintain a uniform plasma flame with argon gas. The first part of the chapter presents the effect of the application of the microwaves on the MIM components with the different configuration presented in the first chapter. The second part presents the effect of the application of the plasma flame on the sintered Inconel 718 components in order to replace the thermal treatment cycles. They are both presenting the optimization of the parameters of the treatments, which are the power of the microwaves, the peak temperatures and the holding time. The effects on the microstructure of the material and its mechanical properties are also investigated.

VII.1 Microwave sintering

VII.1.1 Microwave equipment and methodology

The microwave sintering equipment (Figure VII. 1) is composed of a microwave source going from 0.3 to 3 kW at 2.45 GHz. The microwave are directed towards the cavity of the equipment via

a rectangular guide tube, with a possibility to change the wavelength with two movable short-circuiting piston. They will help to concentrate the microwave radiation on the component. The atmosphere of the process can be controlled via the use of vacuum pumps and a gas managing control panel. The temperature is controlled via two infrared pyrometers, one going from room temperature and the second from 300 to 2000 °C. The equipment also measures the power produced and directed towards the cavity and the power that is not absorbed by the set-up in the cavity is coming back towards the source and is also measured, the difference between the two measures gives the power absorbed by the material. The temperature and the absorbed power also helps the equipment controlling software to adjust the microwave power in order to follow the programmed heating cycle such as the heating rate and peak temperature.

Figure VII. 1 Microwave single cavity mode equipment from Sairem

The MIM components used in this work are composed of binder A + Inconel 718 S 62% and binder B + Inconel 718 S 62% in cylinder and bar shapes. They both are fully debinded by solvent and thermal method in order to only have the metal powder interacting with the microwaves. The use of green compact is bringing cracks and defects of the component, as the high heating rate brings an excess of degradation gas inside the components. The tests can be performed on a rotary plate, helping to have a homogenous irradiation of the component.

The Figure VII. 2 displays the different set-ups that were used in order to perform the thermal treatment of the brown components. The first is just the component with an alumina support below it. The second is the component surrounded by an alumina powder to act as a susceptor. The alumina possesses a high dielectric loss factor and its behaviour when irradiated with microwaves is well known [11]–[13]. By putting the MIM component into alumina powder, the goal is to reduce the chance of arcing during metal-MW interaction and helps to obtain a homogeneous temperature around the component. The last set-up is to use a graphite die in the same configuration as during the

FAPH sintering tests. The graphite is a better heat conductor than the alumina and the interaction with the microwaves is also limited.

The tests are performed in an argon controlled atmosphere after completing the vacuum inside the cavity and purging with a bit of argon two times. The choice of using argon is imposed by the material, as advised by the literature [14]. The nitrogen is preferably used during the microwave experiments as the dielectric strength is higher than argon but cannot be used because of the problems observed during the sintering with nitrogen, with the possibility to create nitrides inside of the material.

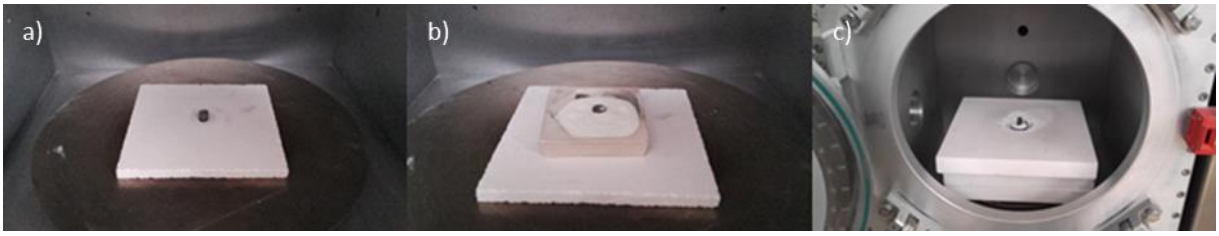

Figure VII. 2 Three set-up used during the microwave sintering tests: a) alumina support, b) surrounded by alumina powder and c) graphite die and tungsten foil surrounded by alumina powder

VII.1.2 Sintering of the MIM component

The first set-up was used as it is the easiest to install. They were performed with both bars and cylinders Inconel 718 brown components at different micro-wave power. Even by using a minimum power, they all resulted in the creation of a huge electric arc inside the cavity of the equipment shown on Figure VII. 3. They have triggered a light sensitive detector and stopped the tests, meaning the incapacity to reach a temperature high enough to activate the sintering mechanism of the powder. At each test, the electrical discharges appeared while reaching the 700 °C.

The Figure VII. 3 also shows the Paschen curves for different gases, argon comprised. They are obtained by following the Paschen law, which is an empiric law that states that once a certain value of electric voltage is crossed, electric arcs are created. The graphic displays the breaking voltage V_b in function of the value pd, which is the product between the pressure of the gas with the distance between the electrodes. The evolution of all the curves follows the same behaviour and have two windows where it should be difficult to create electric arcs, one at a high level of vacuum and the second when the pressure is close to the atmospheric pressure or even in case of overpressure. Thus multiple tests were performed at different argon atmosphere between 10 and 103.5 kPa of argon, but each time, the tests failed. The difference between the law detailed here and our condition is the

distance between electrodes. The theory between the microwave sintering is the movements induced by the passage of the microwave irradiation, but it was also proved that during the process, plasmas were generated between particles and was helping the system to reach faster high temperatures [15]. Because the component is fully debinded, there are multiple cavities created between the different particles, leading each of them to a potential starting point for the electric discharge. After accumulating a high amount of energy, an electric discharge is created, leading to a plasma, itself growing from the microwave irradiation.

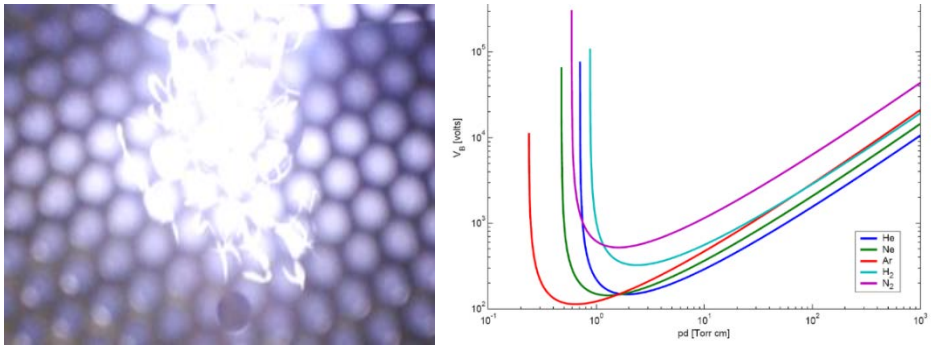

Figure VII. 3 Electric arcs created during tests around 700 °C at 0.80 kW during microwave irradiation with set-up a) and Paschen law curves of different pure gas

The set-up b) was tested in order to reduce this effect and to reach higher temperatures. The alumina powder helped to reduce the effects of the electric arc at low temperatures, however it is not enough to avoid them and they still appear once the temperature is reaching around 1000 °C. Sometimes, the electric discharge was confined below the alumina powder, allowing to reach high temperature around 1200-1300 °C. The problem is that the created electric arc consumes energy and will deviate the microwaves and absorb it instead of the MIM component. The pyrometer measured the right sintering temperature but not on the component but of the alumina powder next to it. The result of the electric arc is also the breaking of the component during the release of the electric arc Figure VII. 4.

Figure VII. 4 Electric arcs created during microwave irradiation appearing at temperatures around 1000 °C and picture of the damaged component after the test

The last set-up was prepared in order to perform a hybrid heating via microwaves. The graphite is a good dielectric material and is a good thermal conductor. The goal of the set-up is to use the microwave irradiation to heat the graphite around a MIM component introduced inside the graphite die protected with Tungsten foils. The component is placed between two graphite cylinders with one being pierced in the centre in order to measure the temperature of the component as close as possible.

The graphite die is set in the middle of a SiC plaques and completed with alumina powder around it. If the graphite die is exposed to the microwaves alone, it was impossible to rise temperature above 400 °C. The images of Figure VII. 5 exhibit the behaviour of the temperature expected from the set-up with the rise of the graphite die with the temperature. The last image was taken at 3.0 KW and the temperature reached by the system was of only 1050 °C. At this temperature, the obtained component did not start to densify.

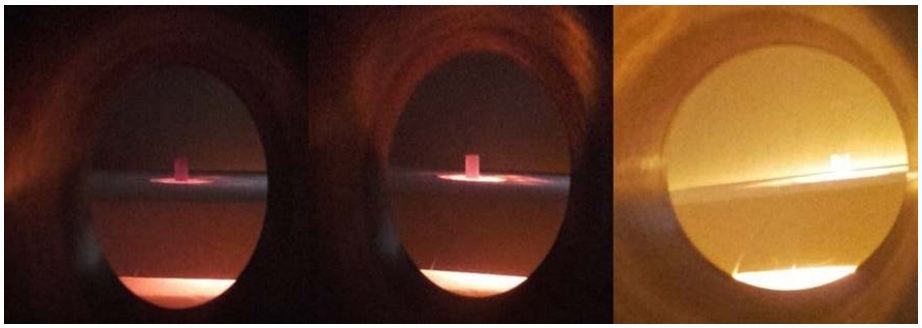

Figure VII. 5 Images of the evolution of the temperature during the microwave irradiation at 1.0, 2.0 and 3.0 kW with set-up c)

The main conclusion of the different tests performed on each set-ups, is that using these configurations, microwave sintering is not suitable to allow the densification of a MIM Inconel 718 component. There are a few reasons that could explain the incapacity to reach the proper temperature.

The first is the requirement to use argon gas in order to obtain a good sintering of the material. The second is the use of a material composed of 8 different chemical elements, with different dielectric properties, which could bring instability to a fragile equilibrium inside the component.

The use of the graphite die shown the most promising results, but it didn’t reach a temperature high enough to start the densification of the powder. The direct heating or hybrid heating by microwave irradiation with our equipment seems inadequate with the Inconel 718

VII.2 Heat treatment via plasma microwave

VII.2.1 Plasma microwave equipment and methodology

The plasma microwave equipment Figure VII. 6 is designed to initiate and maintain a uniform plasma flame inside a quartz tube. In order to create it, a microwave source, identical to the first equipment, sends microwaves through a rectangular guide tube. The tube is equipped with three tuners which helps to provide a maximum of the power towards the cavity. The cavity is composed of a quartz tube, with a gas feeding at the top and a supporting system at the other side with a vacuum system and an infrared-pyrometer. The microwaves, after crossing the quartz tube meets a short circuiting piston that is sending back the microwaves towards the quartz tube and the three tuners. Once the four elements are correctly tuned, the maximum of the power is concentrated inside the quartz tube.

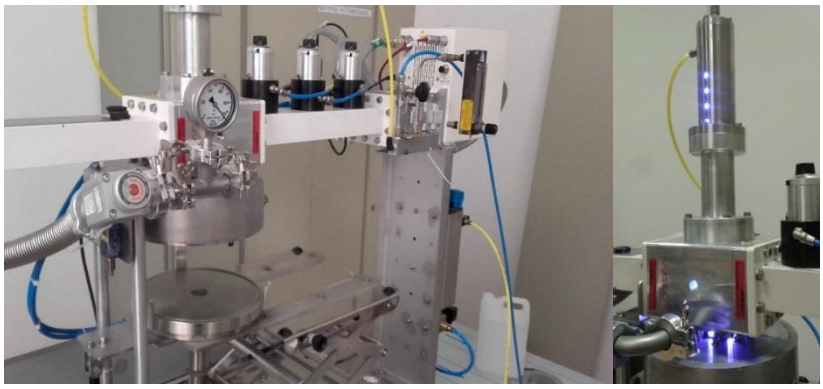

Figure VII. 6 Plasma microwave equipment from Sairem

Then the system follows the Paschen law and once a critical power is reached, the plasma flame is ignited and maintained by the microwave source as long as the gas feeding system is providing a continuous flow. This principle allows the creation and the hold up a plasma column of a certain length, depending of the pressure, the power and the nature of the gas. Depending on the gas used, a plasma flame can go to high temperature at a really fast rate [1]. As the direct microwave heating of the Inconel 718 components were bringing problems with the electric arcing, the use of this equipment is in fact taking advantage of the electric arcing by igniting and maintain the plasma flame.

The sample is introduced inside the chamber and positioned thanks to an alumina tube right in front of the microwave source. The control of the atmosphere inside the chamber is done via a vacuum pump and different inlets of gas. In our case, argon is used thanks to its facility to be ionized [16].

The power of the microwaves can be set between 0.10 and 3.0 kW. The temperature is measured under the support via an infra-red thermocouple that starts at 400 °C. This equipment was designed to hold up until around 2300°C. The heating rate and the temperature obtained during sintering depend on the length of the flame and the distance from the sample.

The sintering of the MIM components tests were performed by following the same cycle. The power of the microwave source is increased step by step by 100°C every minute until around 1300°C during a measured time. The increase in temperature is performed step by step in order to avoid defects of the component with an excessive heating rate. The microwave power described in the results is the real power that was absorbed by the plasma flame by measuring the original power sent inside the chamber and the returned power after absorption by the plasma flame and the sample. In the case of the application of the thermal treatment, they were performed on sintered Inconel 718 MIM components via the optimized furnace sintering cycle presented in chapter 3. This time, the wanted temperature is obtained as fast as possible once the plasma flame is created.

VII.2.2 Plasma microwave sintering of MIM components

The Figure VII. 7 shows the evolution of the temperature and the power absorbed by the system. When the sintering temperature was reached, the power needed to keep a constant temperature remained constant. After some minutes, more power was needed until reaching the limit of 3 kW of the equipment. At the end of one hour of dwell time, it was not enough to maintain the temperature and a uniform plasma. This effect could be explained by the closing of the porosities with the time. Because of the lack of connection between the porosities, it was harder for the microwaves to go through the sample and more power was needed to force its way through the material [17].

Figure VII. 8 presents the microstructures of two samples obtained after a sintering dwell time of 30 and 60 min. After 30 min, the powder particles are still observable. The size varies between 20 and 40 µm. The growth behaviour of the particles looks similar to the conventional way. However, the ratio between large and small particles is not the same and could be explained by a phenomenon already observed with other materials during microwave sintering. The formation of hot points on some samples is observed and are followed by an abnormal enlargement of the particles.

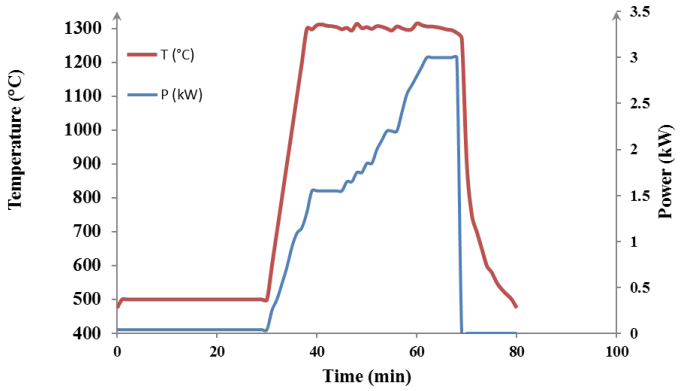

Figure VII. 7 Evolution of the temperature and the microwave power in function of the time during plasma microwave sintering of Inconel 718 MIM component

The formations of these points are explained by reaching locally high temperatures and after a critical temperature, the particles starts to sinter before the others, resulting in an inhomogeneous growth of the particles during sintering. A too high power of the microwaves applied on the material explains this phenomenon [18]. After 1 hour of sintering, the microstructure presents no signs of porosity and no more particles are observable. The obtained relative density of the component is of 95.8 ± 1.4 % and a hardness of 191 ± 12 HV is obtained. The shape of the component was not maintained and some cracks can be observed at the surface of the component. They could be explained by the high heating rate that is still too brutal for powder compact without an adapted support.

The Figure VII. 9 resumes the indentation mapping of the component sintered during 60 minutes and is representing the repartition of the hardness and the Young modulus on a zone of the material. They are performed on a zone with a size of 50 x 40 µm. The indentation Young modulus is divided between two values of around 160 GPa and 210 GPa at the exception of two zones on the upper right corner and the middle where the highest values are measured of 343 GPa. The hardness is more homogenous around an indentation hardness between 200 and 450 HV. The same two points have a hardness above the 1000 HV. This test put in evidence that there are inclusions inside the microstructure with a hardness close to the hardness of an oxide. This test confirms the problem of sintering homogeneity observed on the microstructures as well as a possibility to affect the chemistry of the material.

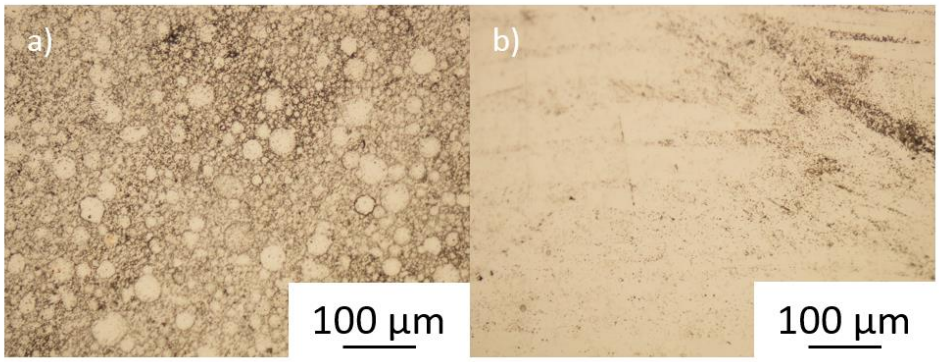

Figure VII. 8 Optical Microscopy images of the samples sintered by microwave sintering during a) 30min and b) 60min

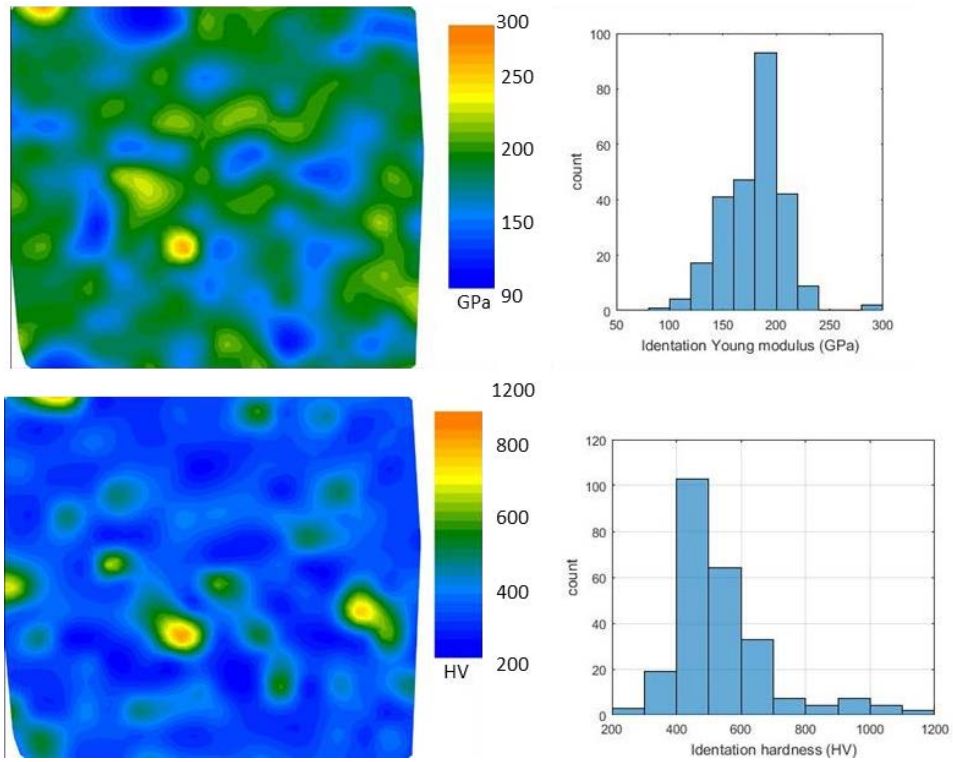

Figure VII. 9 Mapping of the measured Young modulus (above) and of the hardness (below) obtained after nano-indentation on plasma sintered Inconel 718 MIM component

VII.2.3 Plasma flame heat treatment

The sintering of a MIM brown component by the plasma microwave allowed to obtain a densified material but presenting an anisotropy of the both microstructure and mechanical behaviour. However, it could be interesting to observe the effect of a plasma flame on a conventionally sintered MIM component. The microstructure is already developed and the component is more resistant to thermal

and mechanical shocks. Thus this part introduces the optimization and the effect on the microstructure.

The sintered MIM component are thermally treated at 750 °C during different dwell times. This temperature was reached in less than one minute for a microwave power of around 0.6 kW. The Table VI. 6 resumes the hardness measurements obtained after 15, 30 and 60 minutes. After a dwell time of 15 minutes, the hardness is at the same level as the reference hardness obtained after conventional sintering. However, after 30 minutes, the hardness is getting to the same level as the thermal treatment applied in chapter 3. After 60 minutes, the hardness dropped and was even lower than the starting material. If the material is exposed too long under the plasma flame, it has a detrimental effect and is damaging the component.

Table VI. 6 Hardness measurements after plasma microwave thermal treatment at 750 °C

Dwell time	Hardness at centre (1.0 HV)	Hardness at surface (1.0 HV)
15	240 ± 8	229 ± 5
30	397 ± 3	375 ± 6
60	226 ± 6	179 ± 12
Reference	249 ± 4	232 ± 2

The Figure VII. 10 shows the SEM image of the component and an EDX mapping of the different chemical elements. The localization of all the hardening elements such as the niobium, the titanium and the molybdenum are all concentrated in inclusions inside the microstructure. The nickel, the chromium and the iron are composing the matrix around these elements.

Finally carbon was found at the same place as the hardening elements, meaning carbides are present. These carbides may come from the debinding residues. The argon gas used was of laboratory grade, meaning that the carbon was not brought with the gas while the component was under the plasma argon flame. The interesting point is that there were no traces of oxygen at the surface of the components, meaning that the oxidation of the material is only happening during the sintering of the powder and not during the thermal treatment.

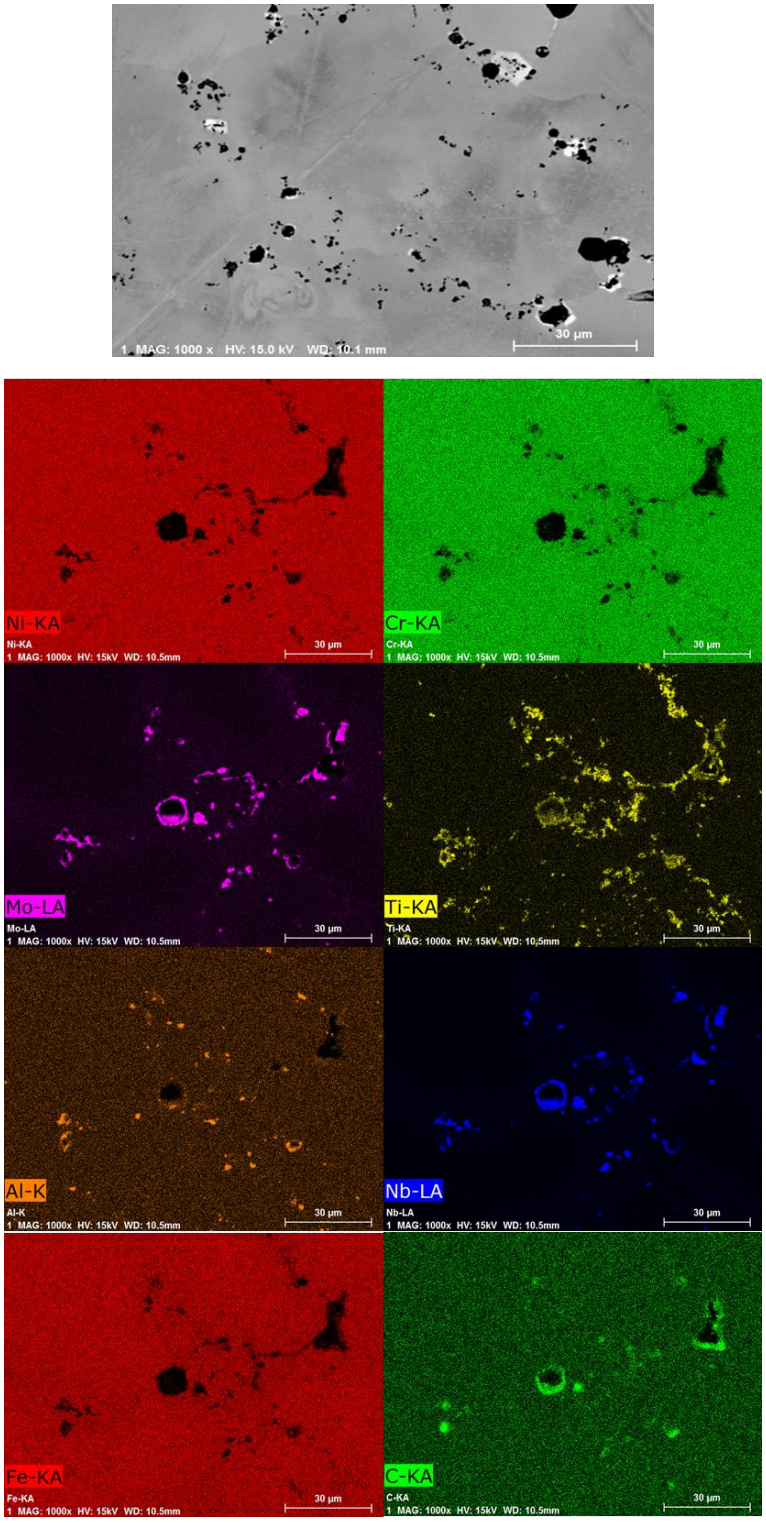

Figure VII. 10 SEM image of Plasma microwave thermal treatment at 750 °C during 30 min of a sintered Inconel 718 MIM component and EDX mapping of the image

VII.3 Partial remarks

The direct and hybrid microwave sintering was used on MIM Inconel 718 brown components but the irradiation by microwaves of the material promotes the creation of electrical discharge. These discharge were then amplified until the creation of plasma arcs forcing the end of the tests. The set-up using a graphite die in order to reduce the electric discharge was efficient but it also lowered the maximum temperature allowed by the power of the microwave source. Hence, it was not possible to obtain a sintered component by applying microwaves irradiation on the Inconel 718 MIM components.

The plasma microwave is however a method that takes advantage of this phenomenon by maintaining a plasma flame. The use of argon and a microwave power from 1.5 kW to 3 kW during 60 minutes allowed to obtain a fully dense material. The characterization of the microstructure and of the mechanical behaviour by nano-identation showed an inhomogeneous behaviour in both of them. It could be explained by the creation of hot-spots inside the component which then were consuming more energy than the surrounding particles. Because of this, an anisotropic growth of the grains caused an inhomogeneous microstructure. The traces of oxides inside the microstructure indicates that the plasma flame brings chemical modification of the material which could impact the mechanical behaviour of the material while under tensile stress.

Finally, a sintered MIM component was put under a plasma flame of 750 °C at different times in order to heat-treat it. From the hardness measurement, a dwell time of 30 minutes is enough to reach the same level as a conventional thermal treatment at 720 and 650 °C during 8 hours each. However, if the dwell time exceeds over 30 minutes, the treatment lowers the hardness.

REFERENCES

[1] Z. Peng et J.-Y. Hwang, « Microwave-assisted metallurgy », Int. Mater. Rev., vol. 60, nº 1, p. 30‑63, août 2014.

[2] D. K. Agrawal, « Microwave processing of ceramics », Curr. Opin. Solid State Mater. Sci., vol. 3, nº 5, p. 480‑485, oct. 1998.

[3] J. Croquesel, D. Bouvard, J.-M. Chaix, C. P. Carry, S. Saunier, et S. Marinel, « Direct microwave sintering of pure alumina in a single mode cavity: Grain size and phase transformation effects », Acta Mater., vol. 116, p. 53‑62, sept. 2016.

[4] R. Roy, D. Agrawal, J. Cheng, et S. Gedevanishvili, « Full sintering of powdered-metal bodies in a microwave field », Nature, vol. 399, nº 6737, p. 668‑670, juin 1999.

[5] D. Demirskyi, D. Agrawal, et A. Ragulya, « Neck growth kinetics during microwave sintering of nickel powder », J. Alloys Compd., vol. 509, nº 5, p. 1790‑1795, février 2011.

[6] R. Bao et J. Yi, « Densification and alloying of microwave sintering WC–8 wt.%Co composites », Int. J. Refract. Met. Hard Mater., vol. 43, nº 0, p. 269‑275, mars 2014.

[7] O. Ertugrul, H.-S. Park, K. Onel, et M. Willert-Porada, « Effect of particle size and heating rate in microwave sintering of 316L stainless steel », Powder Technol., vol. 253, nº 0, p. 703‑709, février 2014.

[8] J. Mascarenhas, T. Marcelo, A. Inverno, J. Castanho, et T. Vieira, « Microwaves show off their advantages in efficient sintering », Met. Powder Rep., vol. 63, nº 11, p. 12‑15, déc. 2008.

[9] J. Shi, Z. Cheng, J. C. Gelin, T. Barriere, et B. Liu, « Sintering of 17-4PH stainless steel powder assisted by microwave and the gradient of mechanical properties in the sintered body », Int. J. Adv. Manuf. Technol., vol. 91, nº 5‑8, p. 2895‑2906, juill. 2017.

[10] C. Leonelli, P. Veronesi, L. Denti, A. Gatto, et L. Iuliano, « Microwave assisted sintering of green metal parts », J. Mater. Process. Technol., vol. 205, nº 1, p. 489‑496, août 2008.

[11] D. Żymełka, S. Saunier, D. Goeuriot, et J. Molimard, « Densification and thermal gradient evolution of alumina during microwave sintering at 2.45GHz », Ceram. Int., vol. 39, nº 3, p. 3269‑3277, avr. 2013.

[12] M. A. Janney, H. D. Kimrey, M. A. Schmidt, et J. O. Kiggans, « Grain Growth in Microwave-Annealed Alumina », J. Am. Ceram. Soc., vol. 74, nº 7, p. 1675‑1681, juillet 1991.

[13] V. Delobelle, J. Croquesel, D. Bouvard, J. M. Chaix, et C. P. Carry, « Microwave sinter forging of alumina powder », Ceram. Int., vol. 41, nº 6, p. 7910‑7915, juillet 2015.

[14] C. Slama et G. Cizeron, « Étude du comportement structural de l'alliage NC 19 Fe Nb (Inconel 718) », J. Phys. III, vol. 7, nº 3, p. 24, 1997.

[15] K. P O'Flynn, B. Twomey, A. Breen, D. Dowling, et K. Stanton, « Microwave-assisted rapid discharge sintering of a bioactive glass-ceramic », J. Mater. Sci. Mater. Med., vol. 22, p. 1625‑31, mai 2011.

[16] J. M. Hill et T. R. Marchant, « Modelling microwave heating », Appl. Math. Model., vol. 20, nº 1, p. 3‑15, janv. 1996.

[17] G. Roussy, « Temperature runaway of microwave heated materials: study and control », J Microw. Power, 1985.

[18] J. M. Hill et M. J. Jennings, « Formulation of model equations for heating by microwave radiation », Appl. Math. Model., vol. 17, nº 7, p. 369‑379, juillet 1993.

VIII CONCLUDING REMARKS

This work is focused on the application of new methods on MIM components in order to reduce the cost in time and energy of the process. The selected material for the project is a nickel-chrome superalloy Inconel 718, chosen for its high mechanical performances and its nonmagnetic property. The MIM process for this material is well developed and so is the processing conditions. Thus it offers enough experimental information for a comparison with the effects of the three selected methods of the project.

MIM components were elaborated with two different Inconel 718 powder morphologies. The first one is a commercial spherical powder and the second one is a milled flake shape powder. They were used to elaborate feedstocks by mixing them with two binders. Four feedstocks were selected during the optimization of the feedstock elaboration. The spherical powder was mixed with binder A at two different powder loading volumes, 62 and 71 (wt.) % and with binder B at a powder loading volume of 62 (wt.) %. The milled powder was mixed with binder A for a powder loading volume of 55 (wt.) %. All four of the feedstocks were injected into MIM components.

Table VIII. 1 Properties obtained after water and supercritical debinding

Debinding method	Powder	Cycle parameters	PEG removed (%)	Rp (µm)	Ra (µm)
water	Inconel 718 S	72 hours, 50 °C	99.3	9.27	3.77
	Inconel 718 M	72 hours, 30 °C	97.2	-	-
CO2 supercritical	Inconel 718 S	4 hours, 150 °C, 400 bars	99.1	6.03	2.21
	Inconel 718 M	4 hours, 150 °C, 500 bars	100.7	-	-

The conventional MIM process was applied to these components and optimized in order to reach the best properties possible. The solvent debinding with water was performed at 50 °C during 72 hours in order to extract all the PEG introduced inside of the feedstocks. The debinding by supercritical fluid was applied to the component as a way to substitute with the solvent debinding. The method worked efficiently with the binder A without damaging the components on the contrary

of the binder B. The tests performed on this feedstock completely crumbled the components. The Table VIII. 1 presents the results obtained with the two methods. In the case of the spherical powder, the two debinding methods allowed the complete removal of the PEG. However the supercritical debinding shows a much better debinding rate and a lower effect on the final quality of surface. The results in the case of the milled powder are differing, as the supercritical debinding damages the components. Thus, this method has to be limited with the morphology of the powder.

The sintering cycles of the MIM components was possible with three methods, by thermal diffusion inside a furnace, by application of a high electric current on a component under pressure and by irradiating a component with microwaves. The direct microwave irradiation of the Inconel 718 powder did not allowed to reach the sintering temperature, but the application of a plasma flame maintained by the microwave irradiations enabled the densification of the component. The results of the optimized cycles for each methods are presented in Table VIII. 2. The FAHP sintering obtained the best results in terms of density, hardness and mechanical performances. It is even more interesting as the cycle was completed in less than one hour instead of the 10 hours needed to perform the conventional sintering. The plasma flame sintering is also performed in a shorter time, but the heterogeneous microstructure obtained lowered the mechanical performances of the component.

Table VIII. 2 Properties after sintering with the conventional, FAHP and microwave equipment

Sintering method	Cycle parameters	Density (%)	Hardness (1.0 HV)	UTS (MPa)	E (MPa)
furnace	1290 °C at 5 °C/min during 4 hours	97.8	212	817	63.4
FAHP	1250 °C at 300 °C/min during 15 min	99.5	251	1022	48.71
plasma flame	1300 °C at 100 °C/min during 60 min	95.8	191	-	-

The thermal treatment was also applied with the previous three methods. The results obtained after the optimization of the treatment cycles is presented in Table VIII. 3. Once again the best results were obtained with the FAHP method within a short time compared to the conventional furnace equipment. However, the plasma flame treatment also exhibits good terms results, both in terms of hardness and microstructure.

The performances of the Inconel 718 MIM components, after the different treatment applied presented in this work, bring out a new processing road. The spherical powder is needed in order to

avoid troubles during the debinding and sintering steps. It is possible to perform the conventional process on a flake shape powder, but it is not the more efficient. The binder A exhibited a more interesting behavior as it was able to withstand the supercritical debinding on the contrary of the binder B.

Table VIII. 3 Properties after thermal treatment with the conventional, the FAHP and the microwave equipment

Thermal treatment method	Cycle parameters	Density (%)	Hardness (1.0 HV)
furnace	720 and 620 °C during 8 hours each	97.6	341
FAHP	750 °C during 15 min	99.4	394
plasma flame	750 °C during 30 min.	98.5	375

The supercritical debinding displayed great results with a high debinding rate compared to the solvent debinding. It fulfils the requirements of this debinding step. It reacts with one of the element of the binder, it extracts most of this element and does not damage the component. It even had a positive effect on the surface quality of the components. The only disadvantage of this method is the initial cost of the equipment compared to a water bath equipment, which could lower the interest for an industrial application at the moment.

The sintering by FAHP method exhibits the best results in terms of mechanical performances. The application of a pressure on the MIM component limits the possibility of the shape of the components as it has to resist to the minimal pressure applied. The performances of the components displays good mechanical performances for a low cost in energy and time. The next step for the combination of the MIM process and the FAHP sintering may be to research a way to conserve a more complex geometry with this method.

The thermal treatment of the Inconel 718 is necessary in order to maximize the formation of the hardening γ'' phase. The thermal treatment with a furnace needs at least 16 hours in order to reach the best properties of the material. The FAHP displays again good results for a short time. However, the plasma flame treatment also shows interesting results. This method may be easier to set-up for the mass production of MIM components. Thus, the plasma flame treatment may be more interesting for an industrial application. The research of the surface treatment of the MIM components can be a

way to improve the method by researching the effects of different atmospheres on the surface chemistry of the Inconel 718 MIM components.

The MIM process proposed during this work allowed the production of components with high performances and answered to the specifications of the industrial partners of the ProPIM project. The supercritical fluid debinding is the most promising method for an industrial application as it is well adapted to the mass production of components. It was applied to industrial components, like the one presented in the introduction of the project but also to ceramic components provided by another partner, with a paraffin wax binder. They both show promising results in terms of polymer extraction rate and extraction ratio. The components with a more complex geometry were not damaged. The work performed on the FAHP and the plasma flame thermal treatment of the Inconel 718 MIM proved that both of the methods are compatible with the Inconel 718 MIM components but they both need a more specific research work in order to completely understand the extent of the possibilities available when it is combined with the MIM technology.